Department of Precision and Microsystems Engineering

Design of a silicon photonic microphone

Jasper Scheepstra

Report no : 2023.062.
Coach : Wouter J. Westerveld, Paulina Castro Rodríguez (PhD)
Professor : Peter G. Steeneken
Specialisation : Mechatronic System Design (MSD)
Type of report : Master Thesis
Date : 17 August 2023

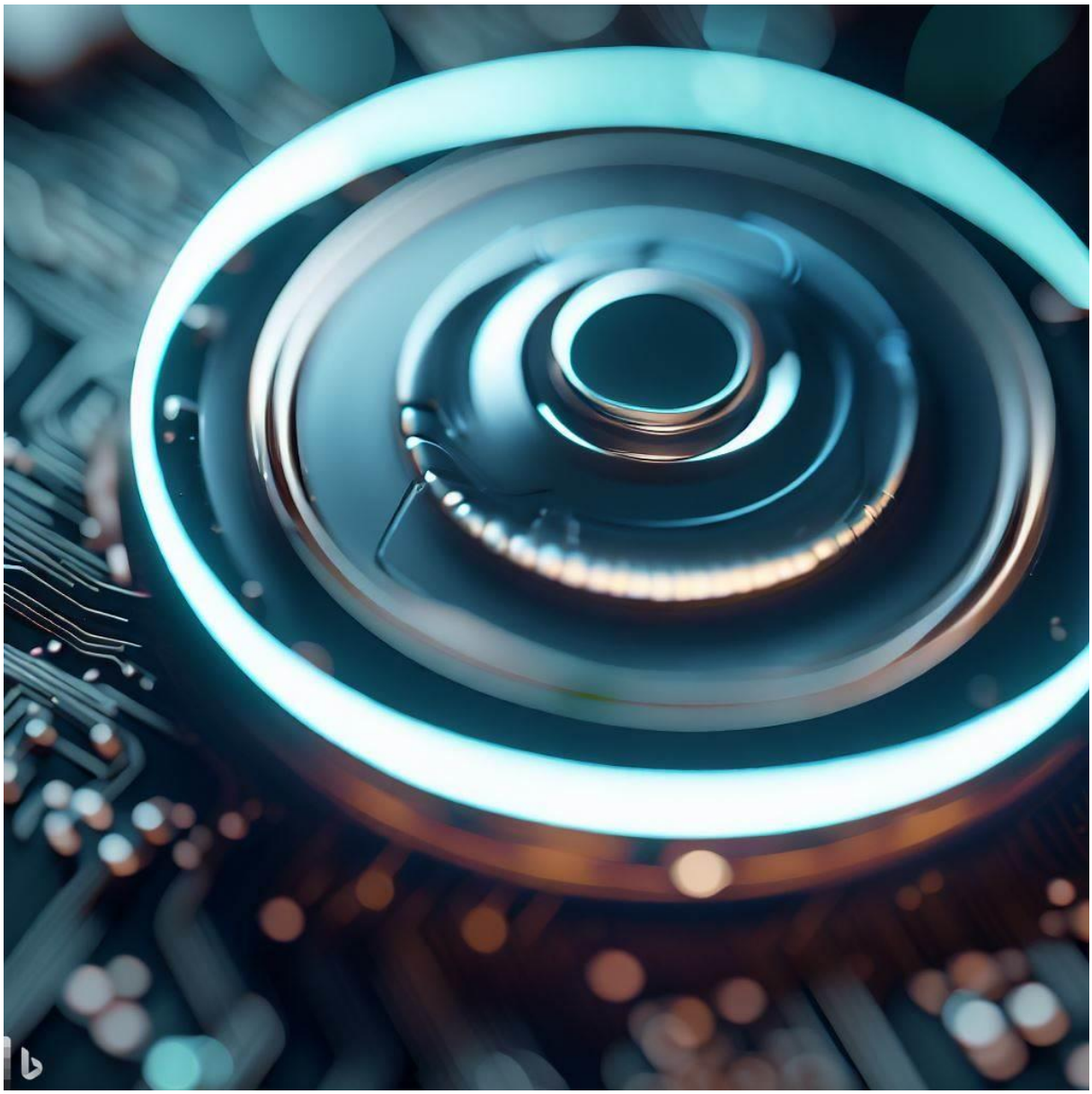

Thesis

Design of a silicon photonic microphone

by

J. A. Scheepstra

This thesis is submitted in partial fulfilment of the requirements of the MSc degree in Mechanical Engineering at the Delft University of Technology

Student number: 4594533

Supervisors: W. J. (Wouter) Westerveld

P. G. (Peter) Steeneken

P. (Paulina) Castro Rodríguez (PhD)

Abstract

In a world increasingly dominated by technological advancements, the demand for high-quality microphones has never been more present. Seamless speech recognition and the development of user-friendly hearing aids remain significant challenges. State-of-the-art micro-electromechanical system (MEMS) microphones are reaching their bottlenecks in terms of thermo-acoustic noise, caused by the acoustic resistance of the parallel plate capacitor. This constrains the achievable signal-to-noise ratio (SNR). This thesis presents a novel solution to address these challenges through the application of silicon photonics technology in the development of a silicon photonic microphone. Silicon photonics is a technology that uses silicon as an optical medium to create photonic systems with sub-micrometre precision, which can be used to create ultra-sensitive sensing devices. The optical sensors are fabricated on standard silicon-on-insulator (SOI) wafers, allowing for seamless integration with the precise and cost-effective complementary metal-oxide-semiconductor (CMOS) process. The optomechanical sensitivity of the proposed microphone is derived for three different cladding materials that could be deposited on the wafer in the fabrication process. The thermal acoustic noise of the microphone is quantified. As the integrated photonic circuit does not require a backplate the design potentially reduces the thermal acoustic noise of current microphones by 44 %. The optimized design for the laboratory setup that is considered for this thesis can theoretically result in an SNR of 73.1 dB, which is roughly 5 dB more than the current state-of-the-art microphone technology.

Contents

Nomenclature

If a nomenclature is required, a simple template can be found below for convenience. Feel free to use, adapt or completely remove.

Abbreviations

Abbreviation	Definition
ADC	Analogue-to-Digital Converter
ASIC	Application Specific Integrated Circuit
CMOS	Complementary Metal-Oxide Semiconductor
DRIE	Deep Reactive Ion Etching
ECM	Electret Condenser Microphone
FDT	Fluctuation-Dissipation Theorem
LFRO	Low-frequency Roll-Off
MEMS	Micro-Electro-Mechanical System
MZI	Mach-Zehnder Interferometer
OMUS	Optical Micro-machined Ultrasound Sensor
PCB	Printed Circuit Board
PD	Photodiode
SFD	Squeeze-Film Damping
SNR	Signal-to-Noise Ratio
SOI	Silicon On Insulator
TE	Transverse Electric
TM	Transverse Magnetic
VCSEL	Vertical Cavity Surface Emitting Laser

Symbols

Symbol	Definition	Unit
a	Radius of diaphragm	[m]
A_p	Area of parallel plate capacitor	[m^2]
b	Radius of the ring resonator	[m]
c	Damping coefficient	[kg/s]
c_0	Velocity of sound in air	[m/s]
$C(p)$	Capacitance	[F]
C_0	Capacitance of parallel plate at initial distance	[F]

Symbol	Definition	Unit
C_m	Mechanical compliance of the diaphragm	[m/Pa]
C_p	Specific heat constant	[J/(kg K)]
D	Flexural rigidity	[N m^2]
db	Change in ring radius of the ring resonator	[m]
F	External applied force	[N]
g	Distance between parallel plate capacitor	[m]
h	Plate thickness	[m]
H	Frequency response	[-]
I_n	Modified Bessel function	[-]
J_n	Bessel function	[-]
j	Imaginary number	[-]
$k*$	Spring stiffness	[N/m]
$k*$	Convenience parameter	[rad s / m^5]
$k*$	Wavenumber / propagation constant	[rad/(ms)]
k_b	Boltzmann constant	[J/K]
m	Mass	[kg]
n	Order of Bessel function	[-]
n_e	Effective refractive index	[-]
p	Pressure	[Pa]
q	Charge on capacitor	[C]
Q_0	Initial total charge of parallel plate capacitor	[C]
Q	Q-factor	[-]
r	Radial coordinate	[m]
t	Time	[s]
u	Piston velocity	[m/s]
V	Voltage	[V]
V_0	Bias voltage applied to capacitor	[V]
V_p	Pull-in voltage of capacitor	[V]
w	Displacement circular plate	[m]
W	Displacement shape circular plate	[m]
x	Position	[m]
Z_a	Acoustic impedance	[Pa s/m^3]
Z_{sa}	Specific acoustic impedance	[Pa s/m]
Z_{mr}	Mechanical impedance	[N s/m]
α	Propagation loss coefficient	[-]
ϵ_0	Permittivity of vacuum	[F/m]
ϵ_r	Relative permittivity of material	[F/m]
$\boldsymbol{\mathcal{E}}$	Electric field	[V/m]

Symbol	Definition	Unit
η	Dynamic viscosity	[Pa s]
ϕ	Phase change	[rad/s]
γ	Ratio of specific heats	[-]
$\boldsymbol{\mathcal{H}}$	Magnetic field	[A/m]
κ^*	Thermal conductivity	[W/(m K])
κ^*	Coupling coefficient	[-]
λ_{ns}^*	Eigenmodes that define mode shape of circular plate vibration	[-]
λ^*	Wavelength	[m]
λ^*	Normalized wavenumber	[-]
μ	Permeability	[m^2]
ω	Radial frequency	[rad/s]
ρ	Density	[kg/m^3]
σ	Squeeze number	[-]
τ	Transmission coefficient	[-]
θ	Angular coordinate	[rad/s]
ζ	Damping ratio	[-]

* This variable comes back multiple times and is explained per section.

1 Introduction

In the era of digital communication, the microphone has become an essential device for many electronic devices such as smartphones, notebooks, hearing aids, headphones and even smart home devices. Consequently, the demand for high-performance, low-cost, and small-size microphones has been increasing rapidly. The micro-scale version of a microphone, known as microelectromechanical systems (MEMS) microphone, is ideal for use in portable and battery-powered devices due to their small size, low power consumption, and high sensitivity. MEMS microphones perform so well that in only 10 years, more than 90% of the traditional electret condenser microphones (ECMs) in mid-to-high-end smartphones have been replaced by MEMS microphones [1].

There is still untapped potential for improvement in MEMS microphones, which offers numerous benefits, such as enhancing speech recognition capabilities [2]. Even more so, an extensive review of the effect of background sound on hearing aid user experience showed that many users indicate background noise amplification as the primary reason for the non-usage of the hearing aid [3]. A recent small study confirms that users still experience difficulties in louder and noisy environments [4]. Improving the microphone can lead to better signal separation and noise reduction.

Developing MEMS microphones has a significant financial benefit: market research by Yole Development predicts a market size of $1 billion [5]. As such, it is not surprising that extensive research has been conducted to improve the design and performance of these devices. The research and development are mostly focused on improving the sensitivity, signal-to-noise ratio (SNR) and dynamic range of the microphone. These parameters are explained in more detail in Table 1.1.

This introduction provides an overview of the current state of the art in MEMS microphone technology and proposes the integration of silicon photonics to address the limitations and challenges of existing MEMS microphone designs. Finally, from the insights gained from the aforementioned subjects, a research question is formulated, which addresses the objectives of this thesis. The introduction concludes by providing a clear overview of the thesis, highlighting the specific topics that will be discussed in each respective part.

1.1. Types of MEMS microphones

MEMS microphones can be roughly subdivided into three categories: piezoelectric, capacitive and optical microphones. All of them use some type of silicon micromachining technique.

1.1.1. Piezoelectric

A piezoelectric microphone uses the piezoelectric effect to convert sound pressure into an electric signal, where the diaphragm is either mechanically connected to a piezoelectric material or is piezoelectric itself [6]. Piezoelectric MEMS microphones are typically less sensitive than capacitive or optical ones, but they have a larger dynamic range [7]. Previously it was suggested to use piezoelectric microphones in other applications such as aircraft design, rocket launching vehicles and biomedical engineering [6]. Due to advanced improvements today, more diverse applications become suitable [1, 7, 8]. However, current MEMS microphones often do not use this technique for audio application so no further research shall be done on piezoelectric microphones.

1.1.2. Capacitive microphones

The by far most dominant type of sensor in MEMS microphones is a parallel plate capacitor [1]. It measures capacitance to convert the acoustic pressure into an electric signal. A cross-section of a MEMS capacitive microphone is shown in Figure 1.1. When sound pressure enters the acoustic port,

the diaphragm (red) displaces relative to the fixed backplate (blue). Both the diaphragm and backplate are made of a conductive material such that a change in distance causes a change in the capacitance of the microphone. The change in capacitance is then converted into an electrical signal by an amplifier circuit, referred to as application specific integrated circuit (ASIC). A protective case (orange) surrounds the MEMS system and the ASIC to protect them against outside harms such as dust particles, electronic noise, incautious handling etc.

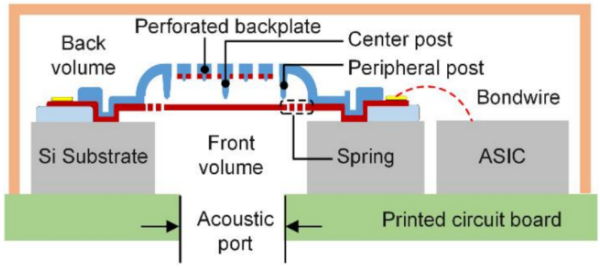

Figure 1.1: Cross-section of recently published MEMS capacitive microphone, from Ref. [9].

Noise sources

Capacitive microphones are considered the most advanced type of MEMS microphone currently available, and their performance capabilities and issues can be regarded as the current state of the art for MEMS microphone technology in general. The primary limitation on the performance of a MEMS microphone is caused by the acoustic thermal noise. Thermal acoustic noise is caused by the random motion of air particles - due to their thermal energy - that generates random pressure fluctuations, picked up by the microphone as noise.

Figure 1.2 indicates the noise power contributions of the complete microphone (right) and the distribution of only the acoustic noise power (left) of a recently published MEMS microphone [9]. Most of the noise is related to acoustic contributions, however, the largest individual contribution is from the ASIC. One way to improve the ASIC noise is to improve the sensitivity of the MEMS microphone to reduce amplification noise [10]. No further details will be provided regarding ASIC noise. Similar results in terms of acoustic noise of MEMS microphones were previously reported [11] [12].

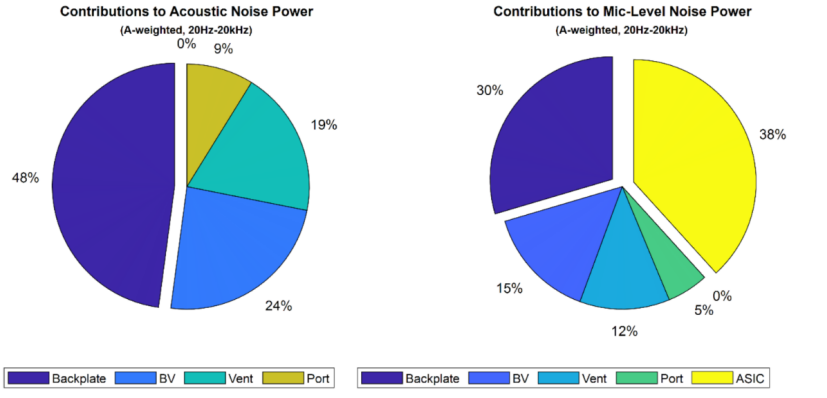

Figure 1.2: Contributions of acoustic noise power (left) and mic-level noise power (right), from Ref. [9].

In conclusion, the most notable areas for improvement in the current state of the art of MEMS microphones are reducing the acoustic noise generated by the backplate and the electronic noise produced by the ASIC. By addressing these issues, the overall performance of MEMS microphones can be greatly enhanced.

Previous attempts to improve backplate and ASIC noise

Various techniques have been developed to reduce the ASIC and backplate noise in capacitive microphones. Zawawi et al. have reviewed MEMS capacitive microphones of the past 30 years, which

lists two recent attempts of removing the backplate by adding the capacitors in a single layer (in the diaphragm). The first by Lo et al. [13] achieves no competitive sensitivity (-60.1 dBV/Pa) for a small frequency range of 1-20 kHz. The second by Mao et al [14] uses a standard CMOS process, but also reports a non-competitive sensitivity (-64 dBV/Pa) for a bad frequency range of 0.2-10 kHz.

Next to improving the thermal acoustic noise of the microphone, successful attempts have been made to improve the SNR by adding an additional backplate or an additional diaphragm in parallel to enable differential amplification. As opposed to noise, the two signals are correlated and the SNR can be improved by a factor of $\sqrt{2}$ (or 3 dB) [1, 15]. Unfortunately, parallel diaphragms require more surface area and a dual backplate adds acoustical noise due to squeezed film damping and viscous flow resistance. Kim and Lee found a poor 7% improvement to the SNR with an additional backplate using the differential amplification effect [16]. A more recently published microphone also applies differential amplification, this time with an additional diaphragm, called sealed-dual membrane [17]. The extra membrane creates a sealed low-pressure chamber, which reduces the acoustic resistance and improves the thermal-acoustic noise. The SNR is pushed towards 72 dB(A), however, the low-pressure chamber adds new issues and challenges for both the manufacturing process as well as the diaphragm compliance.

In conclusion, capacitive MEMS microphones have not been able to reduce the backplate and ASIC noise successfully. Another promising approach to enhance the backplate and ASIC noise is found in optical microphones, which use light to detect sound waves. By implementing an alternative readout principle and decreasing dependence on a backplate design, these devices have the potential to effectively lower the aforementioned noise levels. The next subsection will briefly introduce the state of the art of optic microphones.

1.1.3. Optical microphones

MEMS optical microphones use photodiodes in combination with an optomechanical circuit to convert sound pressure into an electric signal. In 1997 Bilaniuk wrote a comprehensive paper about different optical microphone transduction techniques [18], of which some are applied to MEMS optical microphones as well. At the time, no hard conclusions were drawn on which optical sensing method has the most potential for audio applications. A sensing method commonly found in MEMS optical microphones for audio application is a diffraction-based microphone which uses interferometric phase modulation.

Diffraction-based microphone

In Figure 1.3 a schematic of a diffraction-based optic MEMS microphone is shown together with a schematic of the manufactured microphone. A zero and higher-order diffracted field is created when a laser, such as a vertical cavity surface emitting laser (VCSEL), emits light towards a diffraction grating. The angles remain fixed but the intensities are modulated by the diaphragm deflection to produce the interference curves of a regular Michelson interferometer. Therefore, this technique has the sensitivity of a full-scale Michelson interferometer [19]. Diffraction-based optic MEMS microphones have reported the most competitive performance when compared to capacitive MEMS microphones. In 2011 Kuntzman et al. realised an optic MEMS microphone that implements the diffraction grating principle with a lower noise floor than commercially available MEMS microphones at the time. Unfortunately, their frequency response has a resonance below 20 kHz which is undesired for audio devices [20].

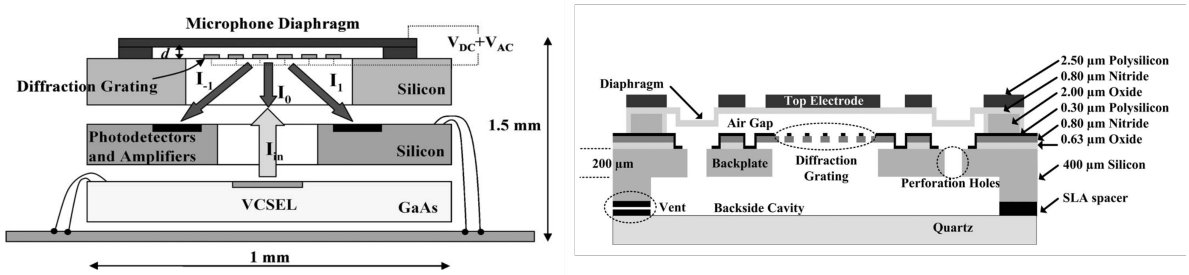

Figure 1.3: Schematic of fully integrated optical MEMS microphone that uses a diffraction grating[19]

The most recent publishing of a fabricated diffraction-based optic microphone marks a start towards the 80 dB SNR MEMS microphone (current capacitive MEMS microphones achieve around 70 dB

SNR [21])[22]. However, the grating system is not optimized properly to avoid large acoustic damping so again, the double-layered structure is problematic in terms of acoustic noise. Theoretically, it is possible to use less surface area of the dual layered structure and thus leave more space for air to flow without damping [22]. Additionally, it is worth mentioning that Apple Inc. has several patents on a diffraction-based optical MEMS microphone, underscoring the commercial interest of this type of MEMS optic microphone [23] [24]. Overall, the diffraction-based optic microphone has shown potential as an alternative to capacitive microphones, but it has yet to achieve significant advancements to prove itself. Furthermore, its complex manufacturing process opens the door for other optic MEMS microphone technologies.

Fabry-Perot interferometer

Another type of optical sensor found in MEMS optic microphones is a Fabry-Perot interferometer (FPI). An FPI also uses the phase change due to membrane deflection as sensing mechanism but in a slightly different configuration. A schematic diagram of an FPI is shown in Figure 1.4 by Zhou and Letcher [25]. At the end of the single-mode fibre, the light is reflected at the intersection with air and similarly the light is reflected by the diaphragm. These two reflections interfere and a change in light intensity can be measured.

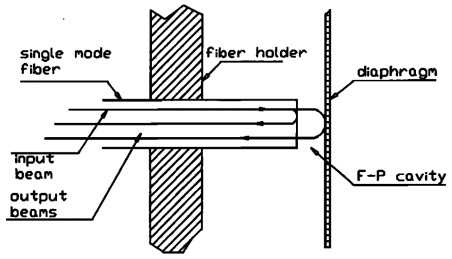

Figure 1.4: Schematic diagram of a Fabry-Perot interferometer [25]

An FPI-sensor applied to a MEMS diaphragm has shown promising results in terms of sensitivity and SNR when compared to a half-inch condenser microphone [26]. However, the membranes tested in this study did not exhibit a flat response across the audible frequency spectrum, and the dynamic range was limited for sensitive membranes. Similar findings of high sensitivity and limited dynamic range have been reported in a study by Liu et al. (2018), which also utilized an FPI-based sensor [27]. Both studies were limited by optical fibres perpendicular to the membrane, such that neither of them achieved a fully integrated sensor as a MEMS microphone. Despite the promising sensitivity results, the current state of FPI-sensor technology for MEMS microphones is still limited and further research is needed to fully integrate the sensor.

The next section introduces a rapidly advancing technology or technological field known as integrated photonics. One of the advantages of integrated photonics is that it allows for in-plane guidance of light, which could potentially solve issues of integration that have been encountered with optical fibres perpendicular to the membrane. Additionally, it could eliminate the acoustic noise that is caused by the damping between a dual-layered structure. This characteristic of integrated photonic technology could be the key to achieving a fully integrated sensitive optic MEMS microphone in the future.

1.2. Integrated photonic microphones

Integrated photonics refers to the integration of multiple photonic components and devices, such as lasers, modulators, detectors, and waveguides, onto a single chip. When silicon is used as the substrate material, it is referred to as silicon photonics. Next to the optic properties, silicon is used as substrate material for its compatibility with existing semiconductor fabrication processes. The optical sensors can be fabricated on standard silicon-on-insulator (SOI) wafers, which are commonly used in the precise and cost-effective complementary metal-oxide-semiconductor (CMOS) process [28].

Silicon photonics can be traced back to the early 1990s and is not a new concept, but due to the advancements in the semiconductor industry new applications are becoming accessible [29]. Currently,

the published research on silicon photonic microphones is limited. A few relevant microphones were published, which are briefly discussed below.

1.2.1. Imec microphone with Mach-Zehnder interferometer

In 2016 Imec (Rochus et al.) developed an analytical model to estimate the sensitivity of optical pressure sensors that use a Mach-Zenhder interferometer [30]. A typical MZI-sensor in silicon photonics is based on two optical waveguides, where the external pressure (or some other external input) changes the length of one arm which modulates the phase of the light. Then these two waveguides are coupled and the interference of both arms changes the intensity of the output signal, see Figure 1.5. The fabricated microphone of which the design and microscopic image can be seen in Figure 1.6. The spirals on the membrane create a longer waveguide, amplifying the membrane's deflection and resulting in a greater change in the length and phase of the light, thereby increasing the sensor's sensitivity. Imec continued to work on this sensor and published a demonstration for an optomechanical microphone [31–33]. The studies focus on an analytical estimation of the linearity and sensitivity of optical pressure sensors, but no competitive performances are presented. Nonetheless, a high sensitivity of 8 mV/Pa is reported, and more research should be done on this type of microphone to optimize for the SNR and dynamic range. Another type of sensor that is commonly found in silicon photonics is the ring resonator, which could also be used to design an integrated photonic MEMS microphone. In ref. [33] it is mentioned that they chose an MZI because it is more robust to laser wavelength noise. The ring resonator is discussed in the next subsection.

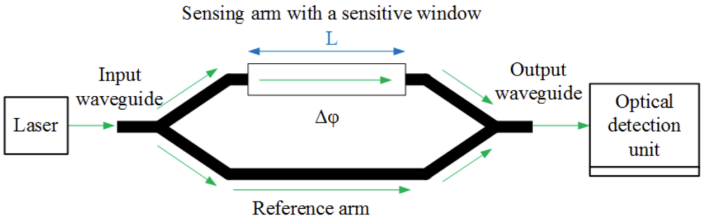

Figure 1.5: Schematic diagram of a typical MZI sensor based on optical waveguides [34]

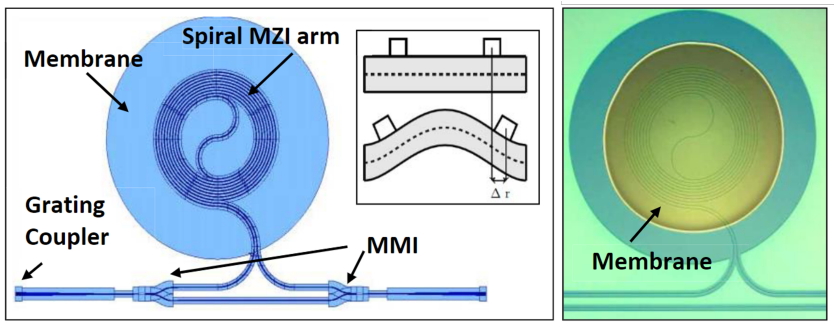

Figure 1.6: Sensor design with integrated waveguides on the membrane of a microphone (left) and a microscopic image of the fabricated device (right), from Ref. [30]

1.2.2. Microphones with a ring resonator

Similar to the MZI presented before, the working principle of a ring resonator relies on the modulation of the light intensity inside a waveguide, by an external effect. I am not aware of any MEMS microphone design that uses an integrated optic ring resonator as a sensor for audio application. A MEMS static pressure sensor that uses a ring resonator on a circular diaphragm was proposed in 2005 by Pattnaik et al., however, the frequency-dependent behaviour of a microphone requires a different approach [35]. In 2015, Leinders et al. introduced a highly sensitive optical micro-machined ultrasound sensor (OMUS) that implements a ring resonator to detect ultrasound sound waves [36]. Note that the reported acoustical resonance frequency is 0.77 MHz, and the device is characterized in water.

Therefore, the re-evaluation of the mechanical design and noise sources for audio frequencies in air is necessary. Westerveld et al. improved the sensitivity of the OMUS by two orders of magnitude by altering the effective index of the cladding of the waveguide, instead of the length of the waveguide [37]. A schematic image of the chip is shown in Figure 1.7. This time the resonance is much higher at around 48 MHZ in air. These studies are of great help to identify sensing techniques, study analytical models and comprehend the challenges of designing an integrated photonic microphone. However, more research is needed to fully understand the implications of using silicon photonics for specifically an audio microphone. Additionally, the extensive knowledge found in the MEMS capacitive microphone industry offers a great foundation to research a MEMS integrated photonic microphone.

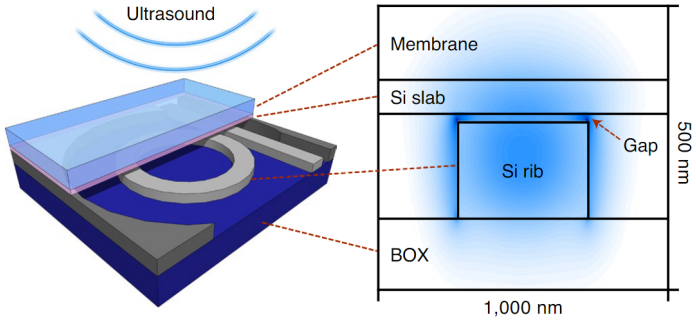

Figure 1.7: Schematic overview of a silicon photonic ultrasound sensor, which uses a change in the effective index of the cladding (gap + Si slab) to sense ultrasound.

1.3. Outline of this thesis

Currently, capacitive MEMS microphones are reaching their bottlenecks and improvements become more and more challenging. In particular, the backplate and ASIC noise are limiting the SNR of such microphones. Modern-day fabrication accuracies achieved by the CMOS fabrication process allow for a new approach, known as integrated photonics. The high sensitivity, planar sensors, cost-effective fabrication and different electronic read-out make that integrated photonic MEMS microphones have the potential to replace the widely adopted capacitive microphone. Especially the signal-to-noise ratio can be significantly improved by eliminating the acoustic backplate noise and reducing the ASIC noise.

From the state of the art of capacitive MEMS microphones, it is evident that analysis and understanding of the acoustic noise in a MEMS microphone are essential to achieve high-quality performance. Furthermore, the implementation of silicon photonics requires a good understanding of the available sensing techniques to optimize the design of a silicon photonic microphone. This thesis combines the implementation of an integrated photonic sensor with the extensive acoustic noise analysis of current capacitive microphones to propose a final design of the silicon photonic microphone. The aim is to eventually outperform capacitive microphones with a silicon photonic one. The research question that has been formulated is:

How can the signal-to-noise ratio (SNR) of a silicon photonic microphone that uses a ring resonator be optimized?

To answer the research question, several subjects are studied. The thesis starts with a background chapter (chapter 2) in which the capacitive microphone is studied in-depth together with the relevant theory of acoustics, and lastly, the background knowledge regarding silicon photonics is presented. The next chapter (chapter 3) discusses the design of a silicon photonic microphone and introduces the design options that are considered and compared. In chapter 4 the models that were used to calculate and compare the thermo-acoustic noise are presented. Next, in chapter 5, the optomechanical models that were used to calculate and compare the sensitivity of the microphone are presented. In chapter 6 the outcome of both models is presented. Additionally, the optimization problem is written which also includes a rough estimation of photonic noise. The chapter finishes with the final design to achieve the highest SNR.

Key parameters MEMS microphone		
Parameter	**Explanation**	**Expression**
Sound Pressure Level (SPL)	The input pressure related to the threshold of human hearing defined as $p_{tr} = 20\mu$Pa; 94 dB SPL equals 1 Pa.	$20\log(p/p_{tr})$ = dB SPL
Sensitivity	For an analogue microphone the sensitivity is the voltage per pressure, evaluated at 1 kHz.	dBV/Pa or mV/Pa
A-weighting	Amplitude modification to account for relative loudness perceived by the human ear.	dB(A)
Signal-to-noise ratio (SNR)	The ratio of the signal and the self-noise of the microphone at a pressure of 1 Pa, evaluated at 1 kHz.	dB
Total Harmonic Distortion (THD)	The ratio of the sum of powers of all harmonic frequencies to the power of the fundamental frequency (typically 1 kHz).	Percentage %
Acoustic overload point (AOP)	Maximum detectable SPL before significant distortion occurs, often defined as 10% THD at 1 kHz.	dB SPL
Size	Scaling down often worsens the SNR, typical package sizes are 3.25mm x 2.5mm x 1mm, diaphragm diameters are typically around 1 mm.	-

Table 1.1: Explanation of the key parameters of a MEMS microphone [1, 8, 38].

2 Background

This chapter aims to give all the background information required to come to the final optimized design. It is meant to provide more background into specific topics, but it is possible to read the thesis without reading the background chapter. For example, sometimes I present only the equation in chapters 3 - 6, with a reference to the background section for more information.

The chapter starts with a more extensive analysis of capacitive microphones. The aim is to understand design choices in the current industry and be able to comprehend whether the same principle applies to a silicon photonic microphone. Then the basics of acoustics are presented. This is useful to understand how the acoustic noise is modelled later in chapter 4. The chapter finishes with a background in silicon photonics, which is required to understand the optomechanical modelling in chapter 5.

2.1. Capactive MEMS microphones

This section provides the functionalities, manufacturing and theory on the capacitance of the design of MEMS capacitive microphones to explain fundamental principles, current trade-offs in device design, and to understand the main problems. Furthermore, it is explained that the microphone can be mathematically modelled as a mass-spring-damper system, and the mechanical modelling of a circular clamped diaphragm is given. Then follows an explanation of acoustic noise modelling based on the recent publication by Knowles et al. (Shubham et al., 2021) [9], providing background on the most prevalent noise sources. The chapter ends with a literature summary of previously solved issues because eventually, the goal of this chapter is to learn from the well-developed capacitive MEMS microphone.

2.1.1. Overview and functionalities

A schematic overview of a recently published MEMS capacitive microphone is shown in Figure 2.1. The chip is placed on a printed circuit board (PCB), which has an acoustic port to let sound through. There also exist designs that have the acoustic port in the enclosure (metal can in image) [10, 16]. The diaphragm and the backplate form a parallel plate capacitor, for more detail see subsection 2.1.3. The centre and peripheral posts are added to prevent sticking of the diaphragm when the device is exposed to loud noises or bumps. They also improve the effective area of the moving diaphragm, which improves sensitivity. More detail regarding effective area is found in Appendix D. A ventilation hole is placed in the centre of the diaphragm to equalise the pressure between the housing and the atmosphere. The springs in the picture have a low stiffness compared to the thickness of the diaphragm, and therefore the vibration happens in a piston-shaped motion. Consequently, more surface area moves towards and away from the backplate such that the change in capacitance that can be measured is larger compared to a membrane-shaped motion.

Next to the MEMS device, the ASIC is placed. It is an electrical semiconductor device that enables a usable output signal of the microphone. Usually, it consists of amplification, filtering, and depending on the application an analogue-to-digital converter (ADC) plus left or right channel assignation is added. It also supplies the bias voltage of the capacitor [10].

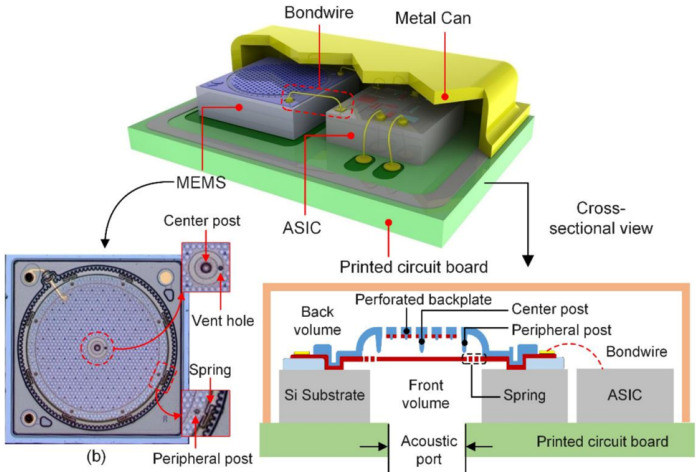

Figure 2.1: Schematic overview of recently published MEMS capacitive microphone, from Ref. [9].

2.1.2. Manufacturing

This section describes the manufacturing process of typical MEMS capacitive microphones [1], which is relevant to understand current MEMS microphone designs. A simplified process flow is shown in Figure 2.2. The basic layer consists of silicon (blue) and silicon oxide (green). The membrane can be made of different materials with common thickness in the order of $1\,\mu$m and diameter of approx. 1 mm and is structured with a lithography process. Then a sacrificial oxide layer is deposited that determines the gap height x_0 between the membrane and backplate, usually in the order of $2-4\mu$ m. The backplate is deposited on the sacrificial layer and usually consists of a polycrystalline silicon layer (blue), the part of the capacitor, on top of a silicon nitride layer (red), which adds isolation between the membrane and backplate. The gaps in the backplate that are shown in the figure indicate the perforation holes of the backplate, which also provide access for the last release etch of the silicon oxide layer. Then gaps are etched into the silicon oxide layer for the electric wire bonding pads, usually made with a gold finish to protect them against rust whilst maintaining high conductivity. Then the bottom is etched away using a deep reactive ion etching (DRIE) process. DRIE results in vertical cavity walls as opposed to wet etching, and therefore allows for smaller surface areas of the microphone.

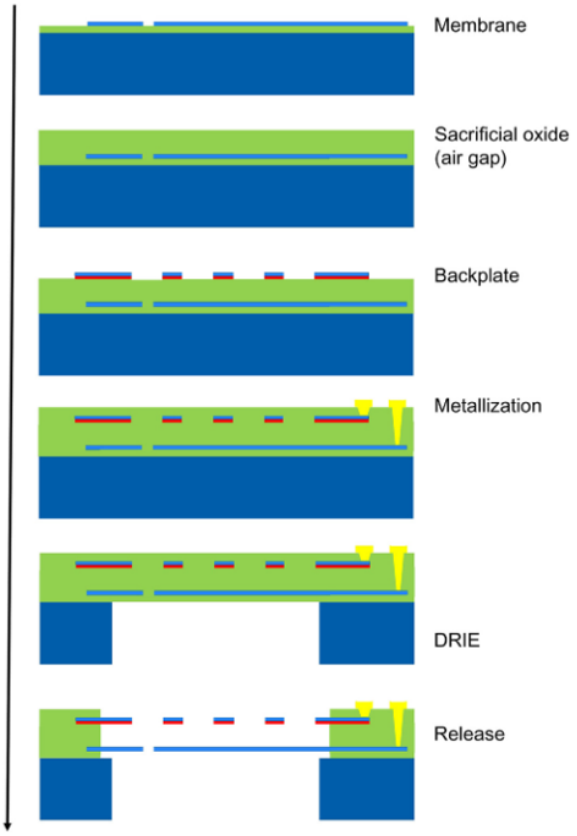

Figure 2.2: Simplified process flow of MEMS capacitive microphone, from Ref. [1].

Lastly, the sacrificial oxide layer is etched away with a release etch. Now the microphone needs to be cut away from the wafer so that it can be attached to another substrate and electronically connected to the ASIC. This process is not relevant to my proposal and is excluded from the report. More details about this process can for example be found in [10].

2.1.3. Theory on capacitance

Capacitive MEMS microphones use capacitance to convert sound pressure into an electric signal [39]. The relation between capacitance C, total charge q and voltage V for two parallel plates is:

$$C = \frac{q}{V} \tag{2.1}$$

For a parallel plate capacitor, the distance g_0 between the plates is sufficiently small compared to its area A, and the capacitance is accurately described by:

$$C_0 = \epsilon_0 \epsilon_r \frac{A}{g_0} \tag{2.2}$$

Where ϵ_0 is the permittivity of vacuum and ϵ_r is the relative permittivity of the material between the two plates (equal to 1 for air). If a change in the distance between the plates is caused by the external pressure $x(p)$, and constant charge $q = Q_0$ due to the applied bias voltage V_0 is assumed (for audible frequencies this assumption holds), the voltage can be rewritten as [1]:

$$V = \frac{Q_0}{C} = \frac{(g_0 + g(p))}{g_0} \frac{Q_0}{C_0} = \frac{(g_0 + g(p))}{g_0} V_0 \tag{2.3}$$

Now the sensitivity S of the capacitive parallel plate microphone is determined by [1]:

$$S = \frac{dV}{dp} = \frac{V_0}{g_0} C_m \tag{2.4}$$

With p the external pressure and $C_m = \frac{dg(p)}{dp}$ the membrane compliance in $[\frac{m}{Pa}]$ given by the average deflection of the membrane per pressure load. A fundamental limit to the sensitivity of capacitive MEMS microphones is the pull-in voltage V_p for which the electrostatic force between the backplate and membrane exceeds the mechanical stiffness of the membrane. The result is a failure of the system because the membrane attaches to the backplate. The pull-in voltage is given by [1, 39, 40]:

$$V_p = \sqrt{\frac{8 g_0^3}{27 \epsilon_0 C_m}} \tag{2.5}$$

Combining Equation 2.4 and 2.5 gives a final sensitivity function:

$$S = \frac{V_0}{V_p} \sqrt{\frac{8 g_0 C_m}{27 \epsilon_0}} \quad \text{with} \quad V_0 < V_p \tag{2.6}$$

The compliance of a fully supported circular plate is further discussed in section 5.1. From Equation 2.4 it is noted that a lower gap distance results in a higher sensitivity of the capacitive microphone. However, negative acoustic effects become more dominant when the gap distance is reduced. This issue still exists with capacitive microphones and is further discussed in subsection 2.2.9.

2.1.4. Historical background indicating previous problems and solutions

By now, many encountered issues have been discussed for MEMS capacitive microphones. In this section, previous solutions that have been published for issues related to a MEMS capacitive microphone are summarized. It is important to note that these solutions are not directly applicable to the current process, but they serve as a valuable source of information and historical background. The purpose is to prevent or solve similar problems in the design process of this project.

As early as 1992, the acoustic damping of the backplate in a silicon microphone was reported as a problem. Studies at that time improved the design of the backplate of the silicon microphone with holes to deal with acoustic damping [41] [42]. Recently, in 2020 Naderyan et al. added an analytical model to optimize the radius of the perforation holes for a fixed perforation ratio [43].

The residual stresses of the fabrication process can be problematic for the compliance and design of the diaphragm. Scheeper et al. (1994) introduced corrugated membranes to deal with residual stresses in the membrane layer due to the fabrication processes [44]. A finite-element analysis to optimize these corrugated structures was conducted by Ying et al. (1998) [45].

Another part of the MEMS capacitive microphones focuses on the implementation of so-called network modelling. It was mentioned that an analytical model for a large range of design parameters is desirable for network modelling, and this is done by Fuldner et al. (2005) [46]. Simplified network modelling is still the common method to design a MEMS microphone and predict its behaviour because it simplifies the complex nature of the coupled acoustical, mechanical, and electrical components [9]. The theory on network modelling can be found in examples for different applications in [8, 12, 20, 47–52].

2.2. Acoustics

This section provides the background knowledge on acoustics that has been studied during this thesis. The purpose of acoustic theory is to understand where the acoustic thermal noise calculations come from. The section starts with the acoustic wave equation, which is followed by an explanation of acoustic radiation and impedance. Then, the radiation impedance of a baffled piston is derived. Other significant acoustic elements relevant to microphone design include closed-pipe and Helmholtz resonances, which will be briefly discussed. Additionally, the compliance of a volume is presented, which is used to model impedances of the back and front volume of a microphone. The section ends with an overview of the noise sources that are presented in several capacitive MEMS microphone studies.

2.2.1. Acoustic wave equation

The basics of acoustics will be briefly explained to understand where later equations are coming from. I used the book of Kinsler [53] for the derivation of this subsection. Acoustic processes are nearly isentropic. This assumption is not completely correct and some acoustic energy is converted into random thermal energy, but for some derivations this assumption holds. When the gas is assumed to be ideal with isentropic compression the relation between pressure p and density ρ is given by:

$$\frac{p}{p_0} = \left(\frac{\rho}{\rho_0}\right)^y \tag{2.7}$$

where y is the ratio of specific heats. When the gas is not assumed as ideal, and fluctuations in density are assumed to be small, the relationship between pressure and density can be approximated by the first-order Taylor expansion:

$$p = \left(\frac{\partial p}{\partial \rho}\right)_{\rho_0} (\rho - \rho_0) \tag{2.8}$$

where ρ_0 equals the initial density. For a small volume element $dV = dxdydz$ through which mass flows, the net rate of mass flow into the volume must equal the rate of mass increase within the volume. This leads to the following continuity equation:

$$\frac{\partial \rho}{\partial t} + \nabla(\rho \mathbf{u}) = 0 \tag{2.9}$$

where **u** is the velocity of the flow into the volume and $\nabla = \frac{\partial}{\partial x} + \frac{\partial}{\partial y} + \frac{\partial}{\partial z}$. When it is assumed that the volume element has a time-dependent velocity $\mathbf{u}(x, y, z, t)$, following Newton's second law the linear Euler's equation is derived as [53]:

$$\rho_0 \frac{\partial \mathbf{u}}{\partial t} = -\nabla p \tag{2.10}$$

which is only valid for acoustic processes of small amplitude. Equation 2.8, 2.9 and 2.10 can be combined into a single differential equation with one variable, known as the linear lossless wave equation of the propagation of sound:

$$\nabla^2 p = \frac{1}{c_0^2} \frac{\partial^2 p}{\partial t^2} \tag{2.11}$$

where c_0 is the speed of sound defined by $c_0^2 = \left(\frac{\partial p}{\partial \rho}\right)_{\rho_0}$. Note that this is the relation of propagation of sound only, so no external sources are considered. This equation can be used to understand the

energy required to, for example, radiate sound from a transducer. The easiest form to study is a spherical harmonic wave with radiation equal in all directions:

$$\frac{\partial^2 p}{\partial r^2} + \frac{2}{r}\frac{\partial p}{\partial r} = \frac{1}{c_0^2}\frac{\partial^2 p}{\partial t^2} \tag{2.12}$$

The complex solution of Equation 2.11 for a harmonic plane wave moving along the x axis is:

$$p(x,t) = Ae^{j(\omega t - kx)} + Be^{j(\omega t + kx)} \tag{2.13}$$

with $k = \omega/c = 2\pi/\lambda$ the wavenumber which is also referred to as propagation constant, A the amplitude of the wave travelling in the $+x$ direction and B the amplitude of the wave travelling in the $-x$ direction. The complex solution of Equation 2.12 for a harmonic spherical wave is equal to:

$$p(r,t) = \frac{A}{r}e^{j(\omega t - kr)} \tag{2.14}$$

This is an important result because it defines the wave propagation coming from a radiating sphere, which defines a point source when the radius a is small. The amplitude A can be calculated at $r = a$ because the velocity at the edge of the sphere is equal to the velocity of the sphere. When it is assumed that a sphere is moving with complex velocity $\mathbf{u} = U_0 e^{j\omega t}$ and displacements are small relative to the radius ($U_0/\omega << a$) the amplitude becomes:

$$A = \rho_0 c_0 U_0 a \cos(\theta_a) e^{j(ka + \theta_a)} \tag{2.15}$$

where θ_a indicates the phase delay between the pressure at the surface of the sphere and the velocity of the surface of the sphere and is defined as $\cot(\theta_a) = ka$, known as the Helmholtz number. When the radius is small compared to the wavelength, $\theta_a \to \pi/2$ and the complex pressure at $r > a$ becomes (from Equation 2.14):

$$p(r,t) = j\rho_0 c_0 U_0 ka \frac{a}{r} e^{j(\omega t - kr)}, \qquad ka << 1 \tag{2.16}$$

Using the reciprocity rule in free space [53], the pressure amplitude for a simple source ($ka << 1$) is equal to:

$$P = \rho_0 c_0 U_0 k \frac{a^2}{r} \qquad \text{(simple source)}$$

$$P = 2\rho_0 c_0 U_0 k \frac{a^2}{r} \qquad \text{(simple source in rigid baffle)}$$

When the source is put inside an infinite rigid baffle (a plane that reflects acoustic waves), the pressure amplitude P doubles. With a derivation of the pressure wave created by the simplest form of a radiator, it is possible to derive the pressure due to the vibration of a piston in an infinite baffle. In terms, the radiation of a baffled piston can be used to calculate the forces of the radiation on the piston which is useful for a microphone as well. The radiation of a baffled piston is discussed in the next section.

2.2.2. Acoustic radiation of a baffled piston

When the diaphragm moves, sound waves are emitted through air as acoustic radiation. A well-known analytical solution to simulate this vibration is the radiation from a piston inside an infinite baffle. This solution is still used in current MEMS microphone modelling [9, 12] and therefore, an in-depth analysis of the radiation from a baffled piston is given in this subsection. The derivations presented closely follow the derivations from Kinsler [53] and Blackstock [54].

A baffled piston is a large fixed area of which a small section, the piston, is able to vibrate normal to the plane. A schematic overview is shown in Figure 2.3. A general solution for the pressure field produced by the vibration of a piston mounted in a rigid baffle is the Rayleigh integral, given in Equation 2.18:

$$p(x,y,z,t) = \rho_0 \int_S \frac{\mathbf{u}(x^*,y^*,0,t-R/c_0)}{2\pi R} dS \tag{2.18}$$

with $\mathbf{u}(x*,y*,0,t-R/c_0)$ the average velocity normal to the plane of a surface element dS and $R = \sqrt{(x-x^*)^2+(y-y^*)^2+z^2}$ the distance from the surface area element to the evaluation point P. Note that there only exists a pressure for $t => R/c_0$ since the pressure wave has to arrive at the evaluation point. The rigid baffle restricts the radiation to only a hemisphere. Equation 2.18 is the result of modelling each surface element dS as a single source placed in an infinite baffle and integrating over the surface area. For a piston with uniform time harmonic vibration $u_p = u_0 e^{j\omega t}$ the integral becomes:

$$p(x,y,z,t) = \frac{j\rho_0 c_0 u_0 k e^{j\omega t}}{2\pi} \int_S \frac{e^{-jkR}}{R} dS \tag{2.19}$$

Note that when the velocity is not equal over the surface of the piston, for example when examining a clamped circular plate which has no piston-like motion, the velocity of surface element dS should be included in the integral. It is possible to simulate a vibrating clamped diaphragm as a circular piston motion with effective area A_e, so for now we leave the velocity outside the integral.

Since we are designing a microphone we are not interested in the pressure field created by actively vibrating the diaphragm (which is only interesting for a speaker/transmitter). However, when the incoming sound waves vibrate the diaphragm, the pressure field still exists. The energy that is lost through this radiation affects the motion of the diaphragm as a mechanical impedance, known as radiation impedance. The next subsection will analyse this radiation impedance.

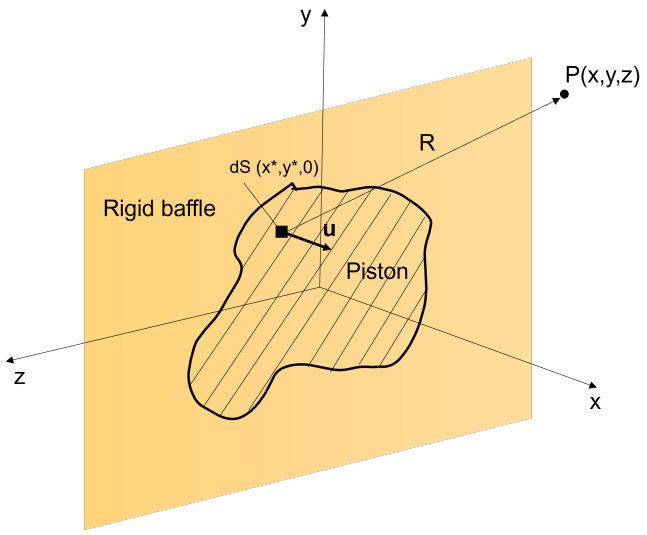

Figure 2.3: Schematic overview of rigid baffled piston with the indication of a small surface element dS.

2.2.3. Acoustic Impedance

Acoustic impedance is a measure of the opposition that a medium offers to the flow of sound waves. Three types of impedances are commonly used in acoustics [55] :

1. $Z_a = \frac{p_{av}}{Q}$ is the acoustic impedance given by the ratio of average sound pressure at a surface to the volume velocity of the fluid through the surface.
2. $Z_{sa} = \frac{p}{u}$ is the specific acoustic impedance given by the ratio of the pressure at a point to the particle velocity at that point.
3. $Z_m = \frac{F}{u}$ is the mechanical impedance given by the ratio of the force acting on a specified area to the particle velocity of that area.

Acoustic impedance can be used directly in circuit modelling, which is explained in section 4.1. Additionally, it is possible to define the acoustic impedance as a mechanical impedance Z_m, which

is suited for mass-spring-damper modelling. This is explained in Appendix B. Lastly, the acoustic impedance is used to derive the thermal acoustic noise. This is explained later, in chapter 4.

2.2.4. Radiation Impedance

Beranek [55] has an understandable definition of radiation impedance: ”a quantitative statement of the manner in which the medium reacts against the motion of a vibrating surface.” It has both a real and complex part so therefore, solely thinking of radiation impedance as resistance to radiation does not suffice as a complete explanation. A broad analysis of the quantity is discussed in [56]. This subsection summarizes the relevant parts coming from this paper and the literature that is cited there.

We are interested in the mechanical radiation impedance to calculate how the motion of the diaphragm is affected. The total mechanical radiation impedance of the air load on the vibrating surface can be separated into radiation resistance R_m and radiation reactance X_m and is defined as:

$$\boldsymbol{Z}_{mr} = \frac{F_s}{u} = R_{mr} + jX_{mr} \tag{2.20}$$

The real resistance part accounts for the energy required to radiate sound into the surroundings, the imaginary reactance part accounts for the energy required to move the air that is not radiated further, and is often referred to as mass loading. At low frequencies, the impedance is dominated by the reactance, and the surface velocity lags behind the pressure of the medium right next to it by app. 90°. It is useful to understand that for sinusoidal motion the surface displacement lags behind the surface velocity by 90° as well, resulting in a phase lag of app. 180° between surface displacement and pressure. For high frequencies, the impedance is dominated by the resistance and the surface velocity and pressure of the adjacent medium are in phase. About this phenomenon, Blackstock [54] mentioned that ”an analysis of the impedance presented to the source by the medium leads to useful conclusions about the efficiency of spherical radiators”.

For a diaphragm with area S that has a normal force $\boldsymbol{f}_S$ on an element dS of the vibrating surface, the mechanical radiation impedance is found by integrating the force over the surface area [53]:

$$\boldsymbol{Z}_{mr} = \int_S \frac{\boldsymbol{f}_S}{\mathbf{u}} dS \tag{2.21}$$

For uniform vibration of the piston $\mathbf{u} = u_0 e^{j\omega t}$ driven by an external force $\boldsymbol{F} = F_0 e^{j\omega t}$ the equation of motion that includes radiation impedance is:

$$m\ddot{x}(t) + R_m\dot{x}(t) + kx(t) = \boldsymbol{F} - \boldsymbol{F}_S \tag{2.22}$$

with m the mass of the piston, R_m the mechanical resistance, and uniform stiffness k. The mechanical impedance in vacuum is:

$$\boldsymbol{Z}_{mv} = R_m + j(\omega m - \frac{1}{\omega}k) \tag{2.23}$$

and solving for $\mathbf{u}$ gives:

$$\mathbf{u} = \frac{\boldsymbol{F}}{\boldsymbol{Z}_{mv} + \boldsymbol{Z}_{mr}} \tag{2.24}$$

To solve the integral in Equation 2.21 we need to introduce another surface element dS' (see Figure 2.4). Now let $d\mathbf{p}$ be the pressure that the motion of dS produces at another surface element dS' so that the total pressure is found by integrating $d\mathbf{p}$ over the surface area S. As mentioned before, each surface element dS is modelled as a simple baffled source and the total pressure on a single element dS' becomes [53]:

$$\mathbf{p}(r,t) = j\rho_0 c_0 \frac{u_0}{\lambda} \int_S \frac{1}{r} e^{j(\omega t - kr)} dS \tag{2.25}$$

where in this case r denotes the distance between two surface elements. The integration to find the total pressure $\mathbf{p}$ to finally calculate $\boldsymbol{F}_S$ should include both a force on dS' due to the motion of dS and vice versa. From the acoustic reciprocity rule, these two forces must be equal so that the result is

simplified as just twice the force on dS due to the motion of dS. Now the total force is computed as twice the pressure at surface area dS due to motion of dS', integrated over the whole surface area S [53]:

$$\boldsymbol{F}_S = 2j\rho_0 c_0 \frac{u_0}{\lambda} e^{j\omega t} \int_0^a \int_0^{2\pi} \int_{-\pi/2}^{\pi/2} \int_0^{2\sigma\cos\theta} \sigma e^{-jkr}\, dr\, d\theta\, d\psi\, d\sigma \tag{2.26}$$

The extra variable σ is introduced to make sure that each surface element dS' only contributes once to the pressure at dS (and vice versa). Following Figure 2.4 a ring of surface elements dS' is defined at a circle with radius σ. Within the ring, the maximum distance r between two surface elements is equal to $2\sigma\cos\theta$ and by integrating r from 0 to $2\sigma\cos\theta$ and θ from $-\pi/2$ to $\pi/2$ the distance between dS' (that lies at radius σ) to each surface element dS within the circle of radius σ is found. Now if we set $dS' = \sigma d\sigma d\psi$ and integrate from ψ from 0 to 2π and σ from 0 to a, the entire surface or the piston is covered. Finally, the total mechanical radiation impedance on a circular piston in an infinite rigid baffle is [54]:

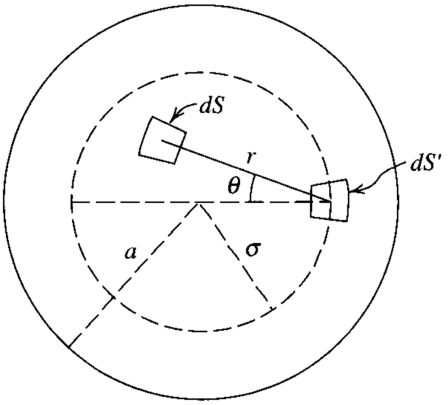

Figure 2.4: Circular piston to indicate new variables and extra surface element dS', from ref. [53]

$$\boldsymbol{Z}_{mr} = \frac{\boldsymbol{F}_S}{\mathbf{u}} = \rho_0 c\pi a^2 \left[1 - \frac{J_1(2ka)}{ka} + j\frac{H_1(2ka)}{ka}\right] \tag{2.27}$$

where J_1 is the first order Bessel function and H_1 the first order Struve function. If we now compare Equation 2.21 to Equation 5.9, we can see that:

$$\boldsymbol{Z}_{mr} = \rho_0 c\pi a^2 \left(R_{mr} + jX_{mr}\right) \tag{2.28}$$

where the resistance is equal to $R_{mr} = 1 - \frac{2J_1(2ka)}{2ka}$ and the reactance is equal to $X_{mr} = \frac{2H_1(2ka)}{2ka}$. For increasing values of $2ka$ the resistance and reactance are plotted in Figure 2.5a. For small values of $2ka$, which is the case for miniature diaphragms, the radiation impedance is dominated by the reactance (see Figure 2.5b). Therefore, radiation impedance will be acting as mass loading in the case of a MEMS microphone.

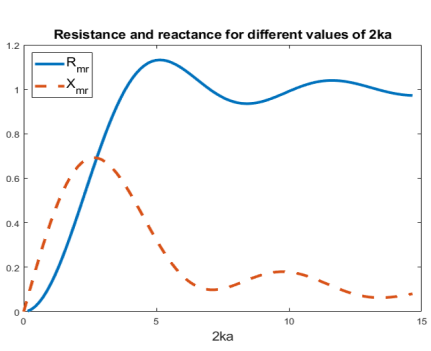

(a) Large range of values of $2ka$.

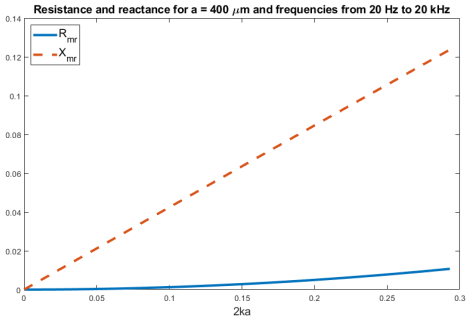

(b) Values of $2ka$ for $a = 400\mu m$ and frequencies from 20 to 20000 Hz.

Figure 2.5: Resistance R_{mr} and reactance X_{mr} plotted for different values of $2ka$

2.2.5. Thermal and viscous boundary layer

This section is added for a further understanding of acoustics in general. The analysis of thermal and viscous boundary layers in this thesis is only on a basic level, and this section is mostly based on Ref. [57].

When sound waves travel past walls, thermal and viscous boundary layers are created. Often there is referred to as something called a no-slip condition, which indicates that the particle velocity is equal

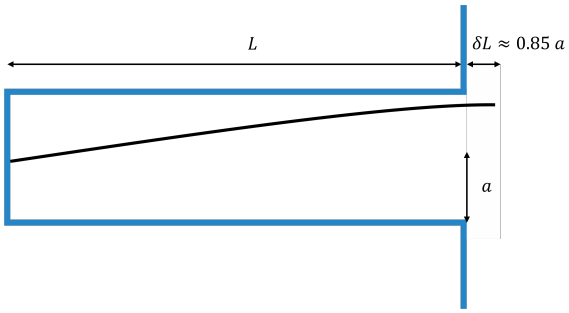

Figure 2.6: Closed pipe resonance with an indication of the end correction due to the viscosity of air [58].

to zero and the isothermal condition for the temperature is also equal to zero (not zero Kelvin, but zero difference with ambient temperature). The gradient of the velocity and temperature profile is the largest close to the wall, and so are the losses. This means that for systems near the size of the viscous or thermal boundary layer, the boundary layer losses are essential to include in the modelling. The sizes of the viscous and thermal boundary layers can be calculated with [57]:

$$\delta_{visc} = \sqrt{\frac{2\mu}{\omega\rho_0}} \tag{2.29a}$$

$$\delta_{therm} = \sqrt{\frac{2k}{\omega\rho_0 C_p}} \tag{2.29b}$$

where μ is the dynamic viscosity, k the coefficient of thermal conductivity, C_P the specific heat capacity at constant pressure, ω the frequency and ρ_0 the density. For air at 100 Hz, 20 $^\circ$ C and 1 atm, the viscous boundary layer is equal to 0.22 mm, which is almost equal to the thermal boundary layer.

Consequently, a diaphragm with a radius of 0.5 mm, has roughly half of its surroundings within the viscous boundary layer at 100 Hz. Note that the boundary layer decreases for higher frequencies, and is only $\approx$0.075 mm for a frequency of 1000 Hz. Nonetheless, the viscous boundary layer should be considered or at least kept in mind during the design process of a silicon photonic microphone.

2.2.6. Closed-pipe resonance

A well-known acoustic resonance to consider is the closed-pipe resonance. In Figure 2.6 a schematic overview is shown, where the length of the pipe includes the end correction caused by the viscosity of air. For the microphone, the closed pipe is formed by the diaphragm and the front port. The length of the front port is determined by the thickness of the silicon substrate and the printed circuit port on which it is mounted. The resonance occurs when the length of the pipe is a fourth of the wavelength. The resonance should be well above the audible frequency range to ensure that audible frequencies are not modulated. The shortest wavelength of audible frequencies corresponds to the highest frequency:

$$\lambda = \frac{c}{f} = \frac{343}{20000} = 17\text{mm} \tag{2.30}$$

In the case of microphone ports, the length is often below 1 mm so closed-pipe resonance will not be a problem. However, the microphone should not be mounted on a thick piece of PCB to keep the resonance above audible frequencies. Another well-known acoustic resonance is the Helmholtz resonance, which is explained in the next subsection.

2.2.7. Helmholtz resonance

A Helmholtz resonator is a specific type of acoustic resonator which is commonly found in acoustics. A schematic overview is given in Figure 2.7. The classical resonator is shown on the left side in blue. It can be thought of as a mass-spring-damper system, where the spring is formed by the volume that is compressed and the mass is formed by the air in the neck [54]. Damping occurs because of viscous losses and radiation. The surface area of the neck should be smaller than the volume, otherwise, it would be a simple open pipe. Now consider sound pressure outside the resonator. When air flows

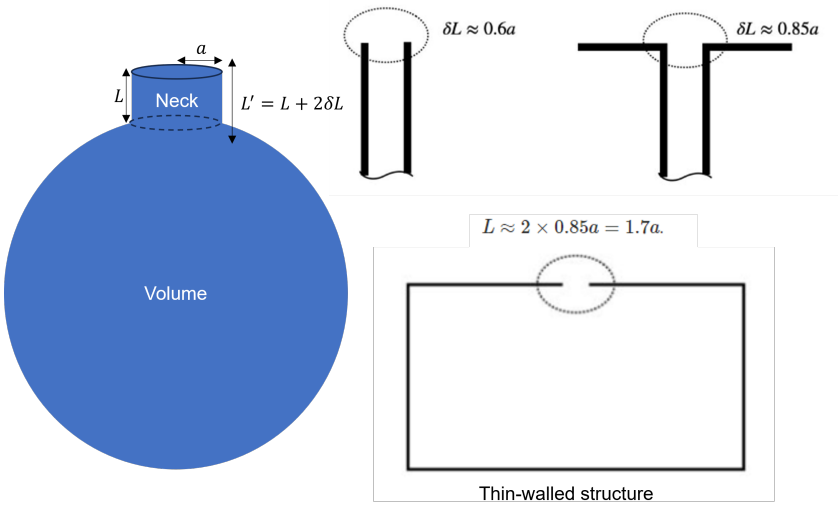

Figure 2.7: Schematic overview of a Helmholtz resonator (left) indicating the neck and volume. Furthermore, the end corrections (right) due to the viscosity of air are shown for two types of neck endings. For a thin-walled structure, the neck length is approximately equal to twice the end corrections [59].

inside the volume through the neck due to the acoustic pressure, air will flow through the neck and the pressure inside the volume increases. As the outside pressure drops again, the extra pressure inside the volume will cause the air to flow outside through the neck again. For a specific frequency, resonance occurs, depending on the geometry of the resonator. The resonance frequency in Hertz can be found as:

$$f_0 = \frac{c}{2\pi}\sqrt{\frac{\pi a^2}{L'V}} \tag{2.31}$$

with V the volume below the neck, L' the effective length of the neck, which includes end effects due to viscosity, c the speed of sound and a the radius of the neck. In microphones, the substrate on which the microphone is connected (PCB) often has a smaller radius than the inlet port, and therefore the substrate forms the neck of a Helmholtz resonance, with the front cavity as the corresponding volume. In any case, the Helmholtz resonance should be considered if it is unavoidable, and the resonance must be kept well above the audible frequencies.

2.2.8. Pipe resistance: Hagen-Poiseuille equation

A reoccurring equation in the acoustic analysis of a microphone is the Hagen-Poiseuillie equation. It calculates the volume flow due to a pressure difference through a cylindrical pipe of a certain medium, which includes viscous losses [60]:

$$Q = \frac{\Delta p \pi a^4}{8\eta L} \tag{2.32}$$

with Q the volume flow in cubic meter per second, a the radius op the cylinder, L the length of the cylinder, Δp the pressure difference and η the dynamic viscosity of the medium. This translates to acoustic resistance as:

$$R = \frac{\Delta p}{Q} = \frac{8\eta L}{\pi a^4} \tag{2.33}$$

The equation only holds for laminar well-developed flow and is not precise for short pipe lengths. However, these are still used to model for example the port resistance in current microphone acoustic models [9]. The next subsection presents how different acoustic noise sources are modelled in current capacitive MEMS microphones.

2.2.9. Noise sources

In the introduction, the dominant noise power contributions and their sources were presented in Figure 1.2. This section gives more detail about the acoustic noise sources. The acoustic noise power is related to the acoustic noise spectral density and both the measured and simulated versions are shown in Figure 2.8.

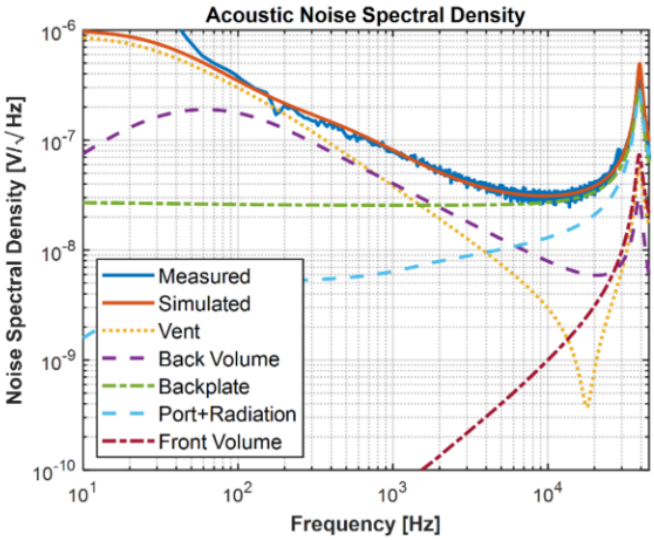

Figure 2.8: Plot that shows simulated and measured noise spectral density, where the simulated contributions are separated for each individual; from Ref. [9].

To calculate the noise spectral density, the fluctuation-dissipation theorem (FDT) is used. It states that for each source of dissipation (absorption of energy, e.g. friction), there is a reaction as thermal fluctuation (kinetic energy) [61]. In the context of thermo-acoustic noise, it means that the drag experienced by any airflow dissipates the kinetic energy of the air into heat. According to the FDT this heat results in the random motion of air particles (known as Brownian motion). These random motions cause small fluctuations in the gas density, resulting in pressure fluctuations, measured as noise. To quantify the magnitude of the thermo-acoustic noise, the sources of dissipation must be analysed [12, 43, 62]. Each individual source of dissipation can be added to find the total noise magnitude [9]. Each source will now be discussed below to gain more insight into how the results were obtained.

Backplate

The most dominant acoustic noise comes from the backplate and can be separated into two effects:

1. Squeeze-film damping (SFD) between the two plates
2. Viscous damping when air flows through the perforation holes

The squeeze-film damping in MEMS has been thoroughly analysed by [63]. For small displacements of two parallel plates, the normalized and linearized Reynolds equation for a compressible gas is given as:

$$\left(\frac{\partial^2 \tilde{p}}{\partial \tilde{x}^2} + \frac{\partial^2 \tilde{p}}{\partial \tilde{y}^2}\right) - \sigma \frac{\partial \tilde{p}}{\partial \tau} = \sigma \frac{\mathrm{d}\tilde{g}}{\mathrm{d}\tau} \tag{2.34}$$

where $\tilde{p} = p/p_a$ is the external pressure normalized to the atmospheric pressure, $\tilde{x} = x/l$ and $\tilde{y} = y/l$ are variables normalized to the characteristic length l, $\tilde{g} = h/g_0$ the changing thickness of the film normalized to the original film thickness, $\tau = \omega t$ and σ is the squeeze number:

$$\sigma = \frac{12\eta\omega l^2}{p_a g_0^2} \tag{2.35}$$

where ω is the radial frequency and η the viscosity coefficient of the fluid. Now Equation 2.34 can be solved for a time-harmonic oscillation $g = g_0(1 + \delta \cos(\omega t), \quad \delta << 1$ to find the squeeze-film damping force for a strip plate as:

$$F = P_a A\delta[-f_e(\sigma)\cos(\omega t) + f_d(\sigma)\sin(\omega t)] \tag{2.36}$$

where the force components f_e and f_d depend on the squeeze number and $A = \sqrt{f_e(\sigma)^2 + f_d(\sigma)^2}$ is the amplitude of the damping force (see [64] for more detail); a plot of the resulting force is shown in Figure 2.9.

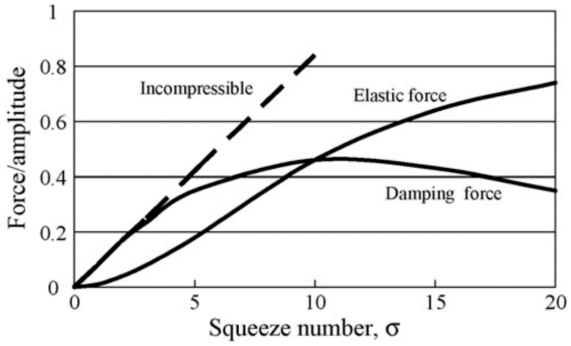

Figure 2.9: Normalized force plotted against squeeze number, with a dotted line added to represent the squeeze-film damping force in an incompressible medium

The damping force relates to the viscous force due to the airflow out of the thin film, and the elastic force relates to the force required to compress the medium. The model of a strip plate is not correct for a perforated backplate. The airflow through the perforation holes reduces the SFD but increases the viscous damping of air, which makes the SFD modelling complex [43]. Recently (2021), Naderyan et al. [65] followed the work of Li et al. [66] on an analytical model to simulate the SFD of a circular perforated backplate for the motion of a circular clamped diaphragm. For a clamped circular plate they found the damping force D and spring force S as:

$$D + jS = \frac{-6\pi j\omega\gamma p_a}{g_0 c_0^2 f(\lambda) a^2 B^2}\left(\frac{64}{B} + \frac{Ba^4}{6}\right) \tag{2.37}$$

with a the radius of the diaphragm, γ the ratio of specific heats, p_a and c_0 again the atmospheric pressure and speed of sound in air, respectively; B is defined as:

$$B = \frac{\hat{\omega}^2}{g_0^2}\left(\frac{\gamma - (\gamma - 1)f(\lambda_\tau)}{f(\lambda)} - \frac{j}{\hat{\omega} f(\lambda)\hat{Z}_{sa}}\right) \tag{2.38}$$

with $\hat{Z}_{sa}$ the dimensionless (normalized) specific acoustic impedance of a perforated backplate defined in Ref. [43]; $f(\lambda)$ and $\hat{\omega}$ are defined as:

$$f(\lambda) = \frac{2\tan(\sqrt{j}\lambda/2)}{\sqrt{j}\lambda} \tag{2.39}$$

$$\hat{\omega} = \frac{\omega g_0}{c_0} \tag{2.40}$$

with λ the dimensionless (normalized) shear wavenumber and λ_τ the thermal wavenumber defined as:

$$\lambda = g_0\sqrt{\frac{\rho_0\omega}{\eta}} \tag{2.41a}$$

$$\lambda_\tau = g_0\sqrt{\frac{\rho_0 C_p\omega}{\kappa}} \tag{2.41b}$$

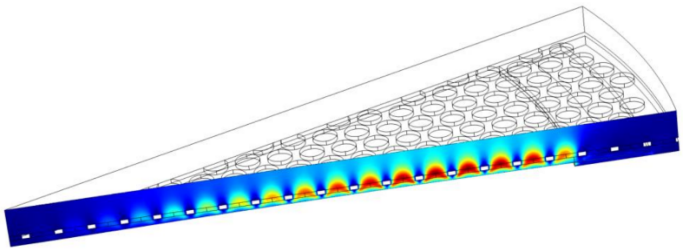

Figure 2.10: Air velocity field cross-section of the backplate to show how acoustics are modelled, from Ref. [9]

The equations above can be used to model the squeeze-film damping of a capacitive MEMS microphone; they can be used to compare the acoustic noise of a MEMS microphone without the backplate to find acoustic improvements. Shubham et al. [9] used a FEM model to find the acoustic damping (resistance) and found $R_{bp} = 1.74 \times 10^8$ Pa $\cdot$ s/m^3. They used the symmetry condition for a slice of the backplate design, as shown in Figure 2.10.

Ventilation hole

Another source of noise comes from the thermo-viscous damping in the ventilation hole. The ventilation hole should not be too large because it would remove the pressure difference between the back and front volume, which is essential for the diaphragm to move. Lower frequencies drop off quicker and the ventilation hole serves as an acoustic high-pass filter [9]. The effect of the location and size of the vent hole has been analysed in ref. [67]. The acoustic resistance is modelled with the Hagen-Poiseuille equation:

$$R_{vent} = \frac{8\eta h_{vent}}{\pi r_{vent}^4} \tag{2.42}$$

with η the dynamic viscosity of air, r_{vent} the radius of the ventilation hole, h_{vent} the height of the material in which the hole is made. Since pressure flows through the diaphragm it is added in parallel with the diaphragm when added to a lumped parameter model (more about this in section 4.1). The effect of different hole sizes is shown in Figure 2.11.

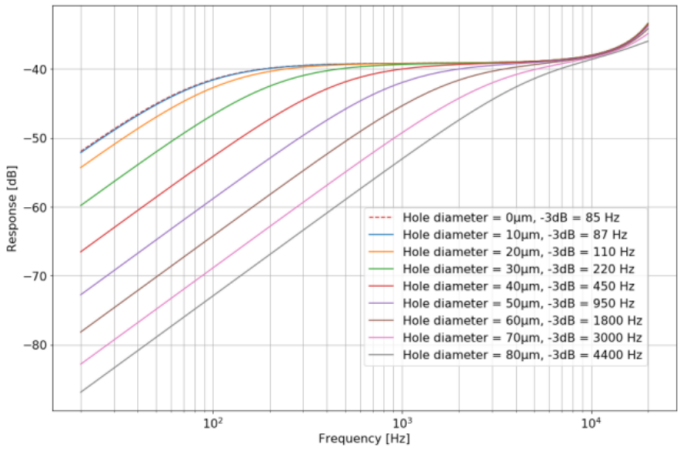

Figure 2.11: Effect of ventilation hole diameter on the frequency response of a MEMS microphone, from Ref. [67]

In [9] there is only a ventilation hole in the diaphragm, and the ventilation resistance is computed by measuring the LFRO, where the back cavity compliance C_b is calculated using the back volume V_b:

$$R_{vent} = \frac{1}{2\pi f_{LFRO} C_b} \tag{2.43}$$

$$C_b = \frac{V_b}{\gamma p_0} = \frac{V_b}{\rho_0 c_0^2} \tag{2.44}$$

This method is also recommended by [67] to calculate the resistance of all the perforations in the diaphragm.

Back volume

The noise coming from the back volume follows the approach from Ref. [12] by Kuntzman et al. (2018), which is summarized in this subsection. For the back volume, a distinction is made between viscous and thermal damping. Previous papers found thermal noise through viscous damping: mechanical kinetic energy irreversibly lost as thermal energy due to frictional forces induced by the viscosity of the medium [68]. It is explained that for such a small scale the assumption of adiabatic (no heat exchange with the environment) compression of sound does not hold. The heat transfer (thermal losses) to the enclosure creates a thermal boundary that results in thermal relaxation losses, which in term increases thermal noise according to the fluctuation-dissipation theorem [12, 61, 62]. The total impedance originates from compression of the back volume, and the heat that dissipates to the housing when the air is compressed. When no heat dissipation is assumed (adiabatic compression), the acoustic impedance is given as:

$$Z_a = \frac{\gamma p_0}{j\omega V_b} = \frac{1}{j\omega C_b} \tag{2.45}$$

Equation 2.44 holds only for adiabatic compression so that the thermodynamic speed of sound for an ideal gas becomes [53]:

$$c_0^2 = \left(\frac{\partial p}{\partial \rho}\right)_{adiab.} = \gamma \frac{p_0}{\rho_0} \tag{2.46}$$

As mentioned, another effect is a significant contribution to the noise: the heat losses to the enclosure. A thermal boundary layer is formed of which the thickness is given by [12]:

$$\delta_t = \sqrt{\frac{2\kappa}{\omega \rho_0 C_p}} \tag{2.47}$$

with C_p the specific heat constant and κ the thermal conductivity of air. It has been shown previously that the thermal boundary layer effects can be added to the acoustic impedance as [69]:

$$Z = \frac{1}{Z_a^{-1} + Z_t^{-1}} \tag{2.48}$$

where the Z_t is the acoustic impedance that results from the heat losses [12]:

$$Z_t = \frac{1}{j\omega C_a(\gamma - 1)\left(1 - \frac{\tilde{T}}{T_a}\right)} \tag{2.49}$$

where T_a is the environmental temperature and $\tilde{T}$ is the spatial average of the amplitude of the temperature oscillation in the cavity due to the acoustic compression. For a thin rectangular parallelepiped enclosure it is given as [70]:

$$\tilde{T} = T_a\left(1 - \frac{\tanh(\beta a)}{\beta a}\right) \tag{2.50}$$

with $\beta = \sqrt{j\omega C_p/\kappa}$. Substituting Equation 2.45, 2.49 and 2.50 into Equation 2.48 results in the final acoustic enclosure impedance:

$$Z = \frac{1}{j\omega C_a\left[1 + (\gamma - 1)\left(\frac{\tanh(\beta a)}{\beta a}\right)\right]} \tag{2.51}$$

The aforementioned noise sources are the main contributors to acoustic noise power. Less dominant acoustic noise sources are radiation impedance (see Equation 2.21), port resistance and front cavity impedance. In Ref.[9] the port resistance is modelled with the Hagen-Poiseuille equation:

$$R_{port} = \frac{8\eta l_p}{\pi a_p^4} \tag{2.52}$$

with time l_p and a_p the port length and radius. The front cavity impedance can be calculated using Equation 2.51, but then with the adiabatic compliance calculated using the front volume V_f instead of the back volume. The size of the front volume is determined by the DRIE etch explained in subsection 2.1.2.

The analysis of noise sources in state-of-the-art MEMS capacitive microphones provides a basis for designing a silicon photonic MEMS microphone with improved acoustic noise modelling. Next, the necessary background knowledge regarding silicon photonics is given.

2.3. Silicon photonics

This section aims to give more background knowledge on the silicon photonics theory. It is meant as a follow-up on the parts that were mentioned in the introduction already. The section starts with an explanation of the waveguides and the related guided TE and TM modes, followed by how these can be used to form optical sensors. Then the ring resonator is explained in more detail as this will be the sensor used for the microphone in this thesis. The theory is mostly taken from ref. [28].

2.3.1. Dielectric waveguides

Photonic sensors integrated within an SOI wafer use waveguides and therefore it is essential to understand what a waveguide is and how it works. A waveguide literally guides a wave, light in this case, by using the principle of internal reflection. Internal reflection can occur because the speed of light is dependent on the medium it passes through. The speed of light inside a medium is often given relative to the speed of light in vacuum, known as the refractive index $n = \frac{\text{speed in vacuum}}{\text{speed in medium}}$. When light meets the intersection of two different media, that have different refractive indices, the propagation angle changes. The incident angle for which the propagation angle changes such that the light remains in the same medium is called the critical angle, see figure Figure 2.12.

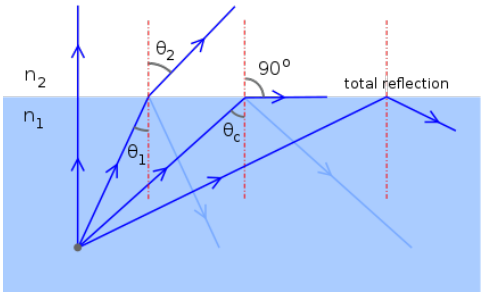

Figure 2.12: Image of change in propagation angle at surface of two different refractive indices. from [71].

The propagation of light in the waveguide is described by Maxwell's equations in terms of electric field $\mathcal{E}$ and magnetic field $\mathcal{H}$. For monochromatic light (single wavelength) in an isotropic linear dielectric medium without charges, the Maxwell's complex equations reduce to:

$$\nabla \times \boldsymbol{\mathcal{E}} = -j\mu_0\omega\boldsymbol{\mathcal{H}} \tag{2.53a}$$
$$\nabla \times \boldsymbol{\mathcal{H}} = j\mu_0\epsilon\boldsymbol{\mathcal{E}} \tag{2.53b}$$
$$\nabla \cdot \epsilon\boldsymbol{\mathcal{E}} = 0 \tag{2.53c}$$
$$\nabla \cdot \boldsymbol{\mathcal{H}} = 0 \tag{2.53d}$$

with μ_0 the vacuum permeability, ϵ the permittivity, and ω the angular frequency. The electric and magnetic field in a homogeneous isotropic medium obeys the Helmholtz wave equation:

$$(\nabla^2 + n^2k^2)\boldsymbol{\mathcal{E}} = 0 \tag{2.54a}$$
$$(\nabla^2 + n^2k^2)\boldsymbol{\mathcal{H}} = 0 \tag{2.54b}$$

with n the refractive index defined as $n = \sqrt{\epsilon/\epsilon_0}$ and $k = \omega/c$ the wavenumber in vacuum. At the edges of a waveguide where two different materials encounter, continuity conditions should be applied for the

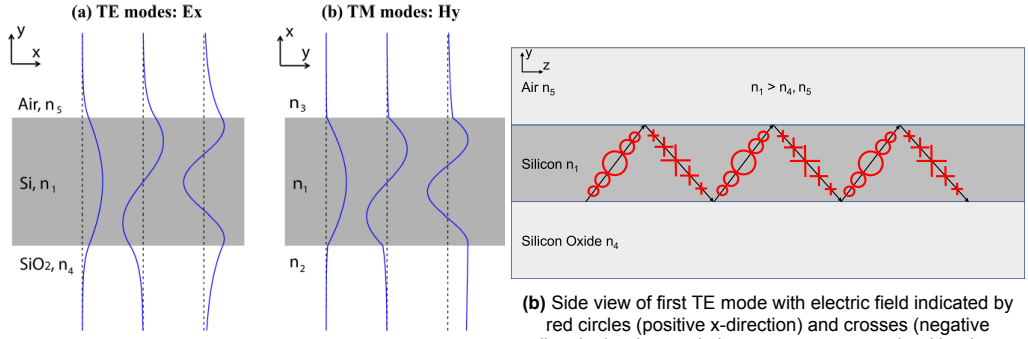

(a) From Ref. [28]

(b) Side view of first TE mode with electric field indicated by red circles (positive x-direction) and crosses (negative x-direction); a larger circle or cross corresponds with a larger electric field. Note that the evanescent field slightly outside the border is not drawn in this picture

Figure 2.13: Visualization of TE and TM modes in slab waveguides [28]

tangential component of both electric and magnetic fields. With these equations, it is possible to derive transverse electric (TE) and transverse magnetic (TM) modes with propagation inside the waveguide and along the edges. These are discussed in the next subsection.

2.3.2. TE- & TM-modes

A transverse mode in electromagnetic radiation refers to a specific pattern of the electromagnetic field within the plane that is perpendicular to the direction of the radiation's propagation. Transverse modes occur due to the waveguide's imposed boundary conditions on the wave. Note that in any case, modes only exist when the refractive index of the core is larger than the effective index, which in term is larger than the effective index of the cladding ($n_{core} > n_{eff} > n_{clad}$). The effective index relates to the propagation speed of the mode. The allowed modes can be found by solving Maxwell's equations for the boundary conditions of a given waveguide. For propagation along the z-axis in a dielectric slab waveguide, TE-modes only have three non-zero field components $\mathcal{E}_x$, $\mathcal{H}_y$ and $\mathcal{H}_z$ that are all defined by the electric field component $\mathcal{E}_x$. Similarly, TM-modes only have non-zero field components $\mathcal{H}_y$, $\mathcal{E}_x$ and $\mathcal{E}_z$ that are all defined by the magnetic field component $\mathcal{H}_y$. When the electric and magnetic field components are assumed as monochromatic propagating wave solutions:

$$\boldsymbol{\mathcal{E}} = E_x(y)e^{j(\omega t-\beta z)}\hat{\mathbf{x}} \tag{2.55a}$$

$$\boldsymbol{\mathcal{E}} = H_y(x)e^{j(\omega t-\beta z)}\hat{\mathbf{y}} \tag{2.55b}$$

The propagation characteristics of dielectric waveguides, particularly for TM and TE modes, can be described through an equation dependent on the propagation constant, refractive indices, and waveguide size. This equation yields zero or more solutions for guided waves, as outlined in Chapter 2.2 of [28], which establishes the finite number of modes present in the slab waveguide. Furthermore, it is possible to derive properties for guided modes in waveguides with permittivity profile $\epsilon(x, y)$, as discussed in Chapter 2.3 of [28].

As shown in Figure 2.13a, a dielectric slab waveguide displays its first three TE and TM modes. Specifically, Figure 2.13b provides a side view of the first TE mode propagating in the z-direction.

For the fabrication of sensors, waveguides are intentionally designed to support only the first TE mode. This approach allows for easier measurement of mode intensity changes caused by external inputs. Each mode possesses its distinct effective index, further emphasizing the significance of isolating a single mode for accurate analysis.

2.3.3. Directional coupler

A directional coupler consists of waveguides so close to each other that light can transfer from one waveguide to the other. The total electromagnetic field $\boldsymbol{\mathcal{E}}^c$ can be approximated by adding the modal electric fields of both waveguides multiplied by a complex modal amplitude u. For two waveguides a and b that means:

$$\boldsymbol{\mathcal{E}}^c(x, y, z, t) \approx \mathbf{E}^a(x, y)u_a(z)e^{j\omega t} + \mathbf{E}^b(x, y)u_b(z)e^{j\omega t} \tag{2.56}$$

If at $z = 0$ all the light is in waveguide b and the coupling length is defined as $\tilde{L}$, the transmission τ defines the amount of light that is still transmitted from the input of waveguide b to the output of waveguide b as $u_b(\tilde{L}) = \tau u_b(0)$. Similarly, the amount of light that is coupled from the input of waveguide b to the output of waveguide a is defined by the coupling coefficient κ as $u_a(\tilde{L}) = \kappa u_b(0)$. The coupling effect can be used to make sensing devices due to a change in coupling by external inputs. The next subsection will explain the ring resonator that uses the coupling effect to sense external inputs.

2.3.4. Ring resonator

A ring resonator is a device that uses the modulation of light intensity inside a waveguide to measure external effects. The basic design of this device includes a straight waveguide that serves as the input and output for the sensor, which is located next to a circular waveguide (the ring); see Figure 2.14. When light travels through the straight waveguide and reaches the ring, some of the light is coupled to the ring. If the ring is designed correctly, the light will stay within the ring for a full circle before returning back to the straight waveguide and interfering with the incoming light. This interference causes a change in the output light intensity, which is then recorded by a photodiode (PD).

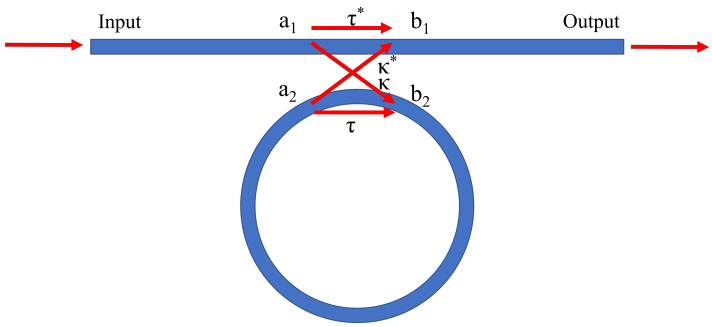

Figure 2.14: Transmission parameters of a ring resonator where a_1, b_1, a_2, and b_2 are the light intensities and τ, τ^*, κ and κ^* are the transmission and coupling coefficients respectively.

Resonances occur when the phase of the light that is coupled to the ring has a phase of $\theta = 2\pi m$ when it returns to the input waveguide, resulting in a dip in the transmission due to destructive interference. This only happens when the circumference of the ring is an integer multiple of the wavelength of the light: $2\pi \cdot r \cdot n_e(\lambda) = m \cdot \lambda$. When an external effect changes the properties of the ring, the resonance wavelength shifts. The highest sensitivity is achieved when the laser is tuned to the flank of the resonance dip, where the most linear behaviour is observed as well [37]. To estimate the output signal and sensitivity of a ring resonator, the mathematical equations that describe the transmission of a ring resonator can be used.

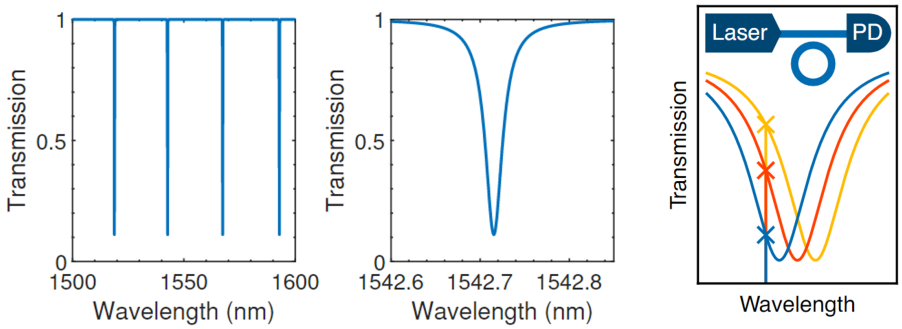

Figure 2.15: Transmission profile of a ring resonator. The left image shows that multiple resonance occur at different wavelengths, the centre image shows a close-up of one resonance and the right image indicates how a shift in resonance results in a different output signal. Taken from Ref. [37].

For a single unidirectional mode the complex mode amplitudes for a lossless coupler without reflections are given by [72]:

$$\begin{pmatrix} b_1 \\ b_2 \end{pmatrix} = \begin{pmatrix} \tau^* & \kappa \\ -\kappa^* & \tau \end{pmatrix} \begin{pmatrix} a_1 \\ a_2 \end{pmatrix} \tag{2.57}$$

where a_1 and b_1 are the normalised complex amplitudes of respectively the input and output of the straight waveguide, a_2 and b_2 are the complex amplitudes of the ring before and after one roundtrip. The squared magnitude correspond to the modal power and additionally $|\tau|^2 + |\kappa|^2 = 1$. For more clarity, see Figure 2.14. After the light has made one roundtrip in the ring waveguide, the light has a phase delay ϕ_r and a round trip amplitude loss described by $a_2 = \alpha e^{j\phi_r} b_2$. The relative power after one roundtrip is defined by α^2 so there is no loss of power when $\alpha^2 = 1$. The complex transmission can by defined as $\tau = |\tau| e^{j\phi_\tau}$ and if we use $\tau\tau^* + \kappa\kappa^* = 1$ and $\theta = \phi_r + \phi_\tau$ the output power $|b_1|^2$ of the straight waveguide is given by [28]:

$$|b_1|^2 = \frac{\alpha^2 + |\tau|^2 - 2\alpha|\tau|\cos(\theta)}{1 + \alpha^2|\tau|^2 - 2\alpha|\tau|\cos(\theta)} |a_1|^2 \tag{2.58}$$

We rewrite the output power in terms of a transmission function:

$$T(\theta, \alpha, \tau) = \frac{\alpha^2 + |\tau|^2 - 2\alpha|\tau|\cos(\theta)}{1 + \alpha^2|\tau|^2 - 2\alpha|\tau|\cos(\theta)} \tag{2.59}$$

This is an important equation because it determines the sensitivity of a ring resonator, which is discussed in section 5.4.

2.4. Discussion

The theory discussed in this chapter does not cover all the required knowledge to be able to fabricate the designed microphone. The fabrication process of the microphone has not been studied in depth. Primarily, the initial stresses in the diaphragm are not studied in detail. As residual stresses are common in SOI wafers, the subject could have been addressed further. Considering time management, it would have been useful to study the fabrication process with more detail rather than acoustics, as the influence of the residual stresses is expected to be more influential than the acoustic impedance on the mechanical sensitivity.

3
Design of a silicon photonic microphone

A silicon photonic microphone uses integrated sensors to convert the acoustic signal to an optical signal. These integrated photonic sensors demonstrate exceptional sensitivity to changes in elongation or refractive index, making them highly suitable for various sensing devices. In this chapter, the design of a silicon photonic microphone is studied. The goal is to understand the different design options that are considered for this thesis. To do so, the chapter starts with an explanation of the fabrication process of an SOI wafer. It includes the fabrication of waveguides and how that has to be considered for the design of the complete microphone. Additionally, post-processing steps are discussed with an explanation of how they relate to the design choices.

These fabrication processes lead to several design options that all have to be considered to come to the optimum design. These are discussed next. With an idea of the fabrication process and what the different options look like, the working principle is explained in detail. The working principle is not discussed first, because I did not want to present the outlook of the microphone without understanding why the microphone has a certain design in the first place.

Then, the lab setup is shortly discussed. As the focus of the microphone is proof of concept rather than improving a current design and its implementation, the design choices are mostly based on the lab setup. Of course, it is kept in mind that without functioning outside a laboratory, the microphone has no potential to solve any of the issues mentioned in the introduction. The differences between a fully integrated microphone and the lab setup are therefore mentioned as well.

The chapter concludes with a short discussion that addresses the most crucial steps in the fabrication and design of the microphone. It also discusses the flaws of the presented design options.

3.1. Silicon Photonic Microphone fabrication

The foundation of this device lies in the use of a Silicon-On-Insulator (SOI) wafer. This section discusses how waveguides are fabricated from an SOI wafer. Furthermore, additional layers can be added to improve the design. These and other post-processing steps are discussed as well. The section ends with a flow chart that illustrates a possible fabrication process of a silicon photonic microphone.

3.1.1. The SOI wafer

An SOI wafer is composed of three distinct layers. There exist different sizes of SOI wafers, this thesis considers the following standard size, for which the top layer thickness is applicable for waveguide design (more on this in subsection 3.1.2) [73, 74]:

1. **(100)-oriented Crystalline Silicon (Si) Layer:** This thin silicon layer, approximately 220$\pm$20 nm thick, serves as the basis for fabricating optical sensing devices. Silicon is chosen due to its excellent optical and mechanical properties.
2. **Thermal Silica (SiO2) Buried Oxide (BOX) Layer:** Positioned between the silicon layer and the silicon substrate, the BOX layer has a thickness of 2 μm. It acts as an insulating layer, allowing optical waveguides to be formed on top of it.
3. **Crystalline Silicon (Si) Substrate:** The silicon substrate is the thickest layer and provides mechanical support for the entire wafer. Its thickness is commonly around 725 μm.

SOI wafers are particularly well-suited for silicon photonics due to several key advantages. Firstly, the optical properties of crystalline silicon are highly desirable for optical devices. Silicon's high refractive index (3.84 [75]) enables strong light confinement in waveguides and optical resonators, leading to reduced signal loss and increased sensitivity. This feature makes silicon photonic microphones highly efficient in converting acoustic signals into optical signals.

Secondly, SOI wafers are compatible with complementary metal-oxide-semiconductor (CMOS) fabrication techniques, which allows for high-precision mass fabrication. Additionally, this compatibility allows for the integration of silicon photonic devices with existing CMOS electronic circuits on the same chip. As a result, silicon photonic microphones can be co-integrated with electronic signal processing circuits, enabling highly integrated and compact systems for advanced signal processing and optical sensing applications.

Furthermore, during the fabrication process of the silicon photonic microphone, the BOX layer serves as an insulating layer during certain processing steps. It allows for precise and controlled etching of the silicon layer to form waveguides and other optical components. Depending on the design, this can be useful to fabricate small sensors. The most common type of waveguides that are fabricated from the SOI wafer are discussed in the next subsection.

3.1.2. SOI waveguide design: STRIP and RIB Waveguides

The top layer of the SOI wafer is used to fabricate the waveguides, see subsection 2.3.1 for a basic understanding of a waveguide. The modifications to the top silicon layer are done with lithography at a foundry specialized in waveguides on SOI wafers. This section introduces two main types of waveguides that can be fabricated on the SOI wafer: strip and rib waveguides. A cross-section of both types is shown in Figure 3.1.

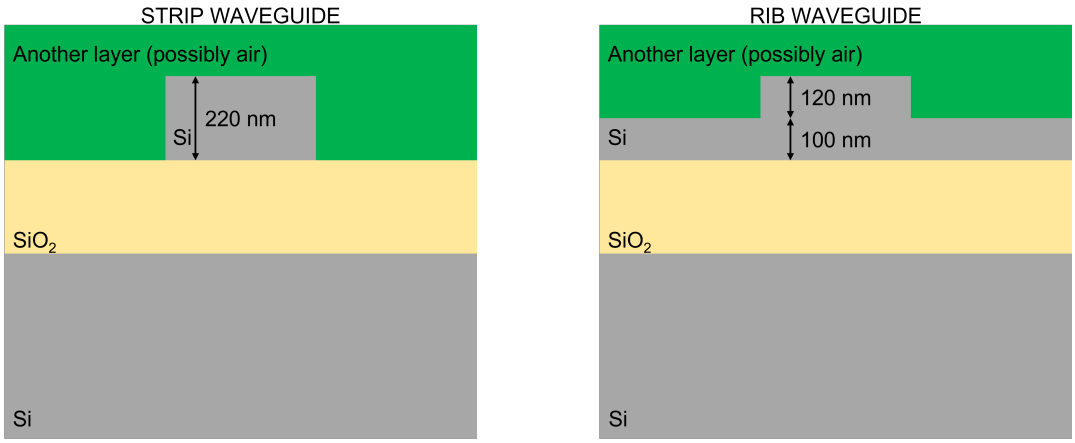

(a) Cross-section of a strip waveguide fabricated from an SOI wafer. The top silicon layer is etched away at the sides of the waveguide, the width is variable.

(b) Cross-section of a rib waveguide fabricated from an SOI wafer. The top silicon layer is partly etched away at the sides of the waveguide. Other thicknesses are accessible, 100 nm is just an example.

Figure 3.1: Schematic figure of STRIP (left) and RIB (right) waveguide.

1. Strip Waveguides: To make a strip waveguide, the silicon layer has to be removed at the edges of the waveguide. Thus, the BOX layer underneath the silicon is required to support the STRIP waveguide. Consequently, the BOX layer should remain to form the diaphragm (the substrate is etched away from the bottom). The buried oxide layer contains compressive stresses and makes it unsuited to form a diaphragm. Previous MEMS microphone literature dealt with initial stresses in the diaphragm by adding corrugated membranes [44, 45]. This fabrication process is complex and should be avoided if possible. Additionally, the thickness of the oxide layer results in large diaphragms with less mechanical sensitivity, discussed later in chapter 5. These reasons make the strip waveguide unsuitable for this thesis and for the silicon photonic microphone, RIB waveguides will be used.

2. Rib Waveguides: Unlike Strip waveguides, RIB waveguides only partially remove the edges of the silicon layer. This allows for the complete removal of the BOX layer underneath, preferred for the diaphragm fabrication. Depending on the etching process, the silicon thickness next to the waveguide

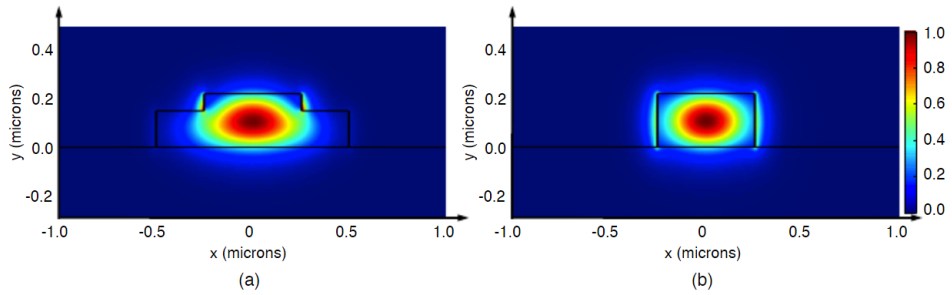

Figure 3.2: Confinement of fundamental mode for RIB (a) and STRIP (b) waveguide, taken from Ref. [76].

can be varied. I considered the foundry Cornerstone as a reference, which offers both 100 nm and 150 nm as silicon thickness [74]. These are considered for the rest of this thesis.

The dimensions of the waveguide determine both the modes that are supported and their corresponding effective index (TE and TM modes are discussed in subsection 2.3.2). In Figure 3.3, the effect of waveguide dimensions of a STRIP waveguide on the guided modes and corresponding effective index is shown [28]. The height of 220 nm ensures that only the first TE mode is supported, which is desired for effectively sensing the output signal.

To give an indication of what the modes look like in terms of intensity amplitude, Figure 3.2 is taken from Ref. [76]. The width is 500 nm and the height is 220 nm. For the RIB waveguide, the silicon thickness is etched to 150 nm around the waveguide. In this example, the silicon is etched away completely at a total width of 1 μm, but this is unnecessary for proper confinement of the mode [28], figure 5.3b.

The waveguide that is considered for this thesis is a strip waveguide with a width of 450 nm and a silicon thickness next to it of either 100 nm or 150 nm. This will ensure that only one mode is guided. The buried oxide will be removed from the bottom to form a diaphragm. This step and other post-processing steps are discussed in the next section.

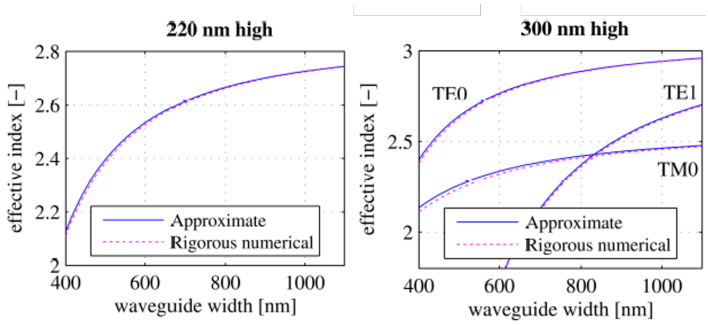

Figure 3.3: Effect of waveguide width for a STRIP waveguide on the effective index, for 220 nm and 300 nm height. Increasing the height results in an increased amount of supported modes; taken from Ref. [28], Chapter 2.4.3.

3.1.3. Diaphragm fabrication: post-processing

The previous steps are required to design the photonic circuit of the microphone. Several steps are necessary to create the diaphragm and complete the microphone after the waveguide fabrication. These are:

- Bottom etching of silicon substrate and BOX layer.
- Layer deposition on top of the top silicon layer.

Bottom etch

The bottom etching of the silicon substrate and BOX layer leaves a floating silicon top layer and determines the dimensions of the diaphragm. This step is also mentioned in the manufacturing of a

capacitive MEMS microphone as DRIE, see subsection 2.1.2. The alignment of the edge determines where the sensor is located on the diaphragm. For example, if the ring resonator is designed to have the centre of the ring exactly in the middle of a circular diaphragm, then the bottom etch determines where exactly the ring ends up on the diaphragm. This requires proper alignment of the mask that is used for the bottom etch process. Current microphone

Additional layer deposition

It is possible to add an additional layer on top of the silicon layer. The additional layer has a different refractive index and changes the optical properties of the waveguide. In any case, the deposited layer should have a refractive index lower than silicon. In practice, it should be as low as possible to ensure strong confinement of the light. Optically, the layer is not essential as the device would also work well with air surrounding the waveguide. Mechanically, the advantages are more significant. It adds design freedom to the size of the diaphragm. With a resonance frequency of around 25 kHz, the silicon thickness fully determines the size of the diaphragm. Diaphragms without a layer and resonance near 25 kHz are small (radius of approx 100 μm) and more sensitive to fabrication errors. Furthermore, the device is more vulnerable to collapsing without any layer deposition, for example when high pressures are applied.

3.2. Design options

This section discusses the different design options that are considered in this thesis. Different optical sensing methods have been discussed previously in section 2.3. An MZI was applied before to fabricate a silicon photonic microphone by Imec [33]. A ring resonator was applied before on an OMUT, to sense ultrasound. This thesis considers a ring resonator as the optical sensor. It would be interesting to do a broader study to which method is more suited for a microphone. Both can be applied and a more extensive study is required to determine the best option.

The diaphragm considered in this thesis has a circular shape. The circular shape of the diaphragm allows for uniform distribution of stress, and it avoids sharp edges, which reduces the risk of mechanical failure. Furthermore, the first eigenmode deflection shape is symmetric which allows for a better response to nonuniform sound waves. In general, the symmetric shape of a circular diaphragm offers structural benefits. Current MEMS microphones apply circular diaphragms as well [8], which substantiates the argument for using a circular shape.

With both the diaphragm shape and optic sensor chosen, there are still different options for the silicon top layer thickness, the layer material and thickness, the size of the diaphragm and the size of the ring resonator. These options are specified in the next subsections.

3.2.1. Silicon thickness

The top silicon layer of the SOI wafer can be etched to several thicknesses. The thicknesses of the silicon layer considered in this thesis are 100 nm, 150 nm and 220 nm. The thickness of 220 nm requires extra attention. It is important that next to the waveguides the silicon is partly etched away because otherwise, the modes will not be confined and the light is not guided. Because these parts etched away next to the waveguides are in reality small compared to the radius of the diaphragm, it can be considered as a layer of 220 nm silicon. A cross-section of these three options is shown in Figure 3.4. For the 220 nm option (3) in the figure, it is also possible to etch the parts next to the waveguide to 100 nm instead of 150 nm. Similarly, for the 100 nm (1) and 150 nm (2) options, the thickness next to the waveguide could be 150 nm and 100 nm respectively. The choice depends on the effective index of the guided mode, which is studied later in chapter 6.

3.2.2. Diaphragm radius

The diaphragm radius is solely determined by the bottom etch where the silicon substrate and BOX layer are removed. The diaphragm radius should at least be larger than the radius of the ring and should allow air pressure to enter. For clarity reasons, a schematic overview that indicates the radius of the diaphragm is shown in Figure 3.5. The figure is not on scale and is only meant to illustrate the fact that the diaphragm is circular, and to understand which parts are making up the whole mechanic structure of the microphone.

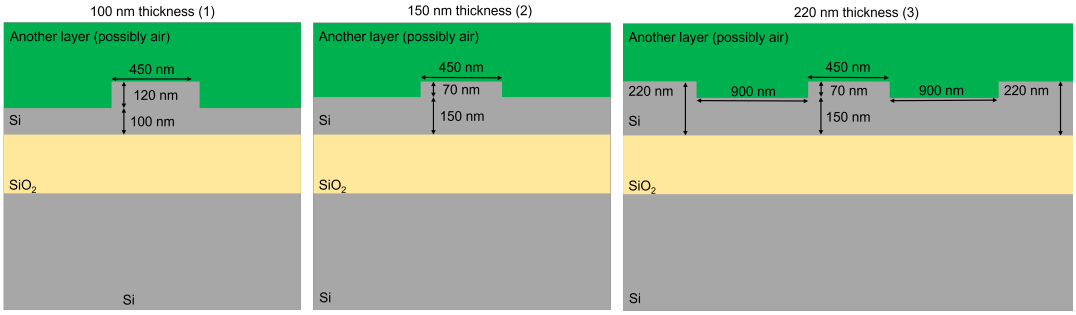

Figure 3.4: Cross-section of the different options for the silicon top layer thickness considered for this thesis. The figure illustrates the dimensions of a RIB waveguide for different thicknesses of silicon.

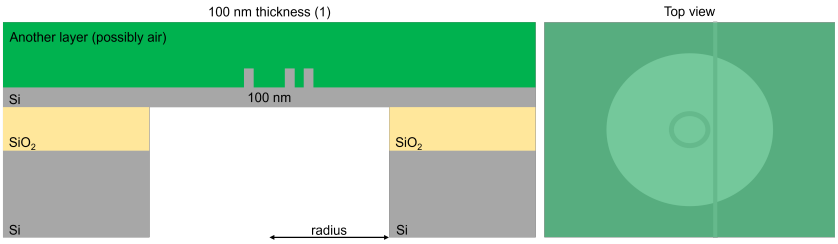

Figure 3.5: Indication of the diaphragm radius, which is determined by the bottom etch. The figure shows an example of 100 nm silicon thickness; the other thicknesses mentioned in subsection 3.2.1 are possible too.

3.2.3. Layer deposition

The additional layer that can be deposited on the top silicon layer changes the optical and mechanical properties of the microphone. The material properties that are considered for this thesis are:

- Young's modules (mechanical)
- Poisson's ratio (mechanical)
- Density (mechanical)
- Refractive index (optical)
- Effective index (optical)

The materials considered in this thesis are:

- Silicon Dioxide (SiO_2)
- Silicon Nitride (Si_3N_4)
- Silicon Carbide (SiC)
- PDMS

The layer thickness is considered as a minimum of 150 nm to ensure that the layer covers the waveguides properly. In terms of numerical simulations, the thickness is considered in steps of 5 nm. When fabricating the final design, the fabrication error should be considered including the influence on the final design.

The next section explains the working principle of the considered design options, just for clarification. The working principle is the start of the next chapters where the modelling of the microphone is done.

3.3. Working principle

The working principle of a silicon photonic microphone is schematically shown in Figure 3.6. A laser sends light into the straight waveguide with a wavelength of around 1550 nm. The waveguide is placed so close to a circular waveguide (the ring) that the light in the straight waveguide couples to the ring and makes a roundtrip inside the ring before it couples back to the straight waveguide. At specific optical

resonance wavelengths, the light destructively interferes with the input waveguide and dips in the light intensity occur at the output. These wavelengths are defined by [36]:

$$m\,\lambda_m = n_e\,l \tag{3.1}$$

where m is an integer, n_e the effective index and l the circumference of the ring. The circular diaphragm (cross-sections on the left) is deformed by incoming sound waves. The small squares represent the ring of the ring resonator, and the deflection changes the optical resonance wavelength of the ring. Because the wavelength of the input laser (measuring wavelength) is constant, the intensity of the light at the outport changes. The light intensity in the outport is measured with a photodiode. As indicated by the figure, the upward motion (black) elongates the ring and increases the resonance wavelength because the circumference l in Equation 3.1 is increased. The photodiode should be chosen such that without deflection (orange), the normalized output voltage is equal to 0.5.

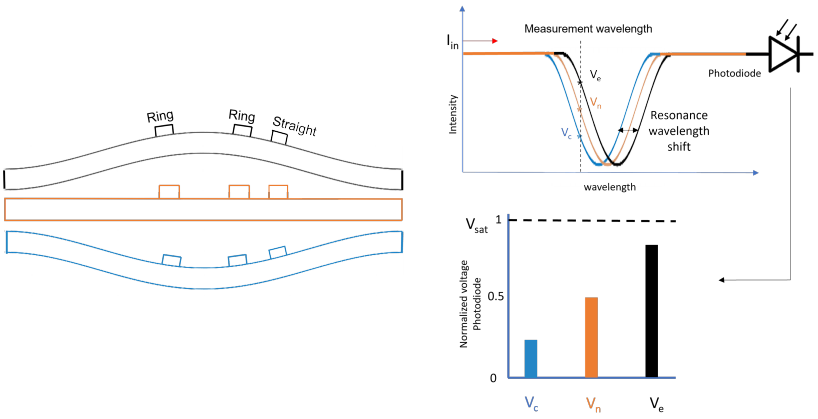

Figure 3.6: Schematic explanation of the working principle of a silicon photonic microphone that uses a ring resonator on a circular diaphragm

3.4. Lab setup

The lab setup plays an important role in this project. The goal of this section is to explain how design options are influenced by the consideration of the lab setup. For the lab setup, it is not required to fabricate a fully integrated device to test the photonic sensor. To understand the differences, the setup is explained first, followed by briefly marking the differences with a fully integrated microphone.

3.4.1. Lab setup components

A simplified schematic overview of the lab setup is shown in Figure 3.7. A tunable laser sends polarized light of 1550 nm towards the photonic chip using an optical fibre cable. The incident angle ensures coupling with a grating coupler. The light passes through the waveguide and ring resonator, over the diaphragm. Then the light is coupled by another grating coupler, towards the photodetector. The optical signal is modulated by the sound pressure, as explained in section 3.3.

3.4.2. Further considerations for on-chip integration

Ideally, the photonic microphone can be packaged as a single fully integrated device. The most important differences between the lab setup and a fully integrated microphone are listed below.

- The lab setup uses high-end laboratory devices for the photodetector and laser that are too large to integrate on the chip.
- The lab setup does not require a protective case.
- The lab setup does not require a ventilation hole.

Laboratory devices: The quality of the devices is not comparable with a fully integrated chip, as these will suffer from size limitations. However, the integration of both the laser and photodetector is not so

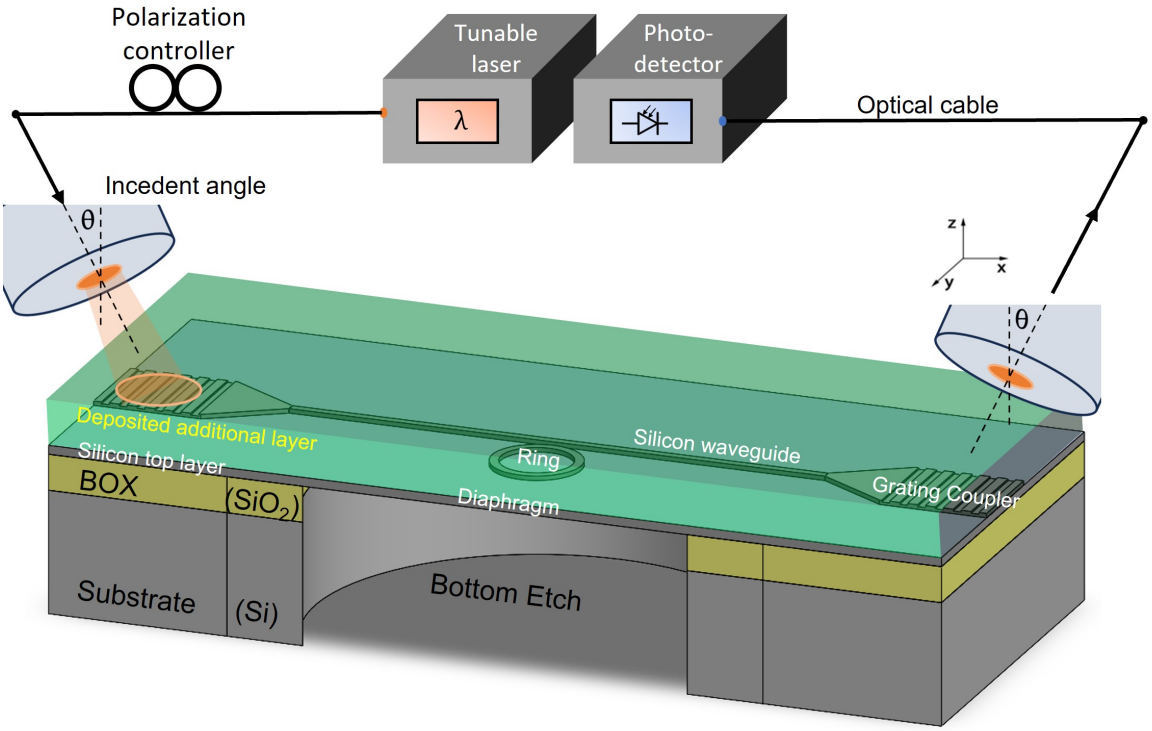

Figure 3.7: Simplified schematic overview of lab setup (cross-section). A tunable laser sends polarized light towards the photonic chip using an optical fibre cable. The incident angle ensures coupling with a grating coupler. The light passes through the waveguide and ring resonator, over the diaphragm. Then the light is coupled by another grating coupler, towards the photodetector.

much effecting the mechanical part of the sensor and is therefore not considered in the design process.

Protective case: MEMS microphones require a protective case to protect it against its surroundings and against electromagnetic interference [10]. Furthermore, the package ensures that the backside of the diaphragm is acoustically separated from the front side. The small volume of the case is causing extra acoustic noise [12]. The lab setup will not include a protective case, so there is a slight unrealistic advantage of the microphone in the lab setup. The choice has been made not to consider a back volume due to the protective case, because the protective case is not the dominant issue for current microphones. Furthermore, it is unknown what exactly is required to protect the fully integrated photonic microphone.

Ventilation hole: MEMS microphones include a ventilation hole to equalize the ambient pressure with the pressure inside the microphone back volume [67]. This is done, for example, to prevent the microphone from collapsing in the elevator of a New York skyscraper. The ability to detect low frequencies reduces due to this opening. Additionally, it adds flow resistance, which contributes to the noise. The lab setup will require acoustic separation between both sides of the microphone, however these pressures can easily be equalized before the measurement without a ventilation hole. The choice has been made not to include a ventilation hole, because it is not the dominant issue for current MEMS microphones.

3.4.3. Chip attachment

The chip that is fabricated from the SOI wafer is glued on a PCB. Also, for the lab setup the chip needs to be glued to a substrate for easy handling. The PCB hole in ref. [9] is smaller than the diaphragm radius, however, this is acoustically disadvantageous. The smaller port radius also results in a Helmholtz resonance, see subsection 2.2.7. The reason for a smaller hole radius could be that it enables better protection from the outside, or that the attachment between the PCB and chip requires enough surface

area. The difference between a larger and smaller hole radius of the PCB is schematically shown in Figure 3.8. For this thesis, the PCB is assumed to have a larger hole radius than the diaphragm. The figure also indicates how a microphone can be placed next to the chip to measure the pressure close to the microphone. The measurement microphone ensures that the correct input signal is used for the characterization of the device.

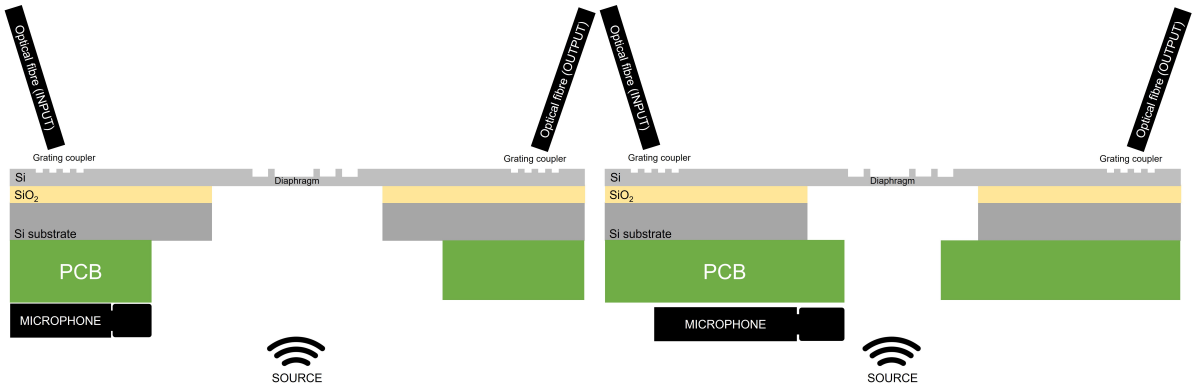

(a) Cross-section of a lab setup where the chip is mounted on a PCB with a larger hole radius than the diaphragm radius.

(b) Cross-section of a lab setup where the chip is mounted on a PCB with a smaller hole radius than the diaphragm radius.

Figure 3.8: Clarification of hole size options of the PCB to which the chip is attached

3.5. Discussion

This section discusses the most crucial design considerations that have not been considered in this thesis. These include both mechanical and optical design options.

3.5.1. Mechanical design

Post-processing

One of the most crucial aspects of mechanical design regards the post-processing stage. First of all, layer deposition comes with many challenges. The deposition of an additional layer introduces inherent stress within the material, which can affect the microphone's mechanical stiffness and operational characteristics. These stresses should be studied, including an analysis of how they influence mechanical stiffness.

Furthermore, the material properties of the layer that is deposited are not exactly known. Young's modulus, density and Poisson's ratio should be tested to correctly predict the microphone's behaviour. How the fabrication process of the additional layer changes the material properties is essential to study as well.

The deposition should be performed with much care for the silicon layer on which the layer is added. The silicon layer is extremely thin, and any damage on the waveguide or on the diaphragm could lead to signal losses or other types of malfunctioning.

Achieving precise alignment between the bottom etch and the fabricated waveguides is critical for the successful operation of the silicon photonic microphone. A specific example is the alignment of a ring with the center of the diaphragm, which directly relies on the accuracy of the bottom etch alignment. Any deviation in alignment could adversely affect the microphone's performance.

Additionally, the radius of the diaphragm is determined by the bottom etch. A significant amount of the mechanical properties of the diaphragm is attributed to the radius, making it sensitive to fabrication errors. Hence, special attention to the bottom etch is essential to ensure optimal mechanical performance.

All these challenges require an individual approach and careful study is essential to realise a properly functioning device. These specific post-processing difficulties are left out of this thesis for time consideration.

Shape of the diaphragm

Another point of attention lies in the shape of the diaphragm. For simplicity reasons, the shape is taken as a circular diaphragm, commonly found in microphones. In terms of design freedom, this makes the design easier, and now only the thickness and layer of the material determine the diaphragm design. Furthermore, circular shapes can be easily modelled in FEM software due to the axisymmetry. There are several good reasons to use a circular diaphragm, but since the sensing mechanism is different from a capacitive microphone, it would be interesting to study different shapes with an optical sensor in mind.

3.5.2. Optical design

It has already been mentioned that the microphone's optical design is incomplete since it relies on an external laser and photodetector. Another point of discussion lies within the optical sensor itself. The choice has been made to use a ring resonator as a sensing mechanism. Ring resonators are generally very sensitive to changes in optical path length or refractive index. However, they are sensitive to wavelength noise and require precise tuning of the wavelength to the flank of the resonance dip. It would be interesting to quantify the differences regarding sensitivity and robustness for both a ring resonator and MZI.

4
Model thermo-acoustic noise

Thermo-acoustic noise is the dominant type of noise in current state-of-the-art MEMS microphones, as discussed in Figure 1.1.2. To understand the role of thermo-acoustic noise for a silicon photonic microphone, the acoustics of a silicon photonic microphone have been studied. This chapter focuses mostly on the models that were used and shortly repeats equations that have been derived in section 2.2. It starts with an explanation of acoustic lumped-element modelling, with a follow-up on how this is used to quantify thermo-acoustic noise of a microphone. The results of two different papers that report their acoustic noise models have been reproduced to verify that my modelling is correct. Lastly, the model that is used to find the acoustic noise of the silicon photonic microphone is presented.

4.1. Acoustic circuit modelling

To model thermo-acoustic noise, (lumped element) circuit modelling is used. Acoustic systems are simplified to discrete electrical circuits, where the electrical elements correspond to their acoustic counterparts. It is essential to understand the relationship between electrical components and their acoustic equivalents. In circuit modelling, voltage is analogous to acoustic pressure, while current corresponds to volume flow [53]. The acoustic equivalents of basic electrical components are discussed below.

Acoustic mass: The acoustic mass is associated with the mass of air accelerated without compressing it. The mass is modelled as if it moves through a constant surface area. The volume flow U can then be expressed as velocity u times the surface area S and pressure as the force per surface area S. As a result, the acoustic mass m_a is the mass m divided by the surface area squared, and the unit is kg/m^4 [55]:

$$f = m\frac{du}{dt} \rightarrow \frac{f}{S} = p = \frac{m}{S^2}\frac{d(uS)}{dt} = m_a\frac{dU}{dt} \tag{4.1}$$

The acoustic mass is represented as an inductor, with corresponding impedance $Z_L = j\omega L$ with $L = m_a$. It is possible to convert the mechanical mass of the diaphragm towards acoustical mass by dividing it by the surface area squared and add it to the acoustic model.

Acoustic compliance: Acoustic compliance can be considered as the spring-like behaviour of a compressible volume. The compression of a volume of air by a certain pressure p is given as [55]:

$$\frac{f}{S} = p = \frac{1}{C_m S^2}\int U dt \tag{4.2}$$

with C_m the mechanical compliance. The acoustic compliance is equal to $C_a = C_m S^2$ with unit m^5/N. For a certain volume V the acoustic compliance is approximated as [55]:

$$C_a = \frac{V}{\gamma P_{atm}} \tag{4.3}$$

with γ the dimensionless ratio of specific heats. The acoustic compliance is modelled as a capacitor, with corresponding impedance $Z_C = 1/(j\omega C)$, with $C = C_a$. It is possible to convert the mechanical compliance of the diaphragm to acoustical compliance by multiplication of the surface area S squared.

Acoustic resistance: Acoustic resistance is the mechanical equivalent of a damper and represents a dissipation mechanism. In acoustics, dissipation commonly occurs with the viscous property of air

[55]. For example, the viscous flow between the perforation holes in the backplate act as a mechanical damper, and has a certain acoustic resistance. The force of a mechanical damper is $f = R_m\, u$, and is related to the acoustic resistance as $R_a = R_m/S^2$, which has unit Ns/m^5. The impedance is simply equal to $Z_a = R_a$ without frequency-dependent behaviour.

With an idea of the components used in circuit modelling, the acoustics for a MEMS microphone can be discussed. In this section, it is explained how circuit modelling is used to derive the thermal acoustic noise.

4.2. Thermo-acoustic noise of a MEMS microphone

This section applies the general theory of acoustics that has been discussed so far to the application of a MEMS microphone. The aim of this section is to understand how thermo-acoustic noise is modelled for a MEMS microphone and verify how these models can be implemented. First, the theory of modelling acoustic thermal noise is presented. Second, the results of the acoustic noise models of two published papers (Ref. [9, 16]) are reproduced to verify the implementation.

4.2.1. How to model thermal acoustic noise

To calculate thermo-acoustic noise, the fluctuation-dissipation theorem (FDT) is used. It states that for each source of dissipation (absorption of energy, e.g. friction), there is a reaction as thermal fluctuation (kinetic energy) [61]. In the context of thermo-acoustic noise, it means that the drag experienced by any airflow dissipates the kinetic energy of the air into heat. According to the FDT this heat results in the random motion of air particles (known as Brownian motion). These random motions cause small fluctuations in the gas density, resulting in pressure fluctuations, measured as noise. To quantify the magnitude of the thermo-acoustic noise, the sources of dissipation must be analysed [12, 43, 62]. Each individual source of dissipation can be added to find the total noise magnitude [9].

Each individual noise source is calculated as Johnson-Nyquist noise, which describes the relation between noise (fluctuation) amplitude, temperature and resistance. Although Johnson-Nyquist noise is commonly encountered in electronics, thermo-acoustic pressure can be calculated similarly [61]. The root mean square (RMS) of the pressure noise P_{noise} and volume flow noise Q_{noise} (equivalent to Johnson-Nyquist noise of voltage and current) is equal to [62] [16]:

$$P_{noise} = \sqrt{4kT\Delta f R_a} \tag{4.4a}$$

$$Q_{noise} = \sqrt{\frac{4kT\Delta f}{R_a}} \tag{4.4b}$$

with $k = 1.38 \cdot 10^{-23}$ Bolzmann's constant, T the temperature in Kelvin, Δf the specified bandwidth (for which the noise spectral density is constant) and R_a the acoustic flow resistance. If the noise power is frequency-dependent, the bandwidth is specified as 1 for each evaluated frequency. Note that for acoustic impedances with a real and imaginary part, the real part is considered as flow resistance [12].

The implementation of the aforementioned theory is confirmed through the replication of results from two distinct papers, which will be elaborated upon in the subsequent subsections.

4.2.2. Verification: replication of standard acoustic noise model

The first paper that has been reproduced is authored by Kim and Lee [16]. Primarily, this paper clearly presents their electric circuits complemented by a table providing exact values for each element; see Figure 4.1a and Figure 4.1b. Therefore, it is accessible for replication of the results. The output of the circuits is the noise spectral density of three components: the sound port resistance, air flow leakage through the diaphragm (ventilation hole) and the backplate noise (the resistance of perforations and compression between plates); shown in Figure 4.1c. These noise types have been discussed in detail in subsection 2.2.9.

The replication of the results requires software to simulate electronic circuits. I used Simulink in combination with the RF Blockset library to analyse the circuit. It can model frequency-dependent impedances, allows for a specification of the analysed frequencies, and it is easily integrated with MATLAB.

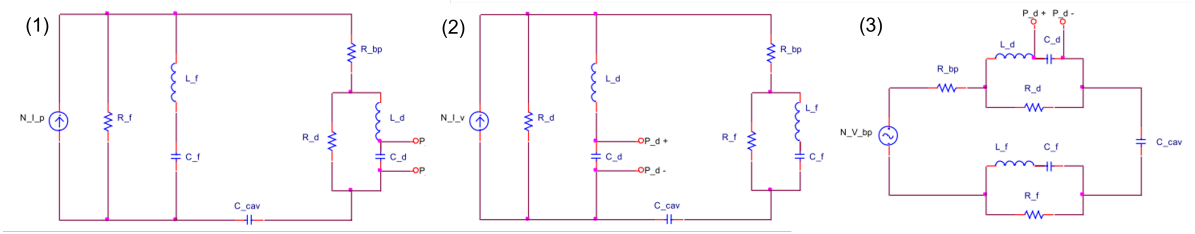

(a) The electronic circuits that have been used by Kim and Lee to model noise corresponding to the port resistance (1), diaphragm leakage (2) and the backplate (3).

Sources	Lumped elements	Quantity
Packing (Sound port, r = 300um, l= 400 um, cavity volume = 4.64e-9 m^3)	L_f (kg/m^4)	1.701e3
	C_f (m^5/N)	3.142e-15
	R_f ($N.s/m^5$)	2.289e6
Back plate (Hole radius = 6 um, gab distance = 4 um)	R_tb ($N.s/m^5$)	4.191e8
	C_tb (m^5/N)	7.554e-18
Diaphragm Thickness =1.2 um	L_d (kg/m^4)	1.435e4
	C_d (m^5/N)	2.429e-15
	R_d ($N.s/m^5$)	1.820e12
Back cavity (vol= 3.02e-10 m^3)	C_cav	2.043e-15
Electrical capacitance	C_e (F)	3.802e-13
Turns ratio (with Vbias= 10volts)	N (volt/Pa)	2.65e-2

(b) The values that correspond to each individual electric component.

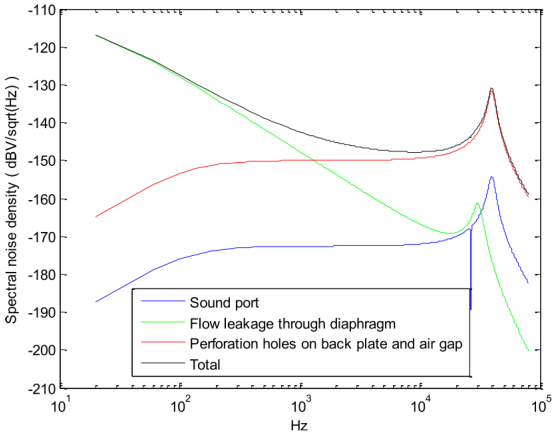

(c) The noise spectral density which results from the electric circuits.

Figure 4.1: (a) The electronic circuits that have been used by Kim and Lee, (b) the corresponding values of the circuit components, (c) the resulting noise spectral density. All taken from Ref. [16].

The circuits that I replicated are shown in Figure 4.2. Each individual noise source requires either a voltage source in series or a current source in parallel with the corresponding acoustic resistance. The value of the voltage or current source is calculated with Equation 4.4. The voltage over the capacitor that represents the diaphragm is used as the output. The outcome of my model is shown in Figure 4.3a.

Model A has two models; one of those uses a current source, and the other uses a voltage source. Additionally, one circuit uses a transducer with a transduction ratio of N (Volt/Pa), and the other uses MATLAB to multiply the outcome by N to convert pressure to volts. The transducer has been added to verify if the outcome would be the same with a transducer, which is discussed in the paper. These two models are expected to give identical results and are added for additional verification. As expected, the results of both models are equal.

The result in dashed lines with a transparent overlay of the results presented in the original paper is shown in Figure 4.3b. The results can now be easily compared.

The outcome of my copy has the same magnitude for the sound port and backplate, but a slightly higher magnitude for the ventilation hole. Furthermore, the low-frequency roll-off of the Kim model starts earlier. Lastly, the resonance of the flow leakage through the diaphragm is slightly different from the results by Kim. Double-checking everything and making adjustments did not fix these issues, so a few reasons that could be of influence are listed. Simulink has a limit of 10^{-18}, which is very close to the value of 7.554e-18 of the backplate capacitor. On their side, the graph looks of poor quality, with perhaps indicates a limited amount of evaluation points. Especially at low frequencies, the limited evaluation points are visible. Linearly spacing of the frequency vector results in fewer points on the lower spectrum of the frequency axis due to the logarithmic scaling of the figure.

Nevertheless, the copy matches the amplitude well, including the correct resonance and it gives enough insight into how acoustic noise can be modelled to continue to the next model by Knowles, which is discussed in the next subsection.

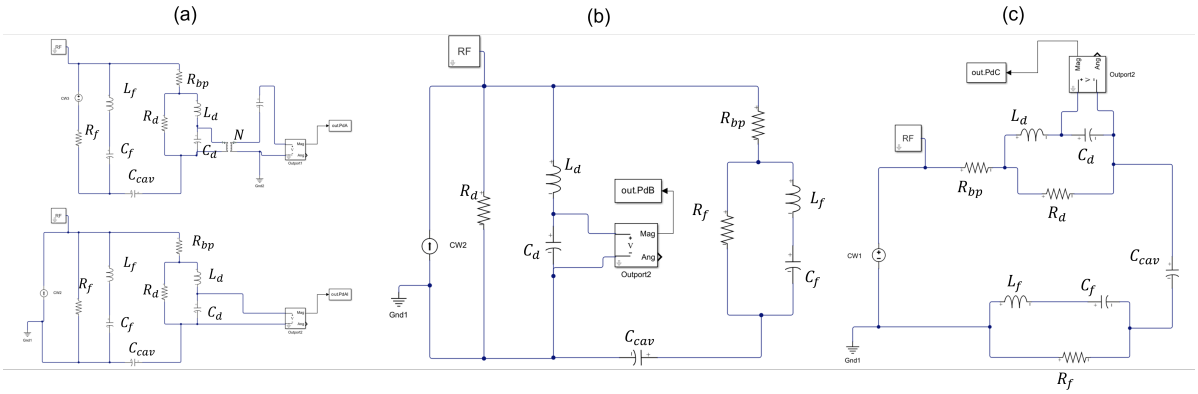

Figure 4.2: Snapshot of Simulink models that were used to copy the result of Kim and Lee [16]. A has two models to compare the outcome of a current and voltage noise source (equal outcome as expected).

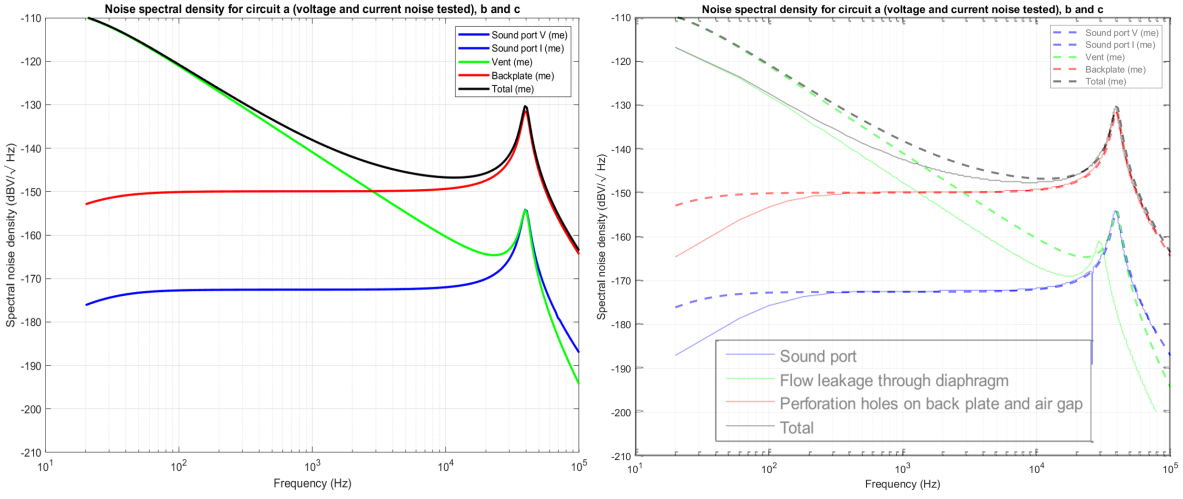

(a) Result of the replication using the Simulink output for all three circuits.

(b) My result in dashes with a transparent overlay of the result presented by Kim and Lee [16] for comparison.

Figure 4.3: The result of the NSD replica of Ref. [16], together with a transparent copy to easily compare the results.

4.2.3. Verification: replication of Knowles acoustic noise model

The second result that was reproduced is the model presented by Knowles in ref. [9]. This replica is added because the model includes equations rather than just the numerical values. Additionally, the model is more sophisticated compared to the model of Kim and Lee. Even more so, the paper is considered state-of-the-art of current MEMS microphones. Unfortunately, not all parameters were given, and the model is abstractly presented. The model that is presented in the paper is shown in Figure 4.4. The individual noise sources have been previously discussed in chapter 2, subsection 2.2.9.

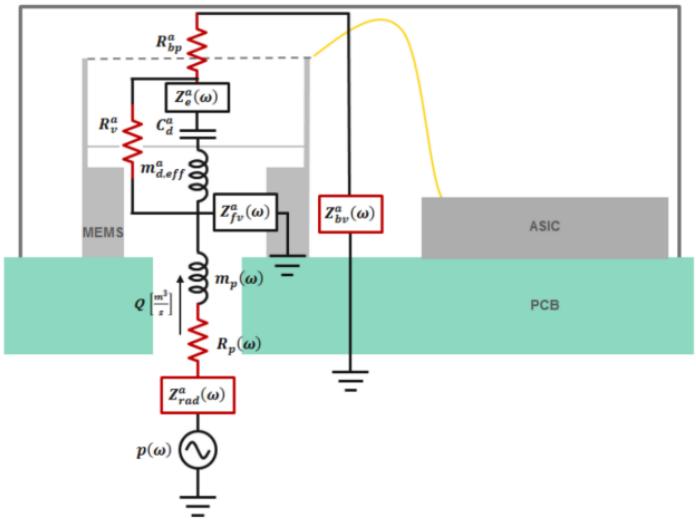

Figure 4.4: Knowles lumped element model used to derive the acoustic noise levels; taken from Ref. [9].

To quantify the acoustic thermal noise for each individual acoustic impedance, a voltage source is added in series with the resistor. The value of the voltage is given by Equation 4.4a. For impedances with both real and imaginary parts, only the real part is considered as R_a [12]. Knowles only showed the five largest contributors to the noise diaphragm, and as a result, I have five circuits to analyse each noise source, similar to the model by Kim. Each model is shown in Figure 4.5; only the last model indicates the names of the elements for simplicity reasons. These are equal for all models.

The result is shown in Figure 4.6, where on the right image, my result is transparently placed over the result from the paper. My result has a higher value for the back volume, backplate, vent hole and port + radiation. The best match is for the front volume. For the backplate simulation, the vent resistor has been removed and as a result, the low-frequency roll-off does not occur. Additionally, the value for the port and radiation impedance is different. Differences can be explained because not all values are numerically given. Also, the paper by Kunztman et al. from 2018 (Ref. [12]) reported a very similar acoustic noise analysis, with slightly different equations and values. Perhaps some equations from this paper were used. Lastly, the back volume impedance was obtained numerically and is not specified in the paper. Consequently, it is not possible to make a perfect copy of the results that were published.

The paper also shows a pie chart in which the total noise power for each source is shown. This result has also been copied to compare if the magnitudes are proportionally matched. The result is shown in Figure 4.7.

To calculate the total A-weighted RMS noise power V_{rms}, the square root of the noise spectral density squared integrated over the bandwidth is taken. This results in the noise power as a root mean square voltage. The equation for the integration is as follows:

$$V_{rms} = \sqrt{\int_{f1}^{f2} NSD^2(f)df} \tag{4.5}$$

with $f1$ and $f2$ the lowest and highest value of the specified frequency range. For numerical integration, which is done for this thesis, the equation is written as:

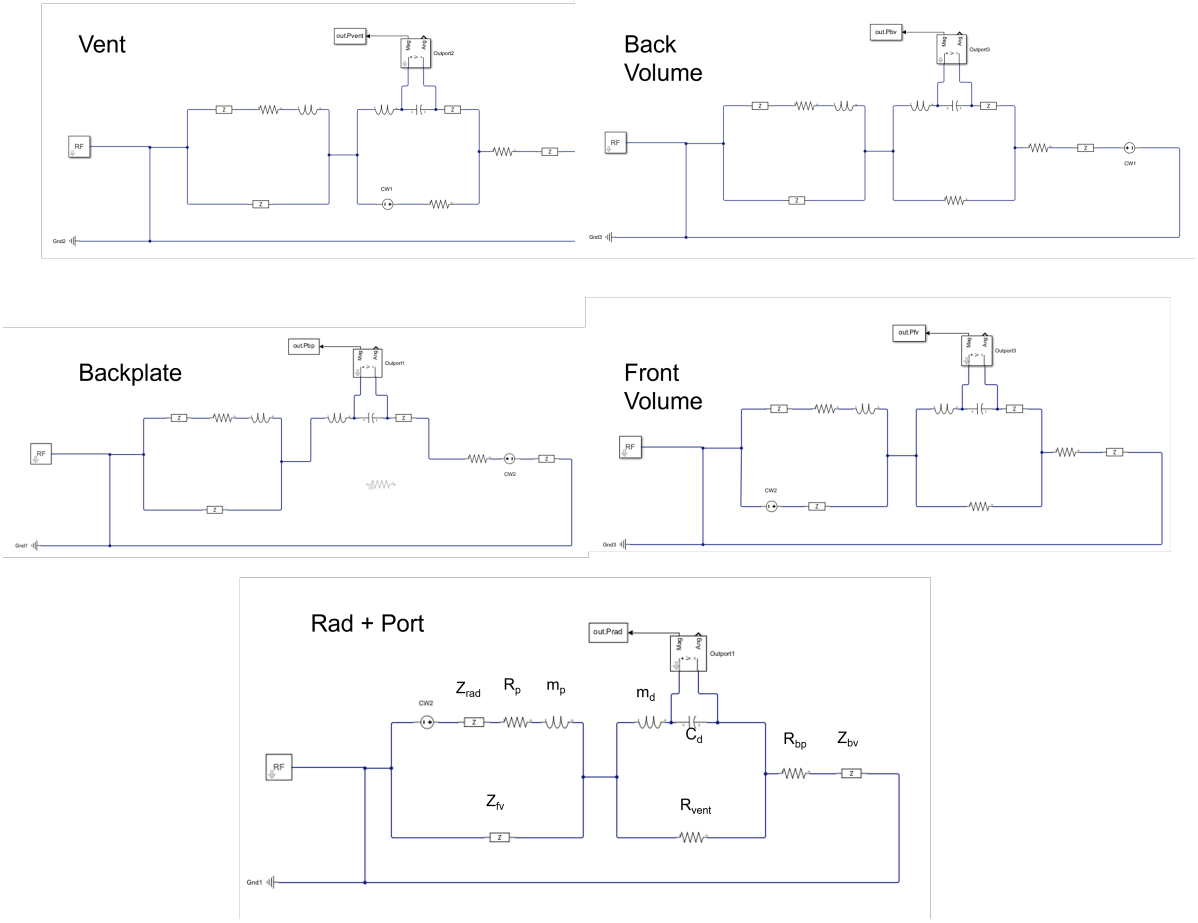

Figure 4.5: Simulink models that were used to copy the result from Ref. [9]. The electrical components of all models are equal to the indications of the Rad + Port model.

$$V_{rms} = \sqrt{\left(\sum_{i=1}^{n} NSD(i)^2 \Delta f\right)} \tag{4.6}$$

where Δf represents the difference between consecutive frequency points for a linearly spaced frequency vector; NSD_A is a vector with the A-weighted NSD corresponding to the frequency vector, obtained from the Simulink model that is shown in Figure 4.5. To account for the boundary effects, the first (i = 1) and last (i = n) are multiplied by 0.5. The A-weighting filter accounts for the hearing that is perceived by humans, and is given in dB by [77]:

$$R_a(f) = \frac{12194^2 f^4}{(f^2 + 20.6^2)\sqrt{(f^2 + 107.7^2)(f^2 + 737.9^2)}(f^2 + 12194^2)} \tag{4.7a}$$

$$A(f) = 20 \log_{10}(R_a(f)) + 2 \tag{4.7b}$$

The resulting amplification is shown in Figure 4.8. It can be seen that both low and high frequencies drop off quickly and frequencies between 1 and 8 kHz (speech frequencies) are slightly amplified. The low-frequency drop explains why the backplate is the largest contributor to the noise power instead of the ventilation hole. Also, the logarithmic scaling is misleading in terms of noise power, since high frequencies account for a larger bandwidth.

All the equations and values that have been used to come to the result of my copy are shown in Table 4.1 and Table 4.2. The replicas are not perfectly identical. The exact reason why the result is not identical depends on the noise source. One reason is that simply not all values are given. Since the

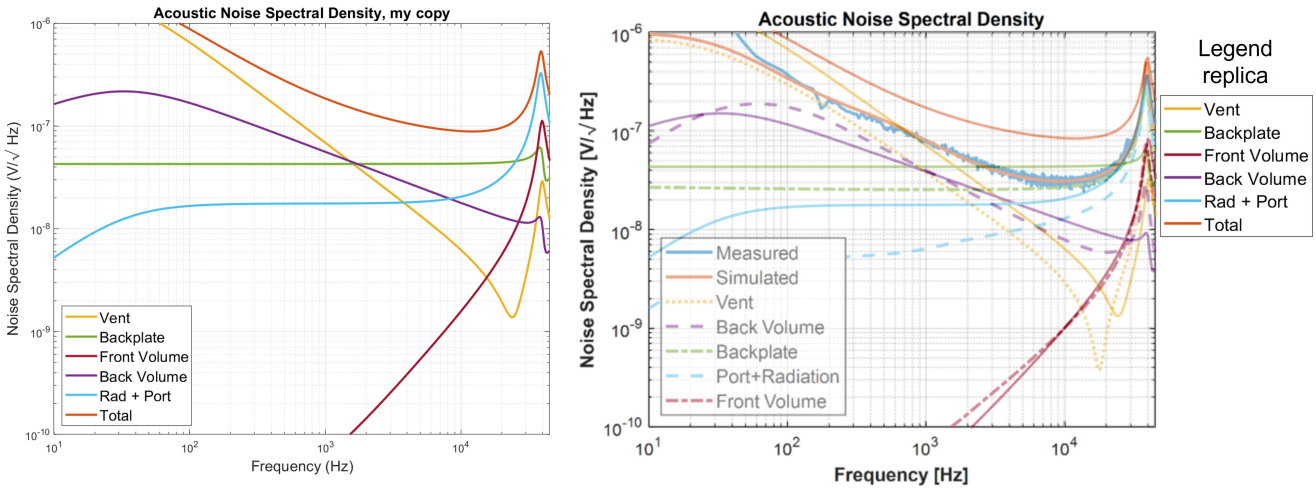

Figure 4.6: The result of the NSD replica of Ref. [9], together with a transparent copy to easily compare the results.

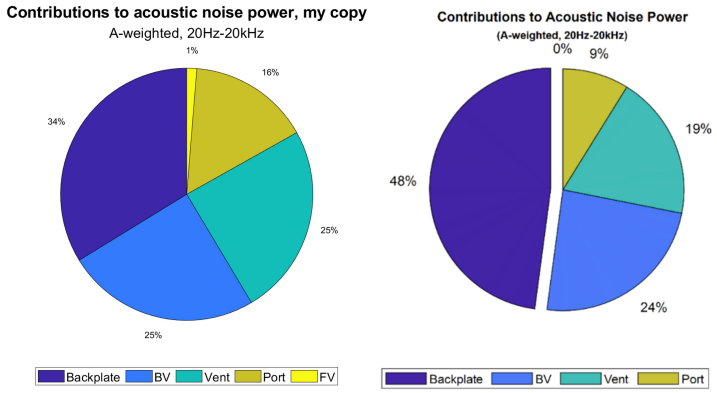

Figure 4.7: Pie chart by Knowles [9] (right) to indicate the contributions of each individual source to the total noise power between 20 and 20000 Hz, with an A-weighting filter applied together with my copy (left).

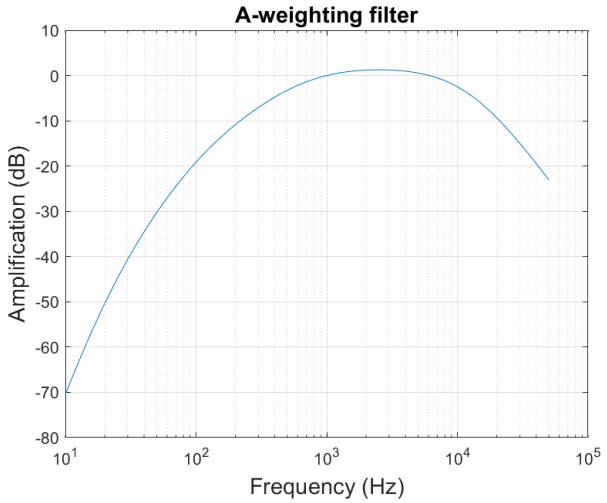

Figure 4.8: Amplification factor of the A-weighting filter plotted against frequency.

NSD measured at the diaphragm depends on all the values of the circuit, it is difficult to know exactly where the mistake is. However, the overall shape and magnitudes of the noise sources are considered

to be within an acceptable limit. With all the attempts to match the result, I have a good feeling about how the noise model works and I am confident enough to continue with my own model and simulate the acoustic noise for an integrated photonic microphone.

Element	Description	Formula	Value
Z_{rad}	Radiation impedance	$\boldsymbol{Z}_{rad} = \frac{\rho_0 c}{\pi a_p^2}\left[1 - \frac{J_1(2ka_p)}{ka_p} + j\frac{H_1(2ka_p)}{ka_p}\right]$ [9]	Frequency-dependent
R_p	Port resistance	$R_p = \frac{8\eta l_p}{\pi a_p^4}$ [9]	1.24e7 (Ns/m^5)
m_p	Port mass	$m_p = \frac{4\rho_0\, l_p}{3\pi a_p^2}$ [12]	4.19e3
Z_{fv}	Front volume impedance	$Z = \frac{1}{j\omega C_f\left[1+(\gamma-1)\left(\frac{\tanh(\beta a)}{\beta a}\right)\right]}$ [12]	Frequency-dependent
m_d	Diaphragm acoustic mass	$m_d = \frac{m_{eff}}{A_{eff}^2}$ [9]	9.12e2 %
C_d	Diaphragm acoustic compliance	$C_d = C_m A_{eff}^2$ [9]	8.8e-16
R_{vent}	Vent resistance	$R_{vent} = \frac{1}{2\pi f_{LFRO} C_b}$ [9]	3.86e11
R_{bp}	Backplate resistance	-	1.74e8 [9]
Z_{bv}	Back volume impedance	$Z = \frac{1}{j\omega C_b\left[1+(\gamma-1)\left(\frac{\tanh(\beta a)}{\beta a}\right)\right]}$ [12]	Frequency-dependent

Table 4.1: Calculations or values that were used in the Simulink electric circuits for each element to replicate Knowles's result [9]. Frequency-dependent values have not been listed.

Element	Description	Formula	Value
a_p	Port radius	-	175e-6
$2a$	Thin parallelepiped enclosure height	-	850e-6
f_{LFRO}	Roll-off frequency	-	35 Hz
C_b	Back volume compliance	$C_b = \frac{V_b}{\gamma p_0} = \frac{V_b}{\rho_0 c_0^2}$	1.18e-14
C_f	Front volume compliance	$C_f = \frac{V_f}{\gamma p_0} = \frac{V_f}{\rho_0 c_0^2}$	9.12e2 (m^5/N)%
γ	Ratio of specific heats	$\gamma = \frac{C_p}{C_v}$	1.39 (-)
β	Convenience factor	$\beta = \sqrt{j\omega C_p/\kappa}$ [12]	Frequency-dependent
C_p	Specific heat (const. pressure)	-	1e3 (J/kg)
κ	Thermal conductivity	-	25.89e-3 (W/mK)
C_m	Diaphragm mechanical compliance	-	7.10e-3 (m/N) [9]

Table 4.2: A list of the values necessary to compute the equations listed in Table 4.1, from Ref. [9].

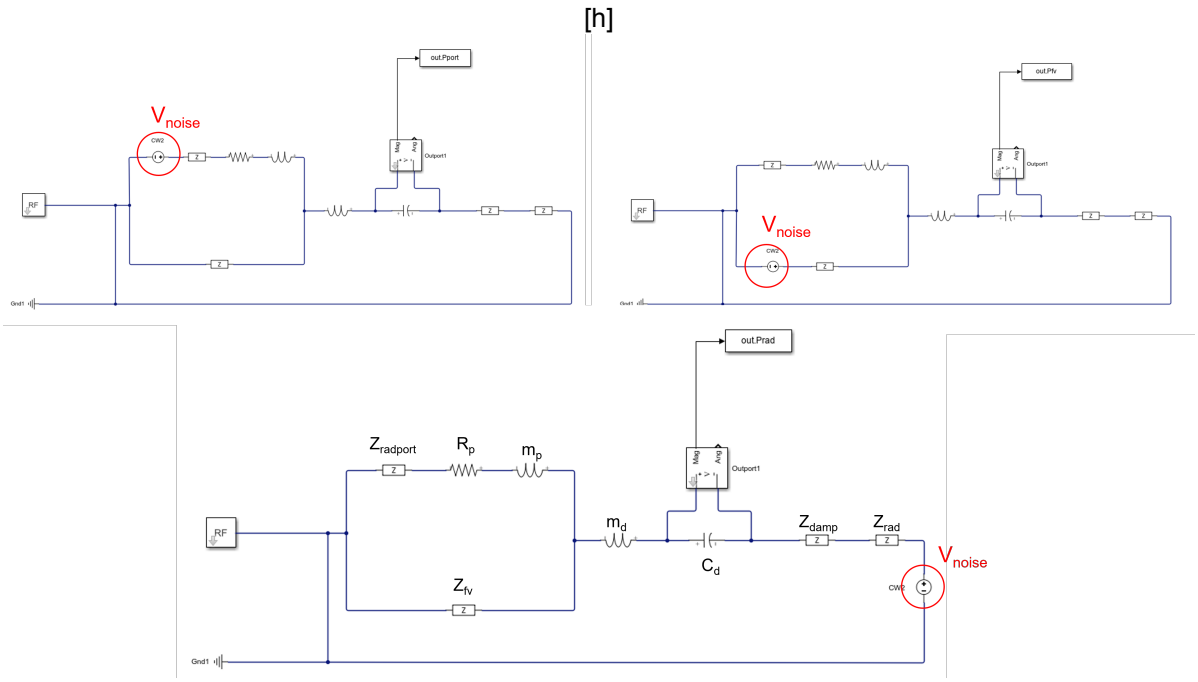

Figure 4.9: Overview of the Simulink models that were used to compute the acoustic noise spectral density of the silicon photonic microphone.

4.2.4. Integrated photonic microphone acoustic model

The model used to determine the thermo-acoustic noise of the silicon photonic microphone is based on the Knowles model, which was discussed in the previous section. However, some adjustments have been made to tailor the model to the specific measurement setup intended for use. First, the removal of the backplate in the silicon photonic microphone eliminates the corresponding resistor from the model. This omission is in essence why a silicon microphone can significantly improve the capacitive MEMS microphone.

Additionally, the design of the silicon photonic microphone does not include a ventilation hole, leading to the removal of the corresponding resistor from the model. However, it is important to note that a ventilation hole is typically required for commercial applications, and including it in the model would allow for a fair and equal comparison.

Furthermore, the back volume impedance has been replaced by radiation impedance towards the back side of the microphone, as there is no enclosure present. Though the radiation impedance is relatively small compared to the back volume impedance, for the sake of fair comparison, an enclosure impedance should be included. Since the exact enclosure size and requirements are unknown for a silicon photonic microphone, the impedance is difficult to compare and for now, excluded from the model.

This thesis focuses on achieving the best performance in a laboratory setup to establish a proof of concept. As a result, the design parameters have been chosen based on the model without a ventilation hole and enclosure impedance.

The resulting Simulink models including these adjustments are shown in Figure 4.9.

The equations for the acoustical components have been presented in the previous section, in Table 4.1 and Table 4.2. This time, the calculations are done with my own design parameters. The port resistance is calculated with the assumption that the radius of the diaphragm is equal to the port radius, $a_p = a$. The acoustic compliance of the diaphragm is calculated via the mechanical compliance, which is:

$$C_{da} = C_{dm} A_{eff}^2 = \frac{A_{eff}^2}{\omega_n^2 m_{eff}} \tag{4.8}$$

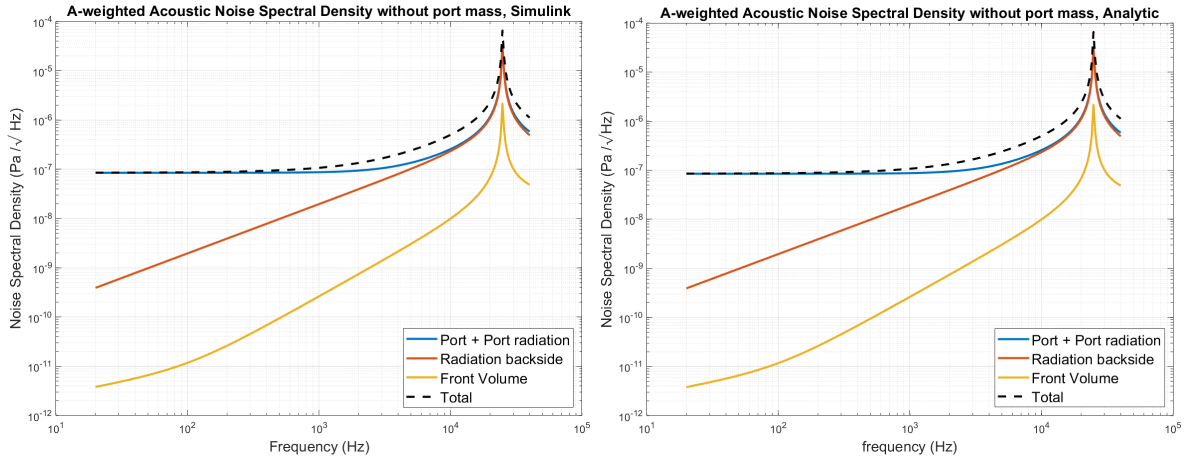

(a) Noise spectral density calculated with Simulink model.

(b) Noise spectral density calculated with analytic transfer functions.

Figure 4.10: Comparison of the result of the Simulink model and the result of the analytical transfer functions to verify the derivation of the transfer functions. The calculations are for a silicon thickness of 100 nm, a SiO_2 layer of 2.2 μm and a radius of 500 μm.

with A_{eff} the effective area and m_{eff} the effective mass of the diaphragm. In terms of the applicability of the model, some issues have been faced due to the fact that the RF Blockset of Simulink does not allow for input values below 1e-18. I obtained values for C_{da} below 1e-18, and therefore a new method had to be used. Simply scaling the system did not work, and the frequency-dependent behaviour made scaling complex. To overcome the issue, I came up with a different method, which is to derive the transfer function of the electronic circuit:

$$H(j\omega) = \frac{V_{out}}{V_{in}} \tag{4.9}$$

where $H(j\omega)$ is the transfer function defined by the electronic circuit, V_{out} is the voltage over the diaphragm capacitor, and V_{in} is the noise voltage source. The derivation for the transfer functions can be found in Appendix A.

The unexpected advantage of this method is that it allows for much faster analytical calculation of the thermo-acoustic noise. Consequently, comparing different designs becomes much more accessible and significantly improves the design process.

A disadvantage of the transfer function is that for each source, the transfer function has to be studied separately. Changing the circuit requires a new derivation of the transfer function.

The results of the transfer function are verified simply by comparing the result of the Simulink model with the results of the transfer function. These are identical as can be seen from Figure 4.10.

With the noise spectral density, Equation 4.5 is used to derive the total A-weighted noise pressure for each individual source. The total is computed as the sum of each source and gives a value for the thermal acoustic noise pressure for each design that is considered. The result that is shown in Figure 4.10 is computed with a design for a silicon diaphragm of 100 nm, a SiO_2 layer of 2.2 μm and a radius of 500 μm and the corresponding A-weighted total noise pressure is equal to 85 μPa (RMS). The calculation is only done for demonstrative purposes, the actual results are published in chapter 6.

4.3. Discussion

Several aspects of the presented thermo-acoustic noise calculations require some discussion.

First of all, the replicas of the papers that have been presented in subsection 4.2.2 and subsection 4.2.3 are not exactly identical. These differences have been discussed in the sections and are not repeated here. The reason to mention the differences is that even though I am confident that the method is correct, the missing of an identical replica leaves room for uncertainty.

Furthermore, another uncertainty comes from the calculation of the pressure noise amplitude. The outcome of the lumped element model is a noise spectral density, from which the pressure amplitude (RMS) can be calculated. However, the models that I replicated only present the noise spectral den-

sity, rather than the noise pressure. The Knowles paper does include a pie graph of the noise power contributions for the acoustic noise sources, but the calculations are not presented. It is not possible to verify my calculations only with the pie graph that is presented, since the noise spectral density is not exactly identical.

The most crucial point of discussion is the calculation of the port resistance. The model has been adapted from the Knowles model, where they present the port resistance coming from the PCB hole in front of the microphone. The resistance is calculated with the Hagen-Poiseuille equation (see subsection 2.2.8). This gives rise to two problems.

1.) My design considers a larger PCB hole than the diaphragm radius (see chapter 3, subsection 3.4.3), so I calculated the port resistance with the radius of the bottom etch (assumed to be equal to the radius of the diaphragm). The length of the port is calculated as the height of the silicon substrate, instead of the PCB thickness. It is uncertain if the port resistance can be modelled with the same acoustic circuit as presented by Knowles because of this design change.

2.) Theoretically, the Hagen-Poiseuille equation only holds for fully developed flow, often only true for longer pipe regions. As the equation is often used to model the acoustic resistance, even for small perforations (see chapter 2, subsection 2.2.9), the equation could be satisfactory. However, since the port resistance covers only a small part of the MEMS microphone acoustic noise, it could very well be that the equation is not a good approximation of the port resistance defined by the bottom etch.

It is desired to do further research on how to model the port resistance of the bottom etch, and compare the aforementioned two design options with a smaller and larger PCB acoustic hole. The boundary layers at the port should be studied, including the losses that are associated with them. I tried to model the port resistance with the thermo-viscous module available in COMSOL. Unfortunately, after one week I did not obtain any usable results and prioritized studying the mechanical behaviour first. The mechanical behaviour and optomechanical interaction are presented in the next chapter.

5 Optomechanical modelling

As discussed in the working principle chapter 3, section 3.3, the deformation of the diaphragm modulates the optical signal. To quantify the modulation, the relation between mechanical deformation and the change in optical signal has to be studied, referred to as optomechanical modelling. This chapter explains the optomechanical modelling done in this thesis. First, the equations necessary to calculate the deformation of the diaphragm are presented. These are used to quantify the change in optical path length as the change in ring radius. Secondly, it is described how the equations are implemented as analytical models. Hereafter, it is presented how the finite element software COMSOL is used to verify the analytical results. Then, the mechanical deformation is related to the change in transmission of the ring resonator as the microphone's sensitivity function. Also, the effect of the sensitivity of the microphone on the SNR is discussed. The chapter concludes with a more general discussion of the aforementioned topics.

5.1. Diaphragm deformation

To calculate the sensitivity of the microphone and its SNR, the diaphragm deformation plays an essential role. The deformation of the diaphragm changes the optical path length of the ring resonator, consequently modulating the intensity of light measured at the photodetector. The following section presents the equations and assumptions employed to derive the diaphragm's deformation, with additional derivations provided in the Appendix.

5.1.1. Free vibration of a circular clamped plate

To find the deformation of the diaphragm, the vibrations of plates theory is used. A more extensive derivation is written in Appendix C. The equations are sourced from Ref. [78] and apply to a clamped circular plate made of a homogeneous isotropic material, under a uniform harmonic load normal to the surface. The aforementioned reference considers density as weight per area, which is changed to weight per volume in this thesis for clarity reasons. The equations only hold for deflections small compared to the thickness. The deflection W of a circular clamped plate can be found by multiplying the central displacement w_0 with the corresponding mode shape. Because of symmetry, the presented mode shape only depends on radial coordinate r:

$$W(r) = w_0 \left(\frac{J_0(\lambda_{01}\frac{r}{a})I_0(\lambda_{01}) - J_0(\lambda_{01})I_0(\lambda_{01}\frac{r}{a})}{I_0(\lambda_{01}) - J_0(\lambda_{01})} \right) \tag{5.1}$$

with J_n the Bessel function and I_n the modified Bessel function of the order n, a the diaphragm radius, $\lambda_{01} = 3.196$ the root of the first mode shape. Only the first mode shape is considered because the system will operate below the first resonance, and excitation is assumed to be uniform across the diaphragm. The eigenfrequency corresponding to the first mode can be found with:

$$\omega_{01} = \left(\frac{\lambda_{01}}{a} \right)^2 \sqrt{\frac{D}{\rho h}} \tag{5.2}$$

with D the bending rigidity defined as:

$$D = \frac{Et^3}{12(1-v^2)} \tag{5.3}$$

where E is the Young's modules, t the thickness of the plate and v Poisson's ratio.

The central deflection is calculated by adding a force to a damped oscillator. This makes it possible to calculate the harmonic behaviour of the plate. The equations for a single mass-spring-damper are found in Appendix B; how a circular clamped plate is converted to a single mass-spring-damper with an effective mass, stiffness and surface area is shown in Appendix C.

For a clamped circular plate, the effective moving mass is equal to:

$$m_{eff} = 0.2 \cdot m_{diaphragm} \tag{5.4}$$

The effective stiffness is:

$$k_{eff} = \omega_{01}^2 \, m_{eff} \tag{5.5}$$

The impedance of a damped oscillator with effective mass and stiffness is:

$$Z_m = c + j\omega m_{eff} - \frac{k_{eff}}{j\omega} = \frac{U_{m_{eff}}}{F} \tag{5.6}$$

where c is the mechanical damping of the plate determined by the Q-factor, $U_{m_{eff}}$ the velocity of the mass and F the harmonic load on the diaphragm. Now the central displacement of the diaphragm at frequency ω can be found as:

$$w_0 = \left| \frac{p \, A_{eff}}{j\omega(Z_m)} \right| \tag{5.7}$$

with p the pressure of the sound wave and A_{eff} the effective area of a circular clamped plate:

$$A_{eff} = \frac{A_{diaphragm}}{3} \tag{5.8}$$

It is convenient to write the deflection in terms of impedance because other impedances on the diaphragm can be easily added.

5.1.2. Add radiation impedance

Radiation impedance has been discussed in chapter 2, subsection 2.2.4. The total mechanical radiation impedance on a circular piston in an infinite rigid baffle is [54]:

$$\boldsymbol{Z}_{rad} = \frac{\boldsymbol{F}_S}{\mathbf{u}} = \rho_0 c \pi a^2 \left[1 - \frac{J_1(2ka)}{ka} + j \frac{H_1(2ka)}{ka} \right] \tag{5.9}$$

where J_1 is the first order Bessel function and H_1 the first order Struve function. The radiation impedance is added to the single mass-spring-damper model as follows:

$$w_0 = \left| \frac{p \, A_{eff}}{j\omega(Z_m + Z_{rad})} \right| \tag{5.10}$$

The radiation impedance will shift the resonance frequency to the left in the frequency spectrum, and dampen the resonance itself. The smaller the microphone, the larger this effect. The graph in Figure 5.1 shows the effect on the resonance frequency.

The designed diaphragm should always exhibit a resonance frequency of at least 25 kHz. The resonance frequency in air is determined by identifying the frequency at which the deflection reaches its maximum value.

With an estimation of the resonance frequency in air, the next critical consideration in terms of deformation concerns the stiffness of a dual-layered diaphragm. The upcoming section studies the flexural rigidity of a multilayered circular plate.

5.1.3. Flexural rigidity of multilayered circular plates

The equations that have been discussed so far assume an isotropic material with constant thickness across the whole diaphragm. This subsection discusses how the additional layer deposited on the silicon diaphragm is modelled in this thesis.

To find the deflection with an additional layer, the flexural rigidity D in C.4 has to be corrected. For a multi-layered plate with isotropic materials, the flexural rigidity for n layers is [79]:

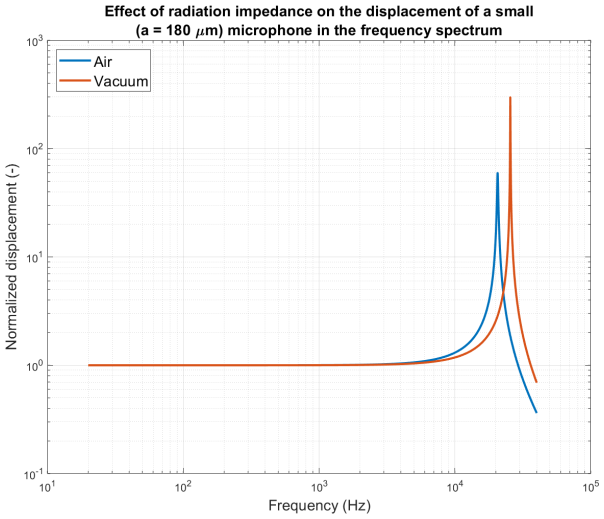

Figure 5.1: Effect of the surrounding air on the resonance frequency, calculated by adding the radiation impedance as in Equation 5.10.

$$(EI)_{\text{eq}} = D_{lay} = \sum_{k=1}^{n} \frac{t_k^3 E_k}{12} + \left(\sum_{k=1}^{n} t_k E_k\right)^{-1} \sum_{1 \le k < l \le n} t_k E_k \cdot t_l E_l \cdot (m_k - m_l)^2 \tag{5.11}$$

with I the moment of inertia, E_k and t_k are the elastic modulus and thickness of each individual layer, respectively, and

$$m_k - m_l = \frac{t_k}{2} + t_{k+1} + ... + t_{l-1} + \frac{t_l}{2} \tag{5.12}$$

represents the distance between the middle planes of the layers, see Figure 5.2.

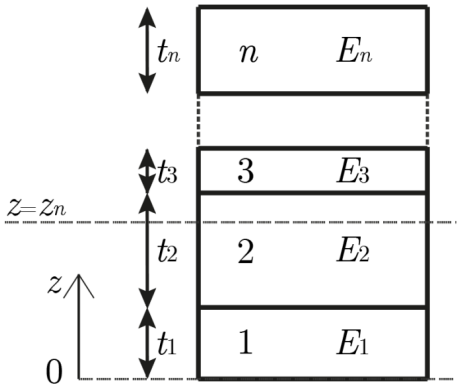

Figure 5.2: A multilayered beam structure for which the flexural rigidity is calculated with Equation 5.11, taken from Ref. [80].

The Poisson's ratio is not equal for all materials and is calculated as average with:

$$v_{avg} = \frac{v_1\, t_1 + v_2\, t_2}{t_1 + t_2} \tag{5.13}$$

where v_1, v_2, t_1 and t_2 represent the Poisson's ratio and thickness of the first and second layer, respectively. With the new flexural rigidity and average Poisson's ratio, the eigenfrequency of a dual-layered structure can be calculated. Equation 5.2 slightly changes to:

$$\omega_{01} = \left(\frac{\lambda_{01}}{a}\right)^2 \sqrt{\frac{D_{lay}}{\rho_1 t_1 + \rho_2 t_2}} \tag{5.14}$$

The neutral axis of the multilayered beam is used in the next section to compute the change in ring radius, and, for two layers, is given by [81]:

$$z_n = \frac{\frac{t_1}{2} E_1 \, t_1 + (\frac{t_2}{2} + t_1) E_2 \, t_2}{E_1 \, t_1 + E_2 \, t_2} \tag{5.15}$$

The material properties considered for this thesis are imported from COMSOL and are found in Table 5.1.

Table 5.1: Material Properties considered in this thesis, imported from COMSOL.

Layer Material (-)	Young's Modulus (E) (GPa)	Poisson's ratio (v) (-)	Density (ρ) (kg/m^3)
Si	170	0.28	2329
SiO_2	70	0.17	2200
Si_3Ni_4	250	0.23	3100
SiC	748	0.45	3216
PDMS	7.5×10^{-4}	0.49	970

5.1.4. Change in ring radius

The optical path length of the ring is calculated as the circumference, which is a function of the ring radius. Therefore, the mechanical deformation analysis is meant to derive the change in ring radius, referred to as db in this thesis.

To find the change in ring radius, the deflection in the radial direction at the location of the ring is studied. An indication of the deformed profile of the ring waveguide is shown in Figure 5.3. The neutral axis of the combined structure and of the ring are indicated as well.

For pure bending (valid for small deflections), the transverse section remains perpendicular to the neutral axis. Consequently, the deflection is solely originating from compression and tension above and underneath the neutral axis. Therefore, the change in the radius of the ring itself is not uniform across the surface area of the cross-section of the ring. To find the total radial displacement, the average radial displacement of the surface area of the ring is taken as the total change in ring radius. In Figure 5.3, the surface area of the ring is the silicon (grey) part that has a higher thickness compared to the rest of the silicon layer. It is assumed that the average displacement is equal to the displacement at the neutral of the ring.

To calculate the radial displacement, the curvature of the diaphragm at the position of the ring is taken as dw/dr, evaluated at r = b. This is indicated as θ in Figure 5.3. The central z-coordinate of the ring and dual-layered structure is used to compute the average radial displacement as:

$$db = \frac{dw}{dr}(z_r - z_n) \tag{5.16}$$

with z_n given by Equation 5.15, and $z_r = t_{ring}/2$. dw/dr is the derivative of Equation 5.1 and is found with the MATLAB symbolic toolbox. When evaluated at r = b, this results in:

$$\left(\frac{dw}{dr}\right)_{r=b} = w_0 \left(\frac{\lambda_{01}}{a}\right) \frac{I_1(\lambda_{01}\frac{b}{a})J_0(\lambda_{01}) + J_1(\lambda_{01}\frac{b}{a})}{I_0(\lambda_{01}) - J_0(\lambda_{01})} \tag{5.17}$$

Note that the mode shape is derived from the vacuum vibration theory and that the central deflection is derived from the mass-spring-damper which includes radiation impedance. All the equations required to calculate the change in optical path length are discussed. The next section presents how they are implemented in the analytical models.

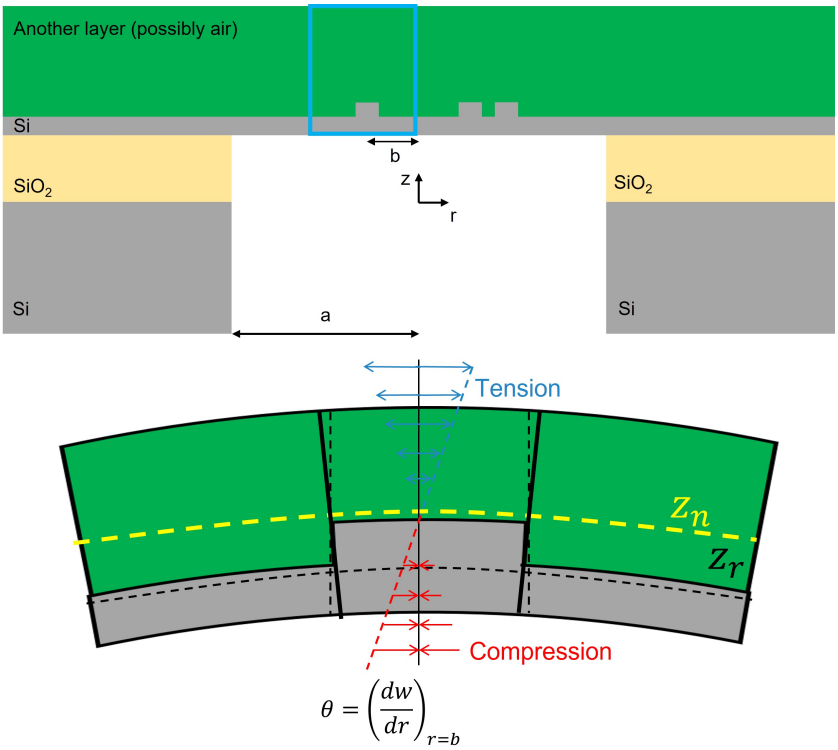

Figure 5.3: Schematic overview of the deformation profile of the layered plate at the location of the ring waveguide. The location of the close-up is indicated by the box in light blue.

5.2. Analytical models

The previous section has summarized the theory that is used to analytically derive the deformation of the diaphragm. This section aims to give more insight into how the equations are set up to analytically compute the desired outputs, referred to as analytical models.

The underlying idea is to compare and optimize different design options. Furthermore, the results will be verified with finite element models. Analyzing all the design options in a finite element model requires significant computational effort, which is undesirable for a design process. The analytical models are used to provide a specified design input for the finite element models, to significantly reduce the computation effort.

A distinction has been made between the model with and without a layer. The models *without* a layer aim to answer the following questions:

1. What radius is required to have a resonance frequency of 25 kHz, when the silicon thickness is either 100, 150 or 220 nm, considering the effect of the surrounding air?
2. What is the change in ring radius (db) of the ring waveguide for a pressure of 1 Pa with a frequency of 1 kHz, considering the effect of the surrounding air?

The models *with* a layer aim to answer the following questions:

1. What layer thickness is required to have a resonance frequency of 25 kHz, when the silicon thickness is either 100, 150 or 220 nm, and the radius is swept between 100 and 500 μm, considering the effect of the surrounding air?
2. What is the change in ring radius (db) of the ring waveguide for a pressure of 1 Pa with a frequency of 1 kHz, considering the effect of the surrounding air?

5.2.1. Without layer

Resonance frequency: Mostly, the air surrounding the diaphragm makes the calculation of the resonance frequency somewhat difficult. From Equation 5.10 it can be seen that the resonance occurs

when Zdamp + Zrad = 0, however, this equation does not have a solution. One approach is to minimize Zrad + Zdamp. Unfortunately, I could not get a solver to work properly. The other approach is to calculate the central deflection for a range of frequencies and find the designs that have a maximum deflection at around 25 kHz. The result is the radius that gives a resonance frequency of a silicon thickness of 100, 150 or 220 nm.
Change in ring radius db: The previous results are now used as the input values to calculate the change in ring radius at 1 kHz of 1 Pa. The steps are as follows:

1. Specify the material properties.
2. Import the design values that give a resonance frequency of 25 kHz.
3. Find w_0 with Equation 5.10.
4. Use the value of w_0 to calculate dw/dr with Equation 5.17.
5. Use the value of dw/dr to calculate db with Equation 5.16.

Note that the neutral axis defined in Equation 5.15 is simply equal to $0.5 * t_1$ where t_1 equals the thickness of the silicon layer. Therefore, when the silicon layer thickness is equal to the thickness of the ring of 220 nm, the resulting radial displacement of the ring is equal to zero. The underlying reason for this is that for plate bending theory when the part below the neutral axis of the diaphragm is elongated (tension), the top part is compressed. When the neutral axis is equal to the neutral axis of the ring, the resulting radial displacements cancel each other. This effect is visualized in Figure 5.4. The image is somewhat misleading because the ring itself always needs a thinner silicon part next to it to form a RIB waveguide and guide the light, but removing a small part next to the waveguide will not have a significant effect on the neutral axis. The option of 220 nm is only considered analytically for efficiency reasons.

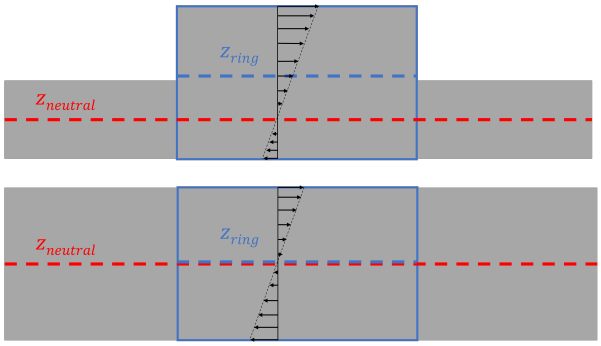

Figure 5.4: Visualization of the neutral axes (dotted lines) and the resulting radial displacement field (black arrows) of the ring for two different silicon thicknesses, to indicate a net displacement of zero when the neutral axis is equal to the ring axis.

5.2.2. With layer

As explained in subsection 5.1.3, the dual-layered structure requires a different approach in terms of mechanical calculations, but also in terms of setting up the model. In contrast to the silicon thickness, the deposited layer thickness can have any value and is not limited by the fabrication process as much. Furthermore, the equations given in subsection 5.1.3 should be used to find the resonance frequency and change in ring radius.

Resonance frequency: The approach with an additional layer is similar to the one without a layer. This time the effective stiffness is calculated by inserting Equation 5.14 in Equation 5.5. Additionally, the effective mass is adjusted. To ensure a limited number of solutions, the range or radii is discretized linearly. For each radius, a corresponding layer thickness is found to achieve the desired resonance frequency of 25 kHz. The steps are repeated for each material and silicon layer thickness.
Change in ring radius db: The previous results are now used as the input values to calculate the change in ring radius at 1 kHz of 1 Pa. The steps are as follows:

1. Specify the material properties of silicon and the layer material.

2. Import the design values that give a resonance frequency of 25 kHz.
3. Find w_0 with Equation 5.10.
4. Use the value of w_0 to calculate dw/dr with Equation 5.17.
5. Use the value of dw/dr to calculate db with Equation 5.16.

The analytical models give the mechanical deformation of the diaphragm, which can be used to derive the sensitivity of the microphone. As mentioned, the values of the radius, silicon thickness and layer thickness are also used as input for finite element models, which are discussed in the next section.

5.3. Finite Element Models

The analytical models are compared with the finite element solver COMSOL to validate and verify the results. This approach allows for more confidence in both the outcome of the analytical and numerical results. Through verification, any errors that might arise can be effectively identified and corrected. The outcome and comparison between the analytical and numerical results are shown in chapter 6, section 6.1. The main aim of this section is to provide a comprehensive insight into the finite element modelling that has been done in this thesis.

To reduce computational efforts, the simulations are separated into three different models to study the mechanical deformation of the diaphragm. The models are used to calculate the following:

1. The eigenfrequency of the diaphragm with and without an additional layer, in vacuum
2. The eigenfrequency of the diaphragm with and without an additional layer, in air
3. The change in ring radius with and without an additional layer, in air, to an input pressure of 1 pascal at 1 kHz.

The next subsection addresses some general knowledge of finite element modelling which is required to understand the model choices.

5.3.1. General knowledge of finite element software

The most basic knowledge of finite element modelling is left out of this thesis, only parts that influence the approach are explained. The focus of the explanation is on the software program COMSOL.

Parametric sweep: Parameters that are used to design the model can be adjusted, and it is possible to sweep values of certain parameters with a vector of specified values. Either all possible combinations or specified combinations are studied. When studying specified combinations, all vectors should have the same length, which makes the computation more complex when not all combinations are required. For example, considering different thickness layers of silicon and sweeping the layer thickness for specified combinations is not an option because the silicon only has 3 thickness options of 100, 150 and 220 nm.

Frequency domain study: A frequency domain study changes the input to a harmonic signal, in our case the input pressure. Since frequency-dependent behaviour is essential in microphones, the studies performed in this thesis are frequency domain studies. It should be mentioned that with frequency domain studies, it is not possible to change the mesh for each frequency that is studied. With a parametric sweep, the mesh is adjusted for each study. By sweeping the frequency as a parameter, it is possible to achieve frequency-dependent meshes. Because the size of the air mesh depends on the frequency, it can be useful to change the mesh for large frequency ranges.

Axisymmetric model: All the studies performed for this thesis are axisymmetric models, which greatly reduces the computation time. Therefore, all the snapshots should be interpreted as 3D models. Figure 5.5 gives more detail about the axisymmetric condition that is applied in the models.
As explained in section 3.2, there are different options in layer material and silicon thickness. Additionally, it is possible to have no layer at all and simply let air be the cladding of the waveguide. An overview of all the different models is shown in Figure 5.6.

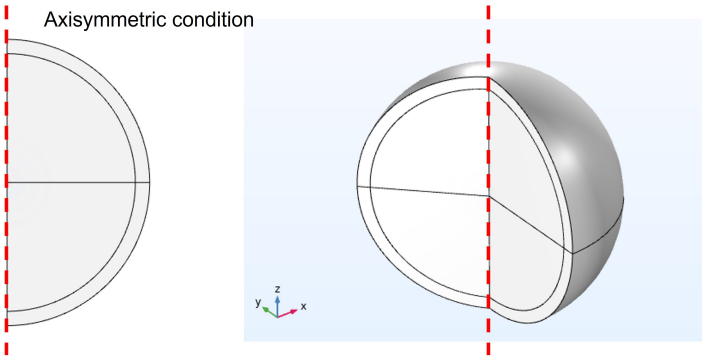

Figure 5.5: Visualization of the axisymmetry condition applied to all models

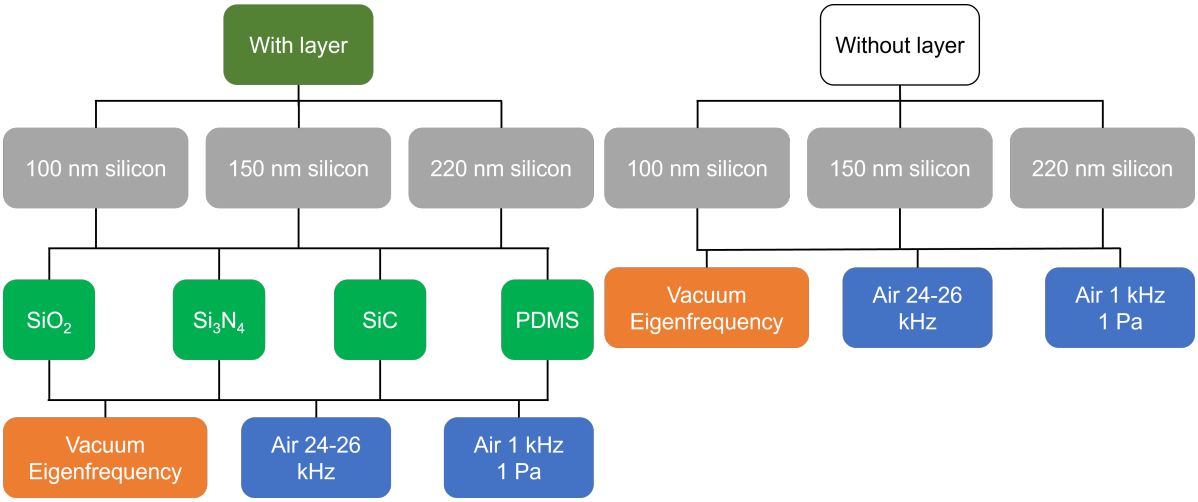

Figure 5.6: Overview of the different COMSOL models that have been set up to perform the numerical studies.

5.3.2. Eigenfrequency in vacuum

The first model is the simplest one as it does not require any acoustic modelling because it operates in vacuum. The model includes the silicon layer, the deposited layer and the silicon ring waveguide. The geometry is shown in Figure 5.7, in which also the design variables are indicated. The model uses the eigenfrequency study available in COMSOL to find the first resonance of the model. The goal of this model is to compare the natural resonance frequency of the diaphragm with that of the analytical calculations, which is calculated with Equation 5.2. Especially for the layered structure, this is a critical model to verify the results, since analytical calculation of the flexural rigidity is not straightforward (see Equation 5.11 and Equation 5.14) and should be verified.

5.3.3. Eigenfrequency in air

The model that computes the eigenfrequency in air is different from the eigenfrequency in vacuum model. The air is added as a sphere around the diaphragm. An extra layer is added at the end of the sphere as a perfectly matched layer (PML), see Figure 5.8. The PML absorbs the pressure waves and makes sure that no reflections occur. When the same eigenfrequency study is performed with the air layer around the diaphragm, the solver is not consistently finding the value of the first resonance. The results were not even close, had large complex values and varied a lot between different sizes. Therefore, I used the central deflection to find the resonance frequency; the method is adapted as follows:

1. Use the analytical models to find the combinations of values for silicon thickness, radius and layer thickness for a resonance frequency in air of 25 kHz.
2. Save the corresponding resonance frequency in air (because of the tolerance, it is slightly different than exactly 25 kHz).

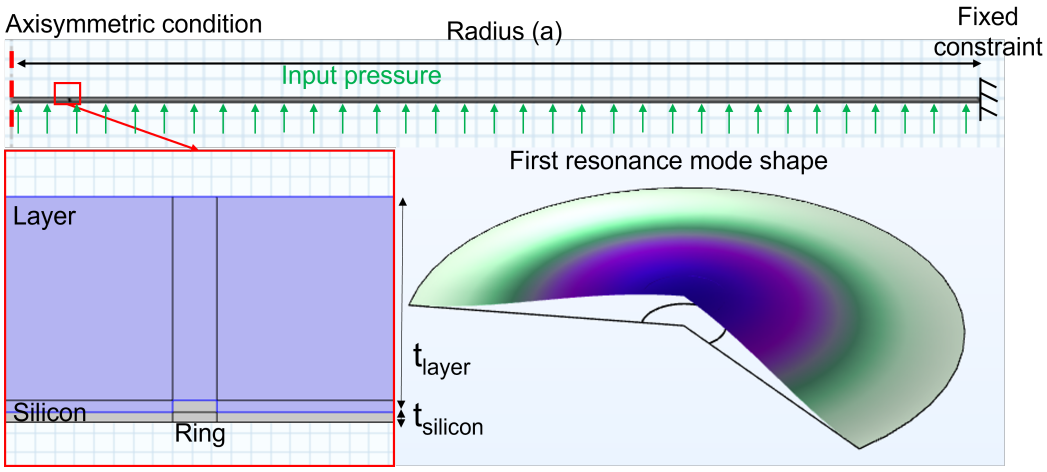

Figure 5.7: Snapshots of the COMSOL resonance in vacuum model to indicate design variables and show what is studied.

3. Import the values of step 1 into COMSOL as a .txt file and compute a parametric sweep of the specified combinations in a frequency domain study between 25 $\pm x$ kHz.
4. Make sure to track the deflection of the centre of the diaphragm for each frequency that COMSOL studies.
5. Export the results from COMSOL to a .txt file and import them to MATLAB.
6. Find for each set of combinations, for which frequency the deflection is maximum, and save the corresponding frequency.
7. Make sure that for all combinations of design variables and materials, the maximum deflection does occur within 25 $\pm$ $< x$ kHz.
8. Repeat for all layer materials.

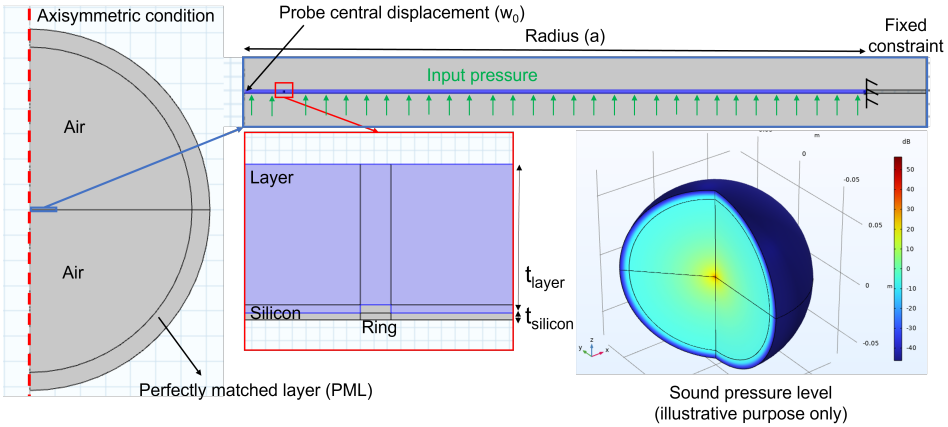

Figure 5.8: Snapshots of the COMSOL resonance in air model to indicate design variables and show what is studied. A central deflection probe is added, and it is illustrated how the perfectly matched layer (PML) absorbs the pressure field.

5.3.4. Change in ring radius

The last model determines the final sensitivity of the microphone, by measuring the change in radius of the silicon ring waveguide. This time, the frequency is fixed at 1 kHz and the input pressure at 1 Pa. These values are chosen because the sensitivity of MEMS microphones is often presented as the sensitivity at 1 kHz and 1 Pa (which equals 94 dB SPL). The model includes radiation impedance by surrounding the diaphragm with a sphere of air. The same specified combinations of the design variables that result in a resonance frequency of 25 kHz in air are used as input. The output is the

average radial displacement of the domain of the ring waveguide. This is shown in Figure 5.9. The right image of the figure includes an indication of the displacement field, which is in line with the expected displacement field of a plate.

The radial displacement of the ring is the desired outcome of the mechanical analysis. These results can then be used to calculate the change in optical path length and see how it would affect the transmission of a ring resonator. This will be discussed in the next section as the sensitivity of a silicon photonic microphone.

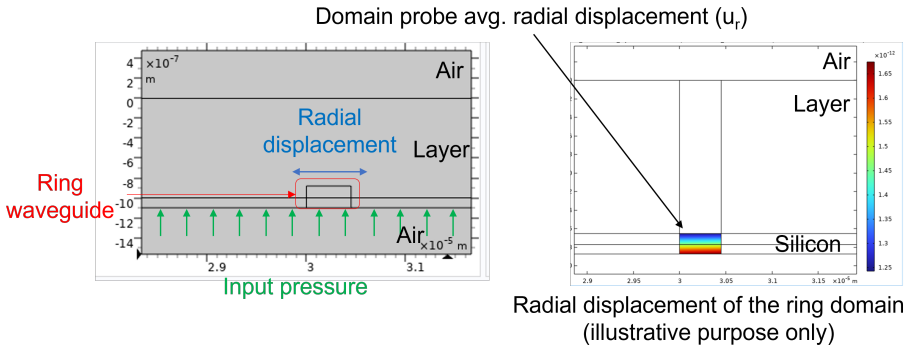

Figure 5.9: The change in ring radius is measured as the average radial displacement of the ring domain surface area.

5.4. Sensitivity of a silicon photonic microphone

This section discusses the sensitivity of a silicon photonic microphone, and how it can be improved. The aim is to explain how sensitivity influences design choices. The section starts with a general comment on the sensitivity notation, derives the optomechanical sensitivity function, and ends with a note on how sensitivity and SNR relate to each other.

5.4.1. Sensitivity notation

It is important to make a note about the sensitivity notation of optical microphones. Whereas traditional microphones have two transduction mechanisms, namely from input pressure to mechanical deformation and from mechanical deformation to an electric signal, optical microphones have three transduction mechanisms [18]:

1. Acoustic $\rightarrow$ Mechanical
2. Mechanical$\rightarrow$ Optical
3. Optical $\rightarrow$ Electrical

For traditional microphones, the sensitivity is usually denoted by dV/dp in mV/Pa or dBV/Pa with the audible threshold as a reference. When this notation is used for optical microphones, it is difficult to distinguish the sensitivity loss in the optomechanical and optoelectrical domains. As the optoelectrical component is not the main subject of this paper, it is not researched further. Consequently, in terms of sensitivity the interest is in the acousto-mechanical and optomechanical domains (from acoustic pressure to optical power). For a silicon photonic microphone, with an integrated ring resonator on the diaphragm, this means the sensitivity analysis is a study of change in transmission in the ring resonator by a certain incoming sound pressure: dT/dP.

5.4.2. Sensitivity function

The study of dT/dP requires a broad understanding of all the underlying physics that occur. The basic understanding is that the mechanical signal changes the optical path length and alters the destructive interference after one roundtrip of the ring. It is discussed in section 3.3 that this requires the wavelength of the laser to be at the flank of a resonance dip. To understand dT/dP, we must look closely into the equation of the transmission of a ring resonator (Equation 2.59), which was given in chapter 2, subsection 2.3.4:

$$T(\theta, \alpha, \tau) = \frac{\alpha^2 + |\tau|^2 - 2\alpha|\tau|\cos(\theta)}{1 + \alpha^2|\tau|^2 - 2\alpha|\tau|\cos(\theta)} \tag{5.18}$$

The transmission coefficient τ depends on the design of the sensor and is determined by the waveguide dimensions and its cladding, the ring radius and the distance between the straight waveguide and ring. The relative power after one roundtrip α^2 depends on the waveguide losses. The waveguide losses have different roots, such as surface roughness, and must be determined experimentally. The loss that occurs due to bending in the waveguide is known as bending loss, which increases with smaller radii and thus forms a limit on the minimum size of the ring radius. An estimation from preliminary studies from within the research group of PME that studies silicon photonic sensors, a minimum radius of 30 μm of the ring was found, which is considered the limit for this thesis. The waveguide losses can only be determined experimentally and are estimated as 3 dB/cm loss. Remember that α represents the loss after one roundtrip, and therefore depends on the ring radius b:

$$\alpha = 10^{-2\pi b \cdot \text{loss}} \tag{5.19}$$

with loss the waveguide losses in dB per meter. The phase θ after one round trip depends on the laser wavelength λ, ring radius b and effective index n_e of the guided mode:

$$\theta = \frac{4\pi^2}{\lambda} n_e b \tag{5.20}$$

Next, all the variables in Equation 5.18, Equation 5.19, and Equation 5.20 that are influenced by a change in pressure P should be analysed. The pressure induces strain on the waveguides; in 2014 Westerveld et al. studied the shift in resonance wavelength of ring and racetrack resonators [82] due to strain. Four physical effects of elongating a ring resonator are mentioned:

1. strain increases the ring radius b so also the resonance wavelength changes (see Equation 5.20)
2. waveguide cross-section shrinks due to Poisson effect (changes effective index n_e)
3. change of permittivity of dielectric material (photo-elastic effect, changes effective index n_e)
4. dispersion (wavelength dependency of the effective index) affects the shift in resonance wavelength

Note that the effect of dispersion is mostly relevant when the effect of strain is studied by measuring the change in resonance frequency by sweeping the wavelength of the laser. It is concluded that the effect of change in radius is about three times larger than the effect of change in the effective index. Rochus et al., who published the silicon photonic microphone based on an MZI mentioned in subsection 1.2.1, calculated the effect of elongation as 10 times larger than the effect of change in the effective index by[30]. For simplicity reasons, I will only look into a change of radius and neglect dispersion and effective index changes. Therefore, the sensitivity function dT/dP can be written as:

$$\frac{\partial T}{\partial P} = \frac{\partial T}{\partial \theta}\frac{\partial \theta}{\partial b}\frac{\partial b}{\partial P} \tag{5.21}$$

The first part of the equation is equal to [37]:

$$\frac{\partial T}{\partial \theta} = \frac{2\alpha\tau(1-\alpha^2)(1-\tau^2)\sin(\theta)}{(1 + \alpha^2\tau^2 - 2\alpha\tau\cos(\theta))^2} \tag{5.22}$$

For small changes in radius, the phase delay caused by the deformation will be small, and it is possible to use small angle approximations $\sin(\theta) \approx \theta$. With some rewriting equation Equation 5.18 can be rewritten as [37]:

$$T \approx 1 - (1 - T_{min})\frac{0.25\Gamma^2}{0.25\Gamma^2 + \theta^2} \tag{5.23}$$

with

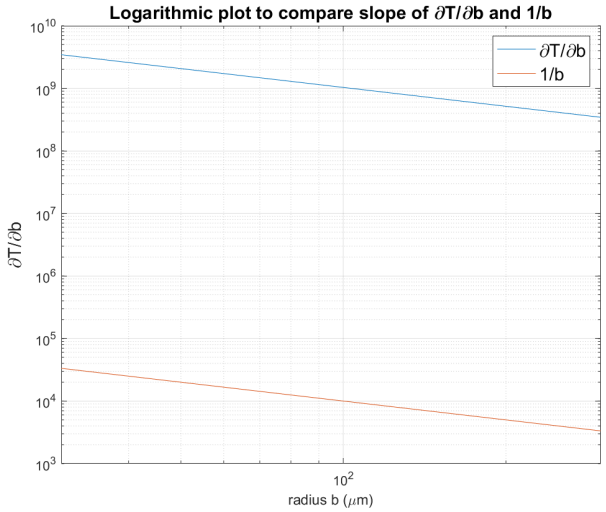

Figure 5.10: Comparison of $\partial T/\partial b$ and 1/b on a logarithmic scale, the equal slope indicates that $\partial T/\partial b \propto 1/b$.

$$T_{min} = \frac{(\alpha - \tau)^2}{(1 - \alpha\tau)^2} \tag{5.24a}$$

$$\Gamma = \frac{2(1 - \alpha\tau)}{\sqrt{\alpha\tau}} \tag{5.24b}$$

The maximum sensitivity is at $\theta = \Gamma\sqrt{3}/6$ and taking the derivative of Equation 5.25 the sensitivity with respect to θ is [37]:

$$\left.\frac{\partial T}{\partial \theta}\right|_{\theta=\Gamma\sqrt{3}/6} = (1 - T_{min})\frac{3\sqrt{3}}{4\Gamma} \tag{5.25}$$

It was numerically obtained that the highest sensitivity of Equation 5.25 is found when $\tau \approx \sqrt{\alpha}$ [37]. For this thesis, it is assumed that the design of the ring resonator is such that $\tau \approx \sqrt{\alpha}$. The second term is found directly from Equation 5.20 and is simply equal to:

$$\frac{\partial \theta}{\partial b} = \frac{4\pi^2}{\lambda} n_e \tag{5.26}$$

With these equations, it is possible to understand the influence of a change in ring radius on the transmission of the ring resonator. In Figure 5.10 it can be seen that the first part of the transmission sensitivity is $\partial T/\partial b \propto 1/b$.

The second part is the change in ring radius due to pressure $\partial b/\partial P$, which is separated into two parts:

$$\frac{\partial b}{\partial P} = \frac{\partial b}{\partial w_0}\frac{\partial w_0}{\partial P} \tag{5.27}$$

To understand these relationships, Equation 5.10 and Equation 5.16 are evaluated. The first partial derivative of b with respect to w_0 can be found by substituting Equation 5.17 into Equation 5.16, and then it can be seen that:

$$\frac{\partial b}{\partial w_0} = \left(\frac{\lambda_{01}}{a}\right)\frac{I_1(\lambda_{01}\frac{b}{a})J_0(\lambda_{01}) + J_1(\lambda_{01}\frac{b}{a})}{I_0(\lambda_{01}) - J_0(\lambda_{01})}(z_r - z_n) \tag{5.28}$$

The second part, the partial derivative of w_0 with respect to P comes from Equation 5.10 and is equal to:

$$\frac{\partial w_0}{\partial P} = \frac{A_{eff}}{j\omega(Z_m + Z_{rad})} \tag{5.29}$$

Now, all the equations have been set up to find the optimal design. In summary, when neglecting changes in the effective index, the first part of the sensitivity equation 5.21, $\partial T/\partial b$, is proportional to 1/b. The highest sensitivity is reached for $\tau \approx .\sqrt{\alpha}$ at $\theta = \Gamma\sqrt{3}/6$, which represents the flank of the transmission dip. The second part of the sensitivity equation, $\partial b/\partial P$ will be discussed in the results because it requires the outcome of the analytical and COMSOL models.

5.4.3. Effect of sensitivity on SNR

Increasing the sensitivity of a microphone does not necessarily mean that the SNR is increased as well. When the noise source is amplified by the same amount as the signal, no improvements in the SNR are realised. Therefore, the sensitivity equation is studied again, but now only to mention the effect on the SNR. To do so, it is important to consider different noise types of the microphone. For the SNR analysis, the following noise types are considered:

- Thermal acoustic noise
- Laser intensity noise
- Laser wavelength noise
- Photodetector noise

Thermal acoustic noise is an acoustical noise type, that is modelled as small pressure fluctuations. Laser intensity noise means that the intensity of the laser is not perfectly consistent, which results in small fluctuations in the output voltage of the photodetector, even without any movement of the microphone. Laser wavelength noise refers to the fact that the wavelength of the laser is not perfectly constant, which results in a change in transmission. Photodetector noise refers to the change in output voltage without any change in laser intensity, laser wavelength or diaphragm position. These noise types will be discussed for each part of the sensitivity function. The purpose of this analysis is not to study each noise type in detail, but only to discuss how they influence the design choices that are made. The signal is considered as a 1 kHz pressure wave of 1 Pa.

Optical sensitivity

The optical sensitivity is analysed as $\partial T/\partial b$ and corresponds to the influence of a change in ring radius on the output signal. Increasing the optical sensitivity results in a larger signal for the same change in radial displacement of the ring and thus increases the signal. The effect of increasing the optical sensitivity on each noise type is discussed below.

Thermal acoustic noise: This noise type induces pressure fluctuations which result in a small radial displacement of the ring. Therefore, increasing $\partial T/\partial b$, means that the thermal acoustic noise is increased by the same amount as the original pressure signal, and as a result, the SNR will not improve when only thermal acoustic noise is considered.

Laser intensity noise: The laser intensity does not influence the optical sensitivity. Therefore, improving the optical sensitivity will increase the SNR when only laser intensity noise is considered. The laser intensity noise will not influence any of the design choices regarding optical sensitivity.

Laser wavelength noise: To understand the influence of wavelength noise, the effect of changing λ is studied. From Equation 5.20 it is evident that $\partial\theta/\partial\lambda$ is proportional to b. However, since $\partial T/\partial\theta$ is proportional to 1/b, the ring radius has no effect on the wavelength noise. In essence, improving the steepness of the flank of the transmission dip increases the signal and laser wavelength noise by the same amount, and therefore, design choices to improve the steepness of the curve do not improve the SNR when only wavelength noise is considered.

Mechanical sensitivity

The mechanical sensitivity is analysed as $\partial b/\partial P$. Increasing the mechanical sensitivity results in a larger radial displacement of the ring for the same input signal and thus increases the signal. The effect of increasing the mechanical sensitivity on each noise type is discussed below.

Thermal acoustic noise: This noise type induces pressure fluctuations which result in a small radial displacement of the ring. Therefore, increasing $\partial b/\partial P$, means that the thermal acoustic noise is increased by the same amount as the original pressure signal, and as a result, the SNR will not improve when only thermal acoustic noise is considered.

Laser intensity noise: The laser intensity does not influence the mechanical sensitivity. Therefore, improving the mechanical sensitivity will increase the SNR when only laser intensity noise is considered. The laser intensity noise will not influence any of the design choices regarding mechanical sensitivity.

Laser wavelength noise: Improving the mechanical sensitivity results in a larger change in the resonance wavelength of the ring resonator. The measured signal due to laser wavelength noise is independent of the mechanical sensitivity, and therefore, improving the mechanical sensitivity will improve the SNR, when only laser wavelength noise is considered.

In summary, improving the sensitivity does not always improve the SNR. Increasing the optical and mechanical sensitivity does improve the SNR when only optical noise sources are considered. Increasing the optical and mechanical sensitivity does not improve the SNR if only thermo acoustic noise is considered. Consequently, if the noise is dominated by thermal acoustic noise, the only way to improve the SNR is to reduce the noise. Design choices to improve the sensitivity should then only be made if the acoustic noise is not increased, or if it is not the dominant noise type.

5.5. Discussion

A few assumptions have been made that are not in line with the reality. These are discussed separately in the mechanical and optical modelling.

5.5.1. Mechanical modelling

The first and most critical assumption lies within the deformation calculated as pure bending, with plate bending theory. The assumption only holds for small deflections relative to the thickness, without any residual stresses in the material. The assumption of pure bending without residual stress contains risks for the silicon layer because the SOI wafer includes stresses due to its fabrication process. The reason to head on with pure bending is that it is a good first start, and literature is readily available. It serves well to implement a model and compare analytical and numerical results.

Secondly, the equation for the mode shape of the plate vibration assumes an isotropic material. Because the silicon layer of SOI wafers often consists of <100> oriented silicon, the material is anisotropic and the assumption does not hold. However, it suits as a first guess to compare different diaphragm sizes. Solving the equations for anisotropic materials is more complex, and it is recommended to use finite-element software to compute the deformation of anisotropic materials, especially for multiple layers.

5.5.2. Optical modelling

The optical modelling neglects the effect of dispersion by neglecting the wavelength dependency of the effective refractive index. Furthermore, the effect of strain on the effective refractive index is completely neglected. In reality, this is not the case and changes the optical sensitivity. It has already been discussed that the effect of change in the effective index due to strain is expected to account only for a small part of the change in transmission.

Additionally, the assumption of a transmission coefficient $\tau = \sqrt{\alpha}$ is not realistic as the loss and transmission coefficient are difficult to design in such a precise manner. Furthermore, the sensitivity is analytically derived at the steepest slope of the transmission dip. When the wavelength is slightly off this inflexion point, the sensitivity will be less. Therefore, in reality, the optical sensitivity will always be lower than the calculated value.

6 Results

6.1. Mechanical deformation

First, the results of the calculations of the mechanical deformations are presented. The section starts with the analysis of the resonance frequency. Then, the analytical and numerical calculations of the central deflection of the diaphragm at 1 kHz is compared for all the designs. Lastly, the analytical and numerical results for the change in ring radius are presented.

6.1.1. Resonance Frequency design

The first step of any further results is to find the combinations of radius, silicon thickness, and layer thickness that result in a resonance frequency of 25 kHz. The method to do this has been explained in section 5.2 and section 5.3. The results have been separated into three parts: without layer, layered with 100 nm silicon and layered with 150 nm silicon. The results are shown in Figure 6.1. For the design without any layer, the vacuum resonance frequency has been plotted as well. The results indicate a large effect of air on the resonance frequency for small diaphragms. Furthermore, the results are almost identical, which means that the vacuum resonance frequency without any layer is calculated correctly.

The resonance frequency of both the layered structure and the one without any layer are close to the expected 25 kHz. As the radius increases, the layer thickness increases as well and for all the combinations the resonance stays within an acceptable limit. This is a great result because the mechanical deformation due to a sound wave of 1 kHz can now be compared with each other. If the resonance would be different, the stiffness would not be equally compared and require a correction.

Unfortunately, I did not manage to find good results for the PDMS layer. The Young's modulus of PDMS defined in COMSOL is small (750 kPa) compared to the Young's modulus of silicon (170 GPa), which makes it sensitive to errors. Since the value of the Young's modulus of PDMS is much determined by its fabrication process, it is left out of the rest of this thesis. It is recommended to perform experiments regarding the Young's modulus of PDMS before improving the calculation of the resonance frequency.

6.1.2. Central deflection

As discussed in subsection 6.1.1, for each layer material, the values of the layer thickness and radius that result in a resonance frequency of 25 kHz have been solved. The radius is limited to a maximum of 500 μm to ensure that the size of the microphone is not larger than current microphones. For each combination of layer thickness and radius that results in a resonance frequency of 25 kHz, the central deflection of the diaphragm is calculated analytically and numerically in COMSOL at 1 kHz with 1 Pa. The central deflection is used to compute the deflection of the ring later, and the analytical and COMSOL result should be approximately equal to ensure that calculations are correct. The results without layer are shown in Figure 6.2. The deflection is both plotted against the thickness and radius to ensure that both relations can be understood. The layered result with 100 nm silicon is shown in Figure 6.3 and the layered result with 150 nm silicon is shown in Figure 6.4.

The analytical and numerical results of the central deflection are close to identical. This means that for the calculation of the ring radius, and later of the total sensitivity, the central deflection is calculated correctly. A slight difference is seen in the deflection of the design without any layer and a 100 nm thickness of silicon. The result is considered to be in the limit for equal comparison.

6.1.3. Change in ring radius

The change in ring radius is what determines the signal as it results in a change in transmission of the ring resonator. The larger the change, the better. For a silicon thickness of 100 nm and 150

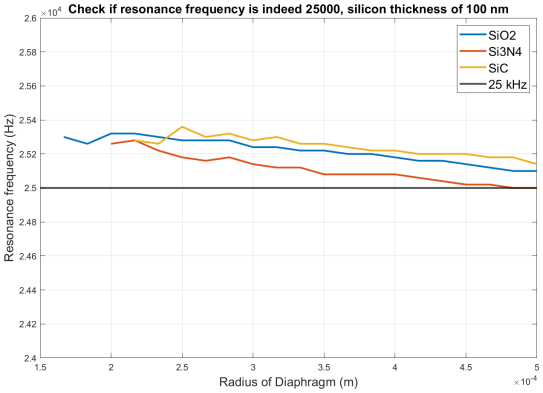

(a) The resonance frequency that is modelled in COMSOL for SiO_2, Si_3N_4, and SiC for a silicon thickness of 100 nm.

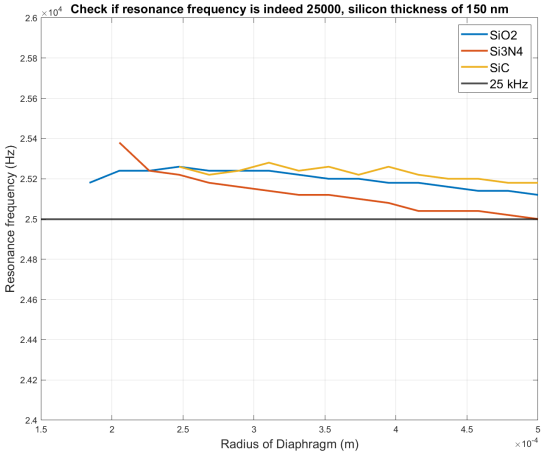

(b) The resonance frequency that is modelled in COMSOL for SiO_2, Si_3N_4, and SiC, for a silicon thickness of 150 nm.

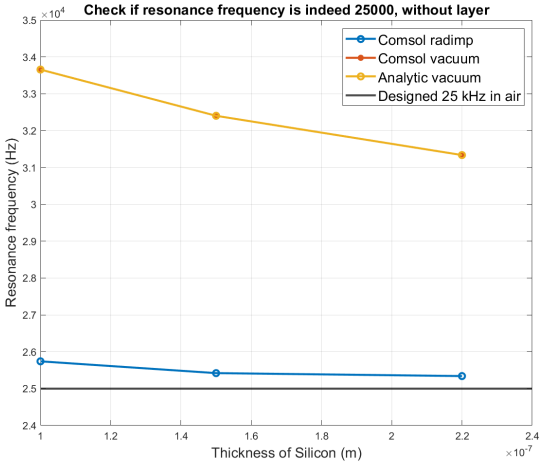

(c) The resonance frequency that is modelled in COMSOL without any layer, for silicon thickness of 100, 150 and 220 nm.

Figure 6.1: The results of the resonance frequency finite element study, where the designed resonance frequency is indicated with a black line at 25 kHz.

nm, the change in ring radius computed both analytically and with COMSOL is shown in Figure 6.5. The minimum layer thickness is set to 150 nm to make sure that the whole ring is covered with the deposited layer. The results of the analytical and COMSOL model are not identical in absolute value but do have a good agreement in the shape. One reason for the difference could be that the assumption of pure bending does not hold perfectly, and the elongation of the neutral axis could result in a different outcome of the result. Another possibility is that the calculation of the curvature, which is the derivative with respect to the central deflection, is not correct in magnitude. One reason could be that for the analytical calculation, the curvature is assumed identical across the cross-section of the diaphragm. In reality, the curvature can be different in the silicon part and the layer part. The fact that the shapes are similar, indicates that the neutral axis calculation should be correct. For a silicon thickness of 100 nm, the change in radius is equal to zero for almost the same thickness of silicon dioxide, which indicates that $z_n = z_r$. Because the shape is similar, the optimum occurs at the same layer thickness or radius. Therefore, the optimum of the design can be found analytically. The next section analyzes the mechanical sensitivity analytically for all the design options.

6.1.4. Mechanical sensitivity

The mechanical sensitivity is defined as the change in ring radius due to sound pressure: db/dP. For each design option, the mechanical sensitivity is analysed in the design space. The results are shown in Figure 6.6. An indication of where the resonance frequency in air is equal to 25 kHz is indicated with a red line, together with a dotted line to specify which part of the design space results in a lower

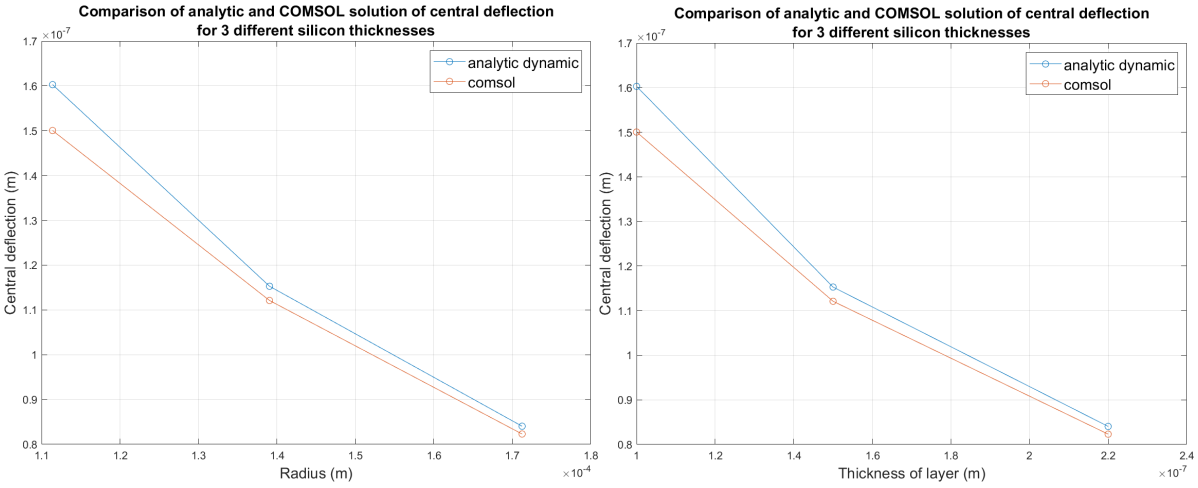

(a) Central deflection without layer, plotted against radius.

(b) Central deflection without layer, plotted against thickness.

Figure 6.2: Comparison of analytical and numerical results without any layer deposition for a pressure of 1 Pa at 1 kHz.

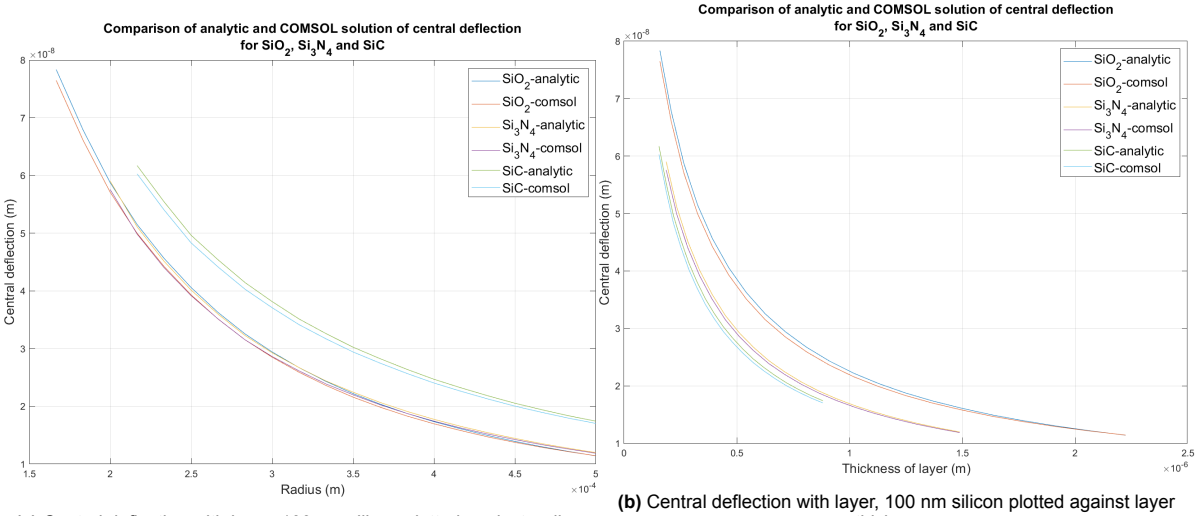

(a) Central deflection with layer, 100 nm silicon plotted against radius.

(b) Central deflection with layer, 100 nm silicon plotted against layer thickness.

Figure 6.3: Comparison of analytical and numerical results with layer deposition, silicon thickness of 100 nm for a pressure of 1 Pa at 1 kHz.

resonance frequency and is therefore not feasible.

The figure is meant to illustrate how the layer thickness and radius influence the mechanical sensitivity. The most interesting result is the effect of the neutral axis. Figure E.1a shows most clearly that a blue horizontal line occurs for a certain layer thickness. As discussed in subsection 5.1.4, the change in ring radius approaches zero when the thickness reaches a point where $z_n = z_r$, resulting in the blue horizontal line.

Additionally, increasing the layer thickness further above the blue horizontal line improves the mechanical sensitivity until a certain point, where the layer thickness increases the stiffness such that it reduces the sensitivity. This trade-off is also clearly visible in the figures (the yellow part above the horizontal blue line).

Furthermore, Figure E.1a clearly shows the higher sensitivity for a thin layer. For all layer materials, a layer thickness of 0 results in the same sensitivity. The absolute value is not indicated clearly because the final design is optimized for SNR, and therefore the values are specified later.

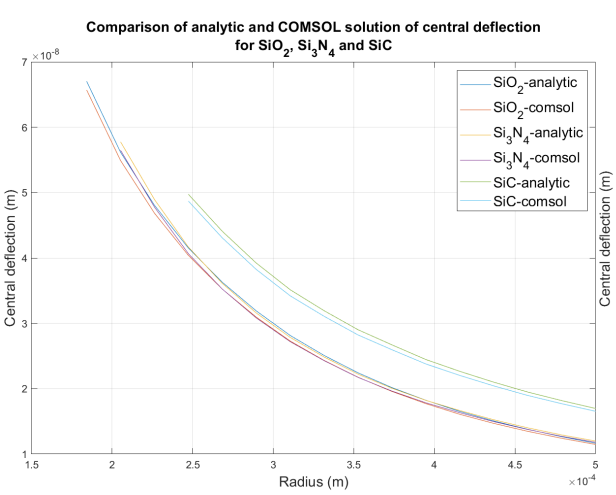

(a) Central deflection with layer, 150 nm silicon plotted against radius.

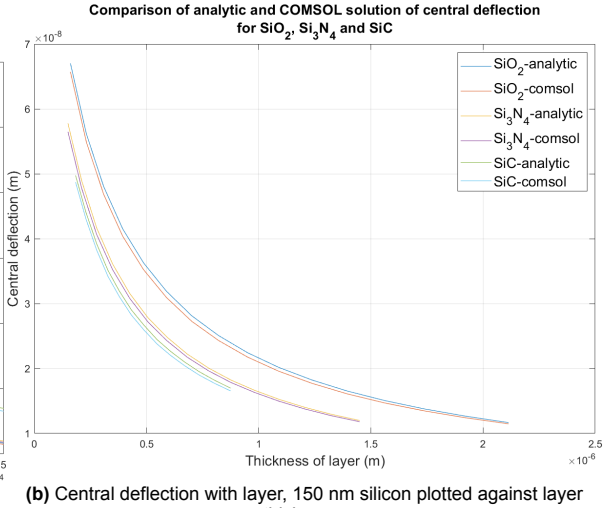

(b) Central deflection with layer, 150 nm silicon plotted against layer thickness.

Figure 6.4: Comparison of analytical and numerical results with layer deposition, silicon thickness of 150 nm for a pressure of 1 Pa at 1 kHz.

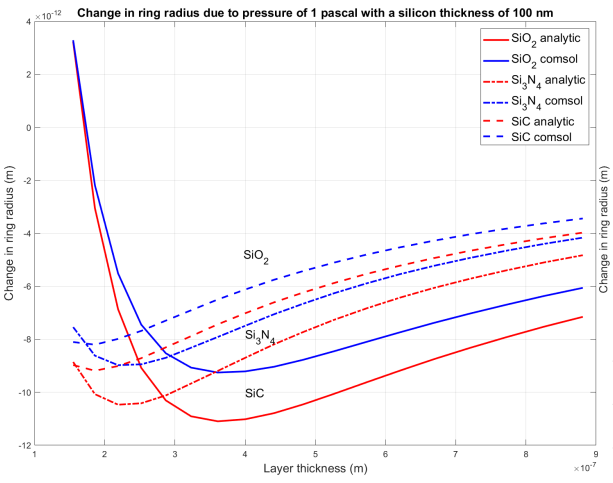

(a) Analytical and numerical outcome of the change in ring radius for each layer material and different layer thicknesses (with f_0 = 25 kHz), with silicon thickness of 100 nm

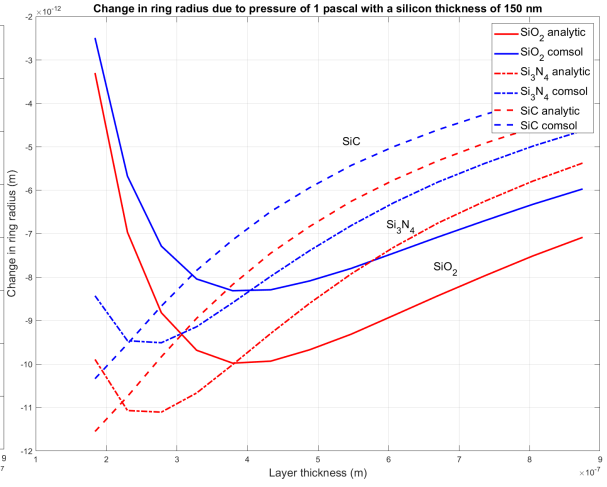

(b) Analytical and numerical outcome of the change in ring radius for each layer material and different layer thicknesses (with f_0 = 25 kHz), with silicon thickness of 100 nm

Figure 6.5: Analytical and numerical result of change in ring radius

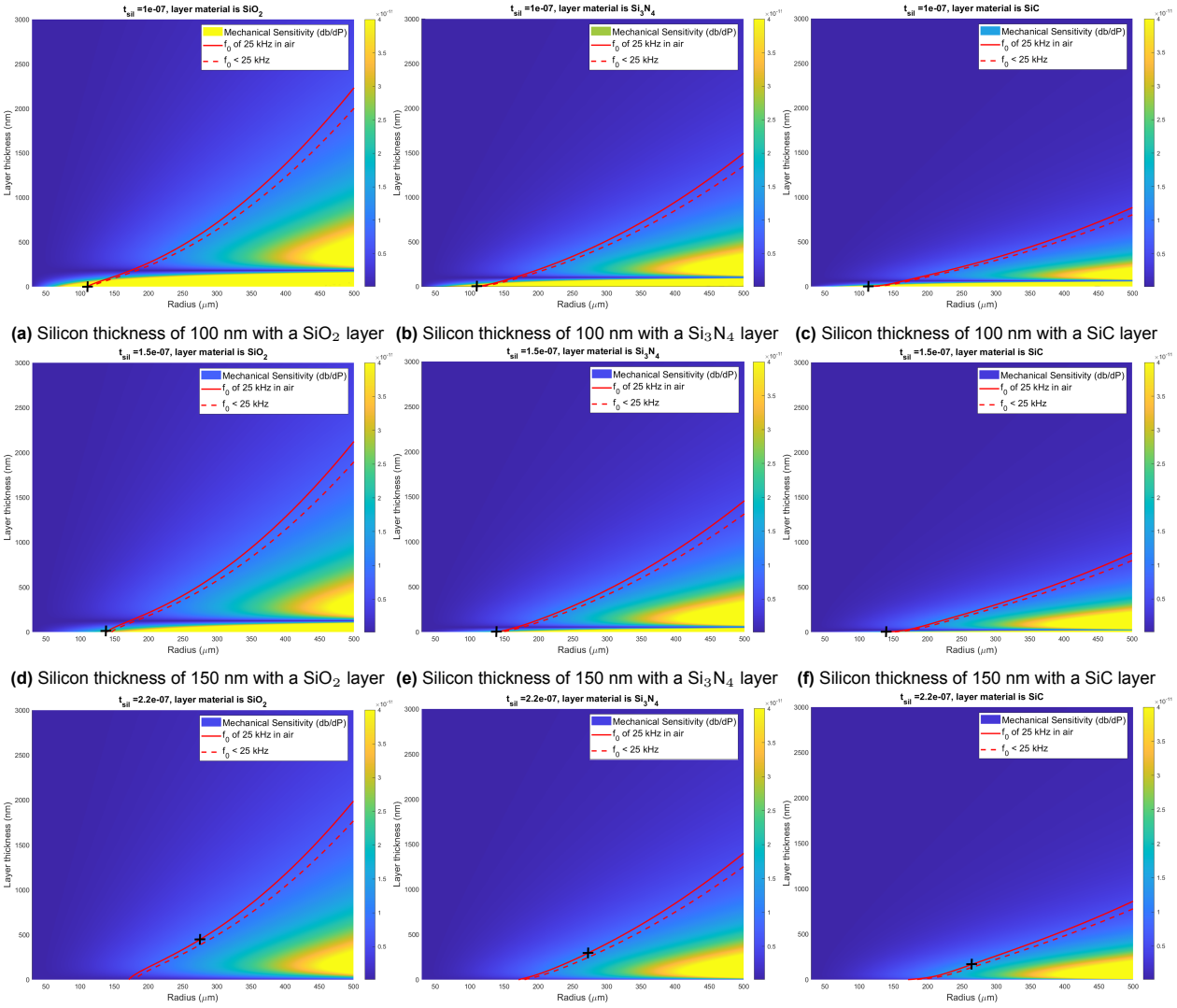

(a) Silicon thickness of 100 nm with a SiO_2 layer **(b)** Silicon thickness of 100 nm with a Si_3N_4 layer **(c)** Silicon thickness of 100 nm with a SiC layer

(d) Silicon thickness of 150 nm with a SiO_2 layer **(e)** Silicon thickness of 150 nm with a Si_3N_4 layer **(f)** Silicon thickness of 150 nm with a SiC layer

(g) Silicon thickness of 220 nm with a SiO_2 layer **(h)** Silicon thickness of 220 nm with a Si_3N_4 layer **(i)** Silicon thickness of 220 nm with a SiC layer

Figure 6.6: Effect of radius and layer thickness on the mechanical sensitivity with an indication of the resonance frequency at 25 kHz. The black cross indicates where the mechanical sensitivity is the highest.

6.2. Optical sensitivity

This section will include the optical sensitivity to quantify the total optomechanical signal. First, the effective refractive index of the first TE mode of the waveguide is calculated for each design option, using an online tool [83]. Then, the effect of the ring location on the sensitivity is discussed. Lastly, the optical sensitivity, defined as dT/db, is calculated for each design option.

6.2.1. Effective index of the waveguide

The different layer materials and different silicon thicknesses have an effect on the effective index of the waveguide. An online app was used to find the values of the effective index of the first TE-mode, see Ref. [83]. A screenshot of what the application looks like is shown in Figure 6.7. The outcome for different layer thicknesses and a silicon thickness next to the ring of 100 and 150 nm is shown in Table 6.1. Since it is possible to have a small section near the waveguide that is either 100 or 150 nm, even though the rest of the silicon layer has a different thickness, the value of the silicon thickness that results in the highest effective index of the mode is chosen, because a higher effective index results in a higher sensitivity.

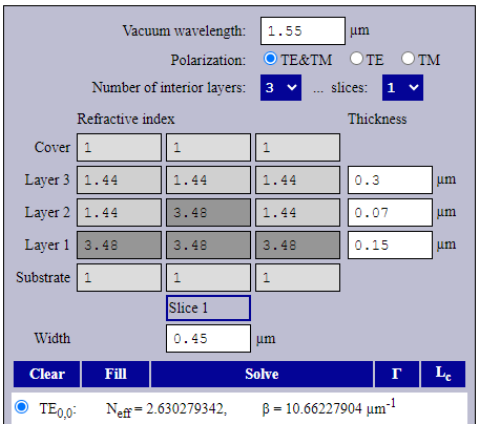

Figure 6.7: Screenshot of the application that is used to determine the effective index for different materials. It allows to enter different waveguide sizes, wavelengths and refractive indices.

6.2.2. Ring location

The ring radius is limited to a minimum of 30 μm, as discussed in chapter 5, subsection 5.4.2. This section studies the effect of the ring location with respect to the radius of the diaphragm, to analyse if the minimum of 30 μm is the right choice. To study it, I considered the effect of ring radius on $\partial w/\partial r$ evaluated at r = b (this neglects the effect of $(z_r - z_n)$). Additionally, I studied $\partial b/\partial P$ (this includes the effect of $(z_r - z_n)$), and the total sensitivity $\partial T/\partial P$ for different ring locations.

The total sensitivity is where the decision is based upon, and is effective by itself. The other graphs are added to gain a full understanding of how each parameter influences the sensitivity. In Figure 6.8a, it can be seen that the curvature $\partial w/\partial r$ of the diaphragm is largest at the centre of the radius.

When the effect of the neutral axis is included, in Figure 6.8b, it can be seen that for the first thickness, the neutral axis of the ring is above the neutral axis of the dual-layered structure (positive values), and for larger thicknesses, the neutral axis of the ring is below the neutral axis of the dual-layered structure (negative values). Furthermore, larger sizes increase the sensitivity db/dP until a certain point, as expected from the analysis in subsection 6.1.4.

The total sensitivity includes the fact that the optical sensitivity $\partial T/\partial b$ scales with 1/b, as discussed in chapter 5, subsection 5.4.2 (Figure 5.10). The normalized result is shown in Figure 6.8c, which indicates that indeed, the highest sensitivity is obtained from a smaller ring, regardless of the other design variables. Consequently, 30 μm is the best choice for design of the ring radius.

6.2.3. Quantification of the optical sensitivity

With the effective indices and ring location determined, it is possible to quantify the optical sensitivity $\partial T/\partial b$ for all design options, which reads as the change in transmission due to a change in ring radius.

Table 6.1: Effective indices for different materials, layer thicknesses and silicon thicknesses.

Layer thickness (μm)	Effective index (100 nm silicon)	Effective index (150 nm silicon)
No Layer (Refractive index air = 1 [75])		
-	2.43	2.60
SiO_2 (Refractive index = 1.44 [75])		
0.05	2.47	2.62
0.1	2.48	2.63
0.15	2.48	2.63
0.3	2.49	2.63
1	2.49	2.63
Si_3N_4 (Refractive index = 2.00 [75])		
0.05	2.56	2.67
0.1	2.57	2.68
0.15	2.58	2.69
0.3	2.59	2.70
1	2.59	2.70
SiC (Refractive index = 2.57 [75])		
0.05	2.66	2.74
0.1	2.70	2.77
0.15	2.72	2.79
0.3	2.74	2.81
1	2.75	2.82

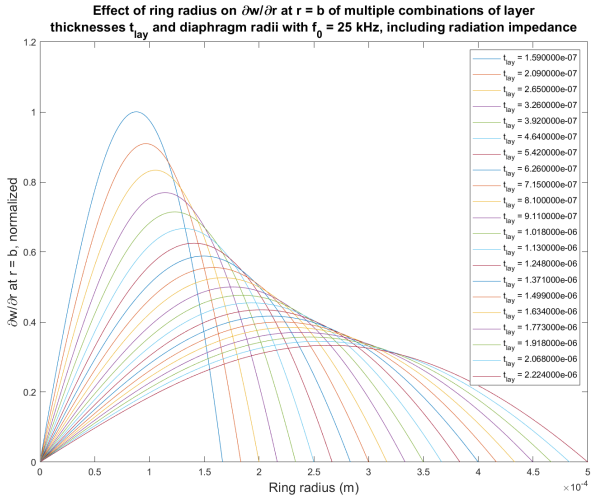

(a) Effect of ring radius on $\partial w/\partial r$ evaluated at r = b.

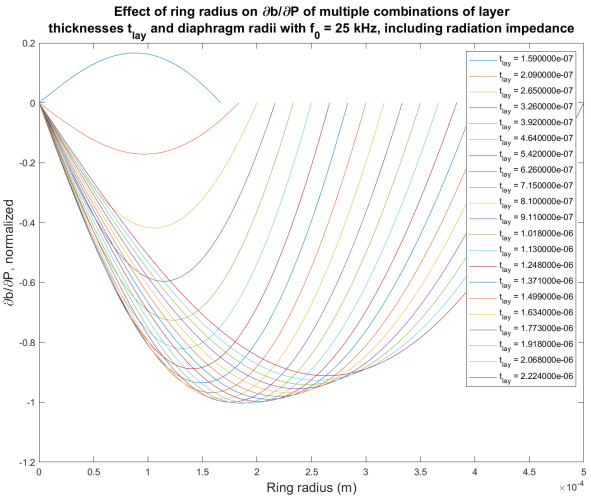

(b) Effect of ring radius on $\partial b/\partial P$.

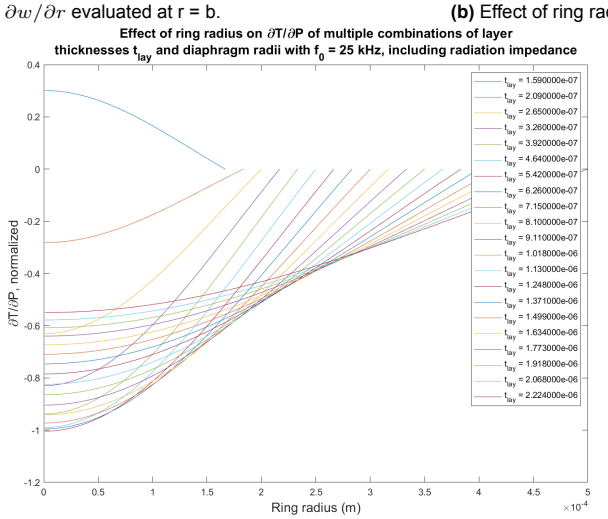

(c) Effect of ring radius on $\partial T/\partial P$.

Figure 6.8: Effect of ring radius on mechanical and optical sensitivity for different designs, silicon thickness of 100 nm and SiO_2 layer.

This is independent of the mechanical behaviour and is solely determined by the optical design. From table Table 6.1 it can be seen that the layer thickness is not significantly changing the effective index, and therefore a value in the middle is chosen for each material. The optical sensitivity can be computed with Equation 5.25 and Equation 5.26:

$$\frac{\partial T}{\partial b} = \frac{\partial T}{\partial \theta}\bigg|_{\theta=\Gamma\sqrt{3}/6} \frac{\partial \theta}{\partial b} = (1 - T_{min})\frac{3\sqrt{3}}{4\Gamma}\frac{4\pi^2}{\lambda}n_e \tag{6.1}$$

The resulting sensitivities are shown in Table 6.2. The waveguide losses were approximated as -3 dB/cm, the transmission coefficient as $\tau = \sqrt{\alpha}$, the ring radius is fixed at 30 μm and the measurement wavelength is 1550 nm.

Table 6.2: Optical sensitivity for different layer materials

Layer Material	Effective Index	$\frac{\partial T}{\partial b}$ $[\frac{1}{m}]$
No Layer	2.60	3.92×10^9
SiO_2	2.63	3.96×10^9
Si_3N_4	2.68	4.04×10^9
SiC	2.75	4.14×10^9

With both the mechanical and optical sensitivity quantified, the optomechanical modelling is finished. The next part discusses the noise to come to the final design, which optimizes the SNR. The results for the optomechanical sensitivity have not been plotted, since the figure is very similar to the mechanical sensitivity (but this time multiplied by the optical sensitivity, which only varies slightly for each material).

6.3. Noise analysis: acoustic thermal noise

Acoustic thermal noise is measured as a pressure fluctuation at the diaphragm. These pressure fluctuations are inevitable and are proportional to the acoustic resistance, as discussed in subsection 4.2.1. The acoustic thermal noise is calculated with the electric circuit model that is presented in subsection 4.2.4. The outcome of the model is the noise spectral density, with unit Pa/$\sqrt{\text{Hz}}$.

The goal is to minimize the acoustic thermal noise to improve the signal-to-noise ratio. The pressure fluctuation amplitude is calculated by multiplying the pressure spectral density with the square root of the bandwidth, which is from 20 to 20000 Hz. The noise spectral density is not constant over the frequency range and the numerical integration is done as:

$$P_{noise} = \sqrt{\sum_{i=1}^{n} \Delta f \text{NSD}_A^2(f_i)} \tag{6.2}$$

where $\text{NSD}_A(f_i)$ is the A-weighted noise spectral density evaluated at frequency f_i; Δf is the frequency range for which the spectral density is considered as constant, and is determined by the size of the numerical integration. P_{noise} is the amplitude of the pressure fluctuations due to acoustic thermal noise. This is used later to derive the SNR. The next section discusses how acoustic noise and resonance frequency are related.

6.3.1. Resonance frequency in noise analysis

The layer thickness and radius of the diaphragm were chosen such that there is a resonance frequency of 25 kHz, which includes the mass-loading effect of the radiation impedance. The resonance frequency is important for the noise consideration because noise amplitude around the resonance frequency is amplified as well [9]. During the analysis of the acoustic noise, there was an observation that for small and thin diaphragms, the resonance frequency was not at 25 kHz, but below that value. It was found that the inductor of the port mass is lowering the resonance frequency. In the Knowles paper, the total shift that is due to the air loading is called mass loading, which includes the effect of the port mass [9]. Kim and Lee mention this effect as well and also describe that the front volume and its mass form a Helmholtz resonance. A Helmholtz resonance is explained in more detail in subsection 2.2.7. For this

thesis, it is uncertain how large the port mass loading effect is and I use the model of references [9] and [12] to include the port mass for the acoustic noise analysis. This means that for small diaphragms designed at 25 kHz with only radiation impedance, the resonance which includes port mass is lower and within the audible frequency. For example, a microphone with a silicon dioxide layer of approximately 160 nm, a silicon layer of 100 nm and a radius of 167 μm has a resonance of only 18.2 kHz with the mass-loading of the port mass included. Whereas the resonance occurs at 25.1 kHz when the port mass is removed from the analysis, which is in line with the desired 25 kHz. The effect of the resonance can be seen in Figure 6.9 and Figure 6.10, where the A-weighted acoustic noise spectral density is shown. Both the external software Simulink and the analytical transfer functions derived in Appendix A were used to compute the result, which validates the correct calculation. The frequency domain is plotted up to 100 kHz to clearly show the effect of the port mass. The next subsection discusses how acoustic noise influences the SNR and also how the port mass influences the SNR.

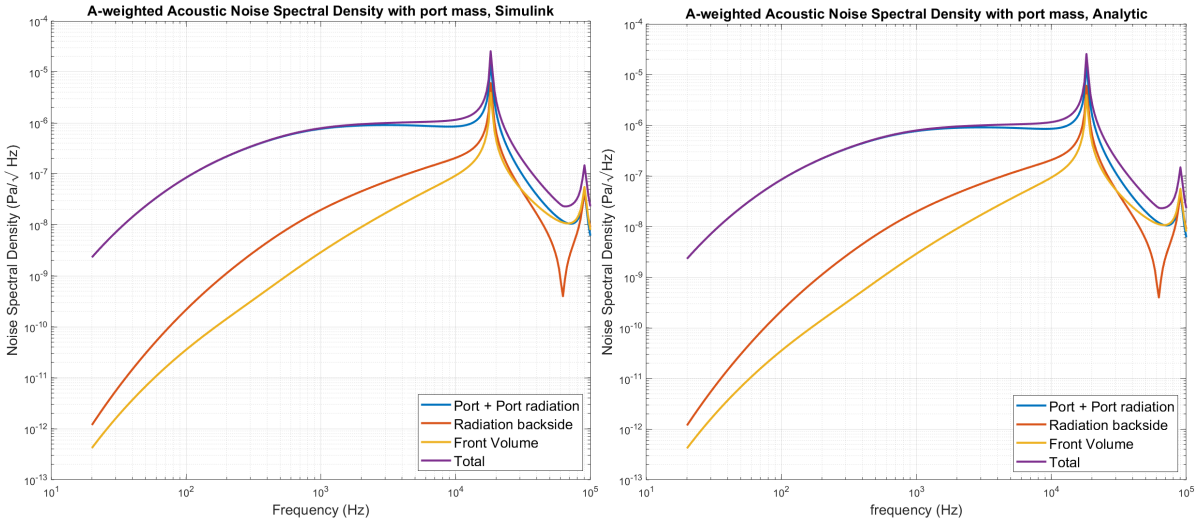

(a) A-weighted pressure noise spectral density computed with Simulink model.

(b) A-weighted pressure noise spectral density computed with analytical transfer functions.

Figure 6.9: A-weighted pressure noise spectral density with a resonance at 18.1 kHz due to the port mass, computed with Simulink and analytically.

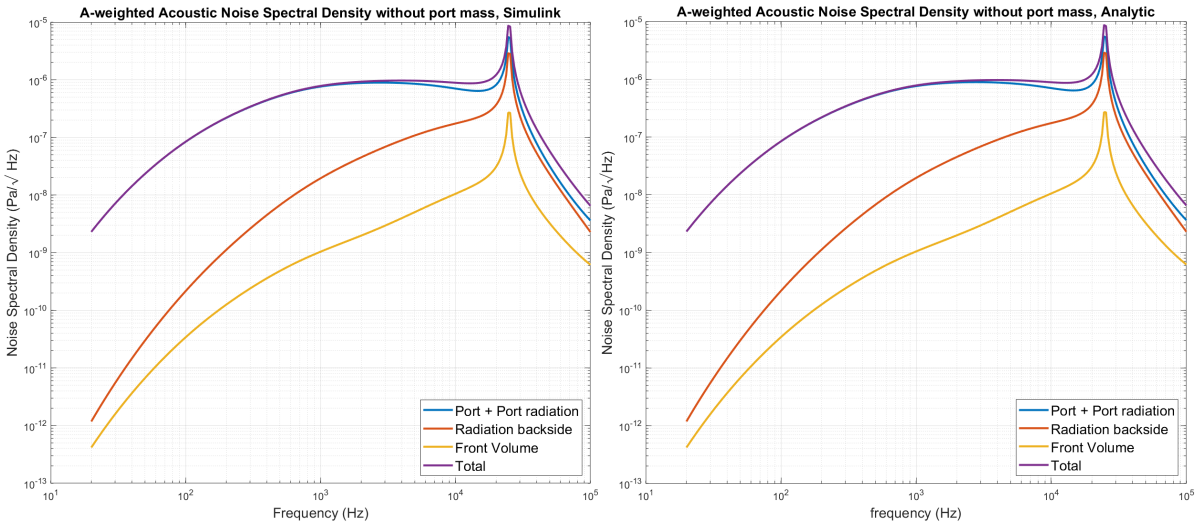

(a) A-weighted pressure noise spectral density computed with Simulink model.

(b) A-weighted pressure noise spectral density computed with analytical transfer functions.

Figure 6.10: A-weighted pressure noise spectral density for the same design, this time without port mass, resulting in a resonance at 25.1 kHz; computed with Simulink and analytically.

6.3.2. Acoustic SNR

The acoustic SNR can be calculated as:

$$\text{SNR}_A = \frac{P_{in}}{P_{noise}} \tag{6.3}$$

with $P_{in} = 1$ for a pressure signal of 1 kHz of 1 pascal. Assuming that other noise types are negligible, and the microphone can perfectly capture pressure levels as small as the noise pressure P_{noise}, this would be the SNR of the microphone. In the microphone industry, the SNR is often presented in dB:

$$\text{SNRdB} = 20\log_{10}(\text{SNR}_A) \tag{6.4}$$

In the example discussed in the previous subsection, with a silicon dioxide layer thickness of 160 nm, a silicon thickness of 100 nm and a radius of 167 μm, the acoustic SNR is equal to 77.6 dB, which is an improvement of 10 dB in comparison with the SNR of the state-of-the-art microphones presented by ref. [9], which shows SNRs up to 67 dB. However, when the port mass is included and the resonance is within the audible bandwidth, the maximum achievable SNR is only 62.3 dB. For larger designs, for example, a silicon dioxide layer of 2.2 μm, and a silicon thickness of 100 nm with a radius of 500 μm results in an acoustic SNR of 82.9 dB, including the port mass. This time, the resonance with port mass reduces from 24.9 kHz to 23.2 kHz.

The examples above show that the port mass is significantly changing the outcome of the acoustic SNR. Therefore, with the current model, smaller diaphragms suffer more from acoustic noise than larger designs. The final design takes this into account by allowing the design to have a larger resonance frequency than 25 kHz. This has a negative effect on the mechanical sensitivity which is approximately proportional to $1/\omega_0^2$. The next section explains in detail how mechanical sensitivity and acoustic thermal noise are both considered to come to a final design.

6.4. Design optimization

With the acoustic noise calculation, the next step is to dive into the design optimization, considering all parameters discussed. In summary, the most important insights or considerations are:

- The only way to improve the acoustic SNR is to reduce the acoustic thermal noise. Increasing the signal by improving the mechanical sensitivity, will also increase the noise amplitude and has no effect on the SNR.
- The smaller and thinner the diaphragm, the larger the mass-loading effect on the resonance frequency.
- The smaller and thinner the diaphragm, the larger the mechanical sensitivity. Thus also (in general) the larger the change in ring radius.
- The neutral axis determines the deflection of the ring. The additional layer can change the neutral axis such that the net deflection of the ring is zero. This can be described as equal elongation and compression of the ring and occurs when $z_n = z_r$.
- The option of 220 nm silicon is therefore not possible without any layer, as it would result in $z_n = z_r$.
- The optical sensitivity is highest for a smaller ring radius b. A limit of 30 μm is set as the minimum and is used to compute the sensitivity.
- The acoustic thermal noise increases quickly when the resonance is within the audible frequency bandwidth. The signal is considered at 1 kHz and is not much affected by a lower resonance.

With these insights and with the verified models, the goal is now to find the best-performing design. This thesis is about improving the SNR; thus, the optimization will be done to achieve the highest SNR. The noise source that has been analysed is acoustic thermal noise. Other noise types have not been studied in depth. Acoustic thermal noise only limits the microphone's SNR when it is the dominant noise source. In other words, the minimum detectable pressure should be below that of the acoustic noise pressure. The minimum detectable pressure is related to optic noise, and requires an analysis of the optical noise, given in the next subsection.

6.4.1. Optical noise

Both the laser and photodetector include noise sources. To quantify the noise, I searched for both a laser and a photodiode online. Koheron fabricates low-noise lasers and photodiodes suitable for 1550 nm, which I used as a reference [84] [85]. The laser intensity noise is shown in Figure 6.11. The highest sample rate that is commonly found in microphones is 192 kHz, which allows for almost 10 samples per wavelength up to 20 kHz, to correctly capture the amplitude of audible signals. It is uncertain which amount of current will be used, but a value of -140 dBc/Hz is safe to consider as laser-intensity noise. The unit dBc is relative to the carrier signal. Multiplied with a bandwidth of 192 kHz, this results in -87 dBc intensity noise of the laser. The bandwidth is considered up to the measurement bandwidth, which is possible if higher frequencies are filtered, according to Ref. [86]. Next, the photodiode is analysed.

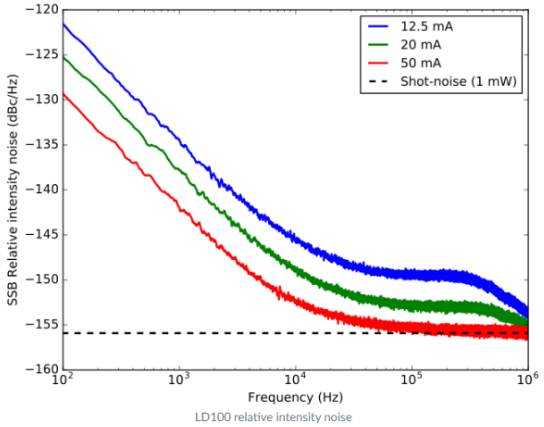

Figure 6.11: Relative intensity noise for different currents (30 mA = 3 mW laser intensity) [84].

The specifications of the photodiode specify an input current noise density of $9pA/\sqrt{Hz}$ and a peak responsivity of $0.9A/W$ [85]. Furthermore, the power density and noise equivalent power are shown in Figure 6.12. The SNR of the photodiode is now computed as the power density times the bandwidth, divided by the noise equivalent power times the square root of the bandwidth. This results in 106 dB SNR. Multiplying the noise current with the square root of the bandwidth and comparing it with the signal of 1 mW multiplied with the responsivity, results in an SNR of 107 dB. Therefore, the method is assumed as correct. One note that should be made is that SNR in dB is either computed as $dB = 20\log_{10}(Mag)$ or as $dB = 10\log_{10}(Mag)$. The 20 comes from a squared signal/noise, which is often used to find the power value. I know that for the microphones of 67 dB, the values are computed with $dB = 20\log_{10}(Mag)$ which is used for pressure comparison in general. To compare both values, the SNR of the photodiode is computed with $dB = 20\log_{10}(Mag)$ as well.

6.4.2. Optimization problem

With an estimation of the acoustic noise, optical noise and mechanical sensitivity it is possible to find an optimal design that results in the highest SNR. To do so, the following approach is used:

1. Define the silicon thickness and layer material with its properties.
2. Define the waveguide loss (-3 dB/cm) and ring radius (30 μm).
3. Define the effective index based on the layer material.
4. Define the input pressure and the evaluated frequency.
5. Define the design space as 30 μm $\leq$ a $\leq$ 500 μm and $t_{lay} \leq 3$ μm.
6. Indicate where in the design space the resonance frequency is equal to 25 kHz, which considers radiation impedance.
7. Compute dT/db for all options in the design space and layer materials.
8. Compute the acoustic thermal noise P_{noise} for all options in the design space and layer materials.
9. Compute the mechanical sensitivity db/dP for all options in the design space and layer materials.
10. Calculate the acoustic noise as P_{noise} times dT/dP times the original signal (1 mW).

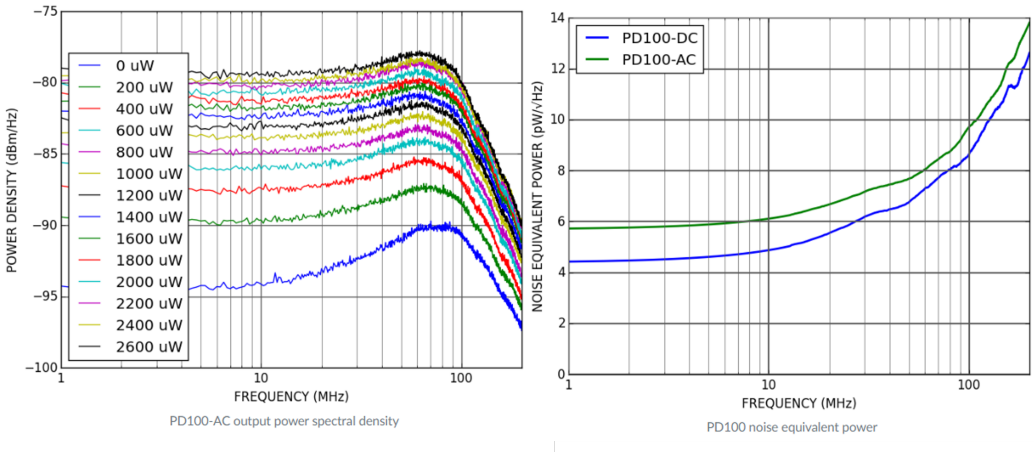

Figure 6.12: Power density and noise equivalent power of AC photodiode [85].

11. Calculate the laser intensity noise as -87 dB ($10^{-8.7}$ in this case) times the original signal and add photodetector noise as -106 dB ($10^{-5.3}$ in this case) times the original signal.
12. Calculate the signal as dT/dP times the original signal at 1 pascal.
13. Calculate the SNR as the signal divided by the total noise.
14. Indicate where the acoustic noise is larger than the optical noise.
15. Find the optimum combination of layer thickness and radius which results in the highest SNR

With three silicon thickness options and three layer material options, this leads to a total of 9 different results. Each option has its own optimum design in terms of radius and layer thickness. For the first option, a silicon thickness of 100 nm and a SiO_2 layer, the result is shown in Figure 6.13. For the other options, the results are shown in Appendix E. The figure is not easy to read and needs explanation. In yellow/green, the contours of different values of the SNR in dB are shown, which should be as high as possible. The red line indicates where the resonance frequency is 25 kHz. The red dashed line indicates the infeasible direction, so any design option on the right side of the red line is not considered. The black line indicates where the optical noise is equal to the acoustic noise. This means that the minimum detectable pressure is equal to the acoustic noise. The dashed black line indicates in which direction the optical noise becomes larger. The main reason for a higher optical noise level in comparison with acoustic noise is that the mechanical sensitivity is not high enough to detect the small acoustic noise pressure. Therefore, it is undesired to have optical noise dominating the noise floor. The blue cross indicates where in the design space the SNR is the highest.

It can be seen that close to the resonance frequency, the SNR quickly drops. This has to do with the fact that the port mass in the acoustic analysis lowers the resonance such that noise is amplified by the resonance. Therefore, the best design is a little away from 25 kHz. It is uncertain how much the effect of the port mass will be in reality, but for robustness, it is advised to consider a resonance above 25 kHz.

The results of all the different options are shown in Table 6.3. The highest SNR is for a silicon thickness of 220 nm in combination with a silicon carbide layer. However, it can be seen that the SNRs of the other options are close to each other and finding the best option requires some more attention. The mechanical sensitivity and the acoustic noise are presented for each design as well. Since the optic noise analysis can be wrong, it is desired to have a high mechanical sensitivity. Furthermore, the acoustic noise pressure should be as low as possible, since this limits the microphone even with perfect optical components. The mechanical sensitivity is also the highest for a silicon thickness of 220 nm with a SiC layer. It is possible to consider the option of a silicon thickness of 100 nm with a SiO_2 layer as well since the SNR is high and the sensitivity too. Additionally, the acoustic noise is lower which can result in a better SNR when the optical noise turns out to be lower than expected. Also, the silicon dioxide layer requires a thicker layer for resonance at 25 kHz, and as a consequence, it is less sensitive to fabrication errors. Another reason for the silicon dioxide layer is that the silicon thickness is less than 220 nm. A thickness of 220 nm around the waveguides is not possible and a local etch

around the waveguide is required to form a RIB waveguide. It is unknown how wide the etching should be for proper guidance of the mode, and the 100 nm option does not have these complications. Since my thesis is mostly about indicating trade-offs and studying the effect of the design parameters, the final design includes both options as advice, discussed in the next section.

Table 6.3: Results of design optimization for each design option

Silicon Thickness (nm)	Layer Material	Radius (μm)	Layer Thickness (nm)	SNR (dB)	dT/dP	P_{noise} (μPa)
100	SiO_2	305	810	73.5	0.0384	84.2
100	Si_3Ni_4	272	455	72.8	0.0353	91.6
100	SiC	295	370	71.4	0.0257	77.9
150	SiO_2	310	760	73.0	0.0350	84.0
150	Si_3Ni_4	268	395	73.0	0.0376	93.1
150	SiC	254	240	73.0	0.0377	95.4
220	SiO_2	310	675	72.6	0.0323	84.9
220	Si_3Ni_4	272	345	73.3	0.0385	90.1
220	SiC	254	195	73.8	0.044	92.1

6.5. Final Design

The final design actually consists of two design options that can be considered. The difference in outcome is not significant enough to present one option as the best option. The first option consists of a 220 nm silicon thickness with a silicon carbide layer of 195 nm, with a radius of 254 μm. The second option consists of a 100 nm silicon thickness with a silicon dioxide layer of 810 nm, with a radius of 305 μm. For both options, the analytical result has been compared to the result obtained in COMSOL. These results are shown in Table 6.4.

Table 6.4: Comparison between COMSOL and analytic result of different values for design 1 and 2.

Design	Silicon Thickness	Layer Material	Radius	Layer Thickness
1	220 nm	SiC	252 μm	185 nm
2	100 nm	SiO_2	305 μm	810 nm
Design	**db** Analytic	**db** COMSOL	$\mathbf{w}_0$ Analytic	$\mathbf{w}_0$ COMSOL
1	10.5×10^{-12} m	9.1×10^{-12} m	0.31×10^{-7} m	0.30×10^{-7} m
2	9.7×10^{-12} m	8.1×10^{-12} m	0.23×10^{-7} m	0.22×10^{-7} m
Design	SNR Analytic	SNR COMSOL	$\mathbf{f}_0$ Analytic	$\mathbf{f}_0$ COMSOL
1	73.8 dB	73.1 dB	29.7 kHz	30.0 kHz
2	73.5 dB	72.5 dB	27.0 kHz	27.3 kHz

In the table, **db** is the change in ring radius due to 1 Pa at 1 kHz, w_0 is the central deflection of the diaphragm, and f_0 is the resonance frequency in air, considering only radiation impedance. The result leads to an improvement of 6 dB SNR compared with current MEMS microphones, see Ref. [9], table 10.

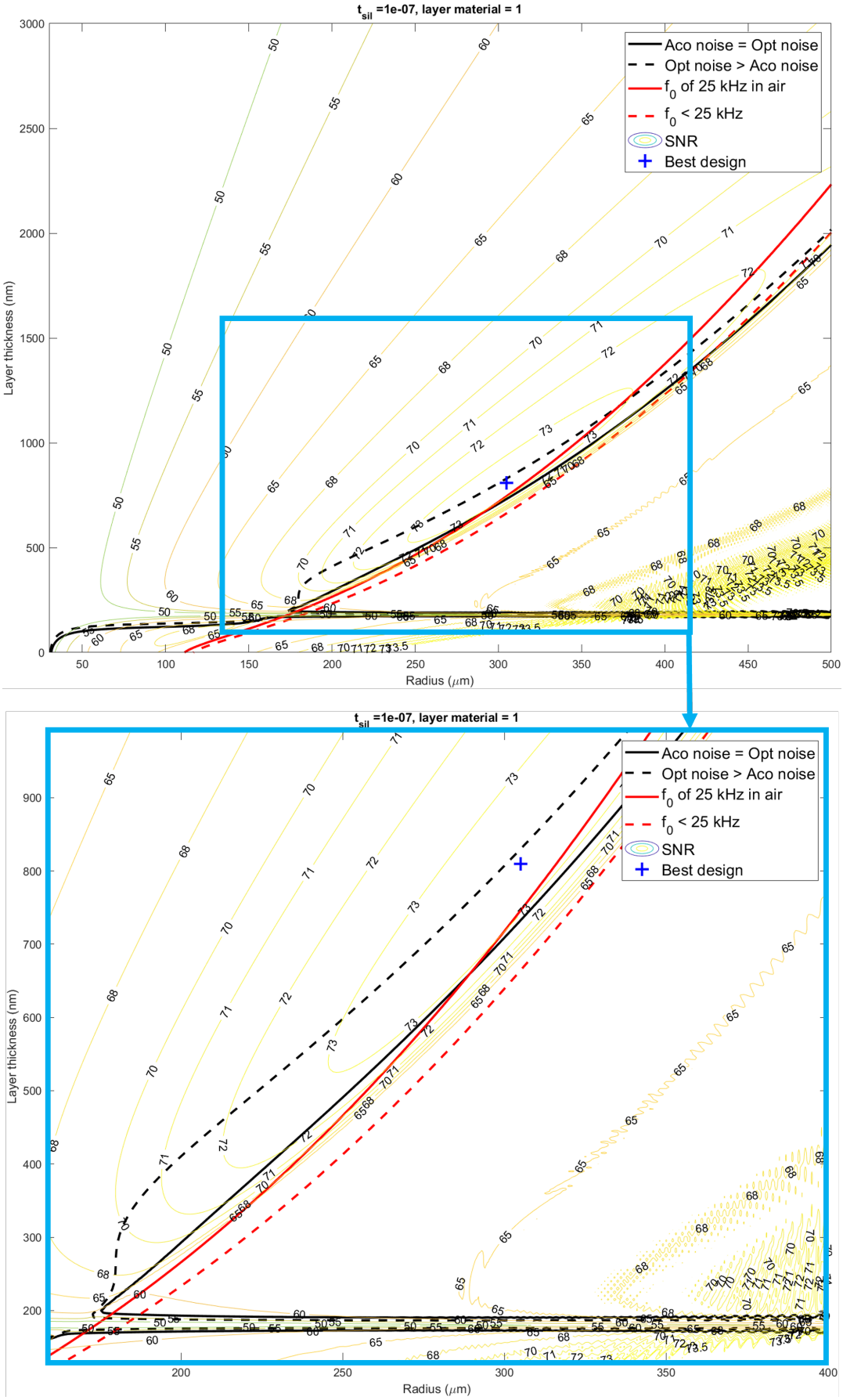

Figure 6.13: Contour figure of the SNR in dB for the design space with a silicon thickness of 100 nm and a SiO_2 layer. A red line marks the design space that results in a resonance frequency of 25 kHz in air, with the infeasible domain indicated by the red dotted line. A black line indicates where optical noise is equal to acoustic noise, the dotted black line indicates where the optical noise is larger.

7 Discussion & Recommendations

The improvement of the SNR of current state-of-the-art microphones is a great result, however, there are several key aspects that have to be discussed regarding the result. After the discussion, the knowledge gained during this thesis is used to provide a recommendation for future research. The discussion also restates crucial points covered in the individual chapters to ensure a complete and comprehensive understanding.

7.1. Discussion

The primary point of discussion lies in the calculations of mechanical deformation. It is important to note that the current models lack the consideration of any residual stresses in the material and do not incorporate membrane modelling, which is only valid for small displacements relative to the thickness. Nonetheless, since the central deflection is less than a 10th of the total thickness for the final two design options, the use of plate theory can be justified.

However, it is crucial to address the impact of residual stresses in the silicon layer, as they can significantly influence the results. The presence of pretension in the silicon layer can lead to an increase in effective stiffness, potentially resulting in a much higher actual resonance frequency than predicted. Therefore, it becomes necessary to account for this additional pretension in the silicon layer to obtain more accurate and reliable results.

Overall, by considering the effects of residual stresses in the material and incorporating them into the analysis, the models can be enhanced to provide a better understanding of the mechanical deformation and predict the actual resonance frequency more effectively.

The second point of discussion pertains to the calculation of acoustic noise. The model used in this analysis is directly derived from the Knowles paper, which incorporates a smaller port radius for the PCB. It remains uncertain whether the Hagen-Poiseuille equation is still applicable for determining the port resistance when the bottom etch is used to determine the port dimensions. Additionally, there is uncertainty regarding the effect of additional mass-loading on the port. Currently, the addition of the port mass results in final designs with resonances at 27.3 and 30.0 kHz, instead of the expected 25 kHz.

Without the mass-loading of the port, the prominence of the acoustic noise is expected to be reduced, leading to a final result with a resonance closer to the target frequency of 25 kHz.

In conclusion, resolving the uncertainties related to port dimensions and mass-loading effects is crucial for accurately calculating acoustic noise and achieving a resonance frequency closer to the desired 25 kHz, thereby enhancing the overall performance of the system.

Thirdly, it is important to note that the calculation of optical noise remains unverified. The data used in the analysis is sourced from a commercial website, and no experimental validation has been conducted to validate these results. Furthermore, there is a lack of scientific references to support the findings. However, including optical noise in the optimization problem is essential to ensure that the SNR accounts for more than just acoustic noise. Exclusively optimizing for acoustic noise, given a signal of 1 Pa at 1 kHz, could potentially overlook the mechanical sensitivity, which is a crucial aspect of the problem. By considering optical noise, the impact of each individual element on the SNR can be better understood, and it provides insights into various trade-offs that arise in optimizing the SNR of a silicon photonic microphone.

Lastly, it's worth mentioning that the obtained results are based on a laboratory setup, which offers several advantages over the referred state-of-the-art MEMS microphones. Primarily, the laser and photodetector are not integrated within the device, making it challenging to perform a direct comparison

with a fully integrated MEMS microphone. Additionally, by excluding the back volume and ventilation hole from the model, the acoustic noise pressure is reduced, further favouring the silicon photonic microphone in comparison.

In conclusion, while the thesis does have some limitations and unverified aspects, it provides valuable insights that lead to a final recommendation for the design of a silicon photonic microphone.

7.2. Recommendation

If my thesis were perfect, I would recommend directly implementing the results and fabricating the two designs presented in section 6.5:

1. Silicon thickness of 220 nm with a SiC layer of 195 nm, with a radius of 254 μm.
2. Silicon thickness of 100 nm with a SiO_2 layer of 810 nm, with a radius of 305 μm.

However, for the fabrication of a silicon photonic microphone, I suggest the following approach:

7.2.1. Layer deposition

Extend the calculations by incorporating residual stresses in both the silicon and deposited layer. Begin with both numerical and analytical calculations of the resonance frequency in vacuum for only the silicon layer. Then, add the additional layer to the calculations using numerical finite element methods to save time. Study the actual stresses and material properties of each layer material. Additionally, investigate the fabrication error of the deposition process and incorporate it into the calculations. Consider how different designs may be affected by fabrication errors; smaller designs may suffer more, potentially impacting the resonance frequency. Avoid any design that results in a resonance frequency within the audible spectrum, to guarantee the required flat frequency response over the audible frequency spectrum.

7.2.2. Neutral axis

An interesting result from my thesis is the observation that the net radial displacement of the ring goes to zero when the neutral axis of the ring and the diaphragm are equal. It is recommended to verify that any proposed design does not have the neutral axis of the ring too close to the neutral axis of the diaphragm. Testing a diaphragm with a 220 nm silicon thickness before depositing an additional layer can determine if the signal is indeed very small due to the equal neutral axes.

7.2.3. Acoustic noise consideration

Acoustic noise is a significant aspect of this thesis, as a key improvement of a silicon photonic microphone compared to current MEMS microphones is the elimination of thermal acoustic noise originating from the backplate. To enhance the calculation, the port impedance for different geometries should be calculated numerically. The COMSOL thermoviscous acoustics module can be utilized for this purpose, as previously done for the backplate and back volume of a MEMS microphone (see chapter 2,subsection 2.2.9, Figure 2.10). Additionally, verify the appropriate method of adding this impedance to the lumped element model, considering that the current port lumped elements are designed for a geometry with a smaller PCB radius (see Figure 3.8, chapter 3).

Given that the PCB hole radius presented in Ref. [9] is only 175 μm, and no significant port impedances are reported, I recommend prioritizing the focus on mechanical sensitivity rather than reducing acoustic noise. Nevertheless, an accessible and interesting option to reduce the port impedance, without necessarily quantifying the improvement, is to create an angle during the bottom etch. Partially anisotropic etching can lead to such an angle, depending on the etching material and the etched material [87]. An illustration of this concept is shown in Figure 7.1.

In conclusion, by following these recommendations, a more refined and optimized design for a silicon photonic microphone can be achieved, with enhanced mechanical sensitivity and potential tradeoffs to consider in optimizing the SNR.

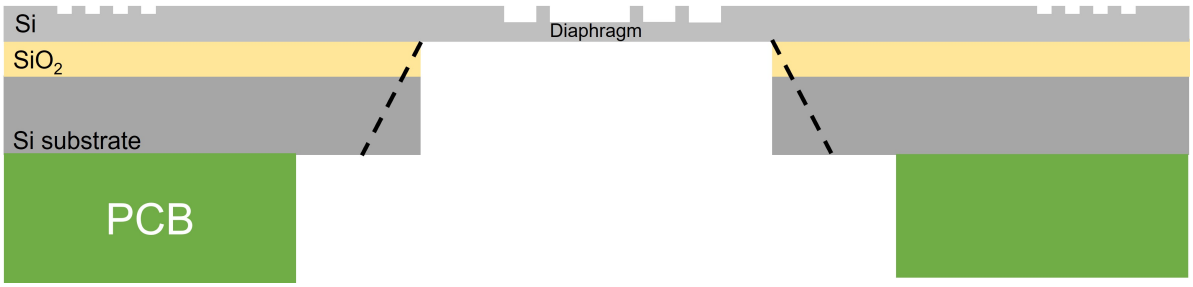

Figure 7.1: Recommendation of the bottom port design.

8 Conclusion

The optomechanical sensitivity of a new type of miniature microphone, a silicon photonic microphone, has been studied for a design space of 3 layer materials (SiO_2, Si_3N_4, SiC) and 3 silicon thicknesses (100 nm, 150 nm, 220 nm), with a limit on the diaphragm radius of 500 μm and a minimum ring radius of 30 μm. Additionally, the thermal acoustic noise has been quantified for all the design options. These were calculated with an analytical derivation of the transfer functions of the acoustic lumped element circuit, allowing for an extensive comparison between different design options by means of an optimization problem. Furthermore, the optical noise sources were presented and quantified for a commercially available laser and photodetector. The optimized SNR of two different designs were presented as the final result of this thesis. The results indicate a potential SNR of 73.1 and 72.5 dB, which is roughly 5 dB more than state-of-the-art MEMS microphones.

References

[1] M. Fueldner, “Microphones,” in *Handbook of Silicon Based MEMS Materials and Technologies*, Elsevier, Jan. 2020, pp. 937–948. DOI: 10.1016/B978-0-12-817786-0.00048-7.

[2] K. Kinoshita, T. Ochiai, M. Delcroix, and T. Nakatani, “Improving Noise Robust Automatic Speech Recognition with Single-Channel Time-Domain Enhancement Network,” *ICASSP, IEEE International Conference on Acoustics, Speech and Signal Processing - Proceedings*, vol. 2020-May, pp. 7009–7013, May 2020. DOI: 10.1109/ICASSP40776.2020.9053266.

[3] B. Gygi and D. Ann Hall, “Background sounds and hearing-aid users: A scoping review,” *International Journal of Audiology*, vol. 55, no. 1, pp. 1–10, Jan. 2016. DOI: 10.3109/14992027.2015.1072773/SUPPL{_}FILE/IIJA{_}A{_}1072773{_}SM9426.DOCX. [Online]. Available: https://www.tandfonline.com/doi/abs/10.3109/14992027.2015.1072773.

[4] D. Lelic, J. Nielsen, D. Parker, and F. Marchman Rønne, “Critical hearing experiences manifest differently across individuals: insights from hearing aid data captured in real-life moments,” *International Journal of Audiology*, vol. 61, no. 5, pp. 428–436, 2022. DOI: 10.1080/14992027.2021.1933621/SUPPL{_}FILE/IIJA{_}A{_}1933621{_}SM3905.DOCX. [Online]. Available: https://www.tandfonline.com/doi/abs/10.1080/14992027.2021.1933621.

[5] Yole Development, “Acoustic MEMS and Audio Solutions,” Tech. Rep., 2017.

[6] P. Scheeper, A. van der Donkb, W Olthuis, and P Bergveld, “A review of silicon microphones,” *Sensors and Actuators A*, vol. 44, pp. 1–11, 1994.

[7] A. Kumar *et al.*, “Recent development and futuristic applications of MEMS based piezoelectric microphones,” *Sensors and Actuators A: Physical*, vol. 347, p. 113 887, Nov. 2022. DOI: 10.1016/J.SNA.2022.113887.

[8] S. A. Zawawi, A. A. Hamzah, B. Y. Majlis, and F. Mohd-Yasin, *A review of MEMS capacitive microphones*, May 2020. DOI: 10.3390/MI11050484.

[9] S. Shubham *et al.*, “A Novel MEMS Capacitive Microphone with Semiconstrained Diaphragm Supported with Center and Peripheral Backplate Protrusions,” 2021. DOI: 10.3390/mi13010022.

[10] Mikko Suvanto, *The MEMS Microphone Book*, 1st edition. Momosic Oy, 2021.

[11] A. Dehé, M. Wurzer, M. Füldner, and U. Krumbein, “The Infineon Silicon MEMS Microphone,” AMA Service GmbH, Dec. 2013, pp. 95–99. DOI: 10.5162/sensor2013/a4.3.

[12] M. L. Kuntzman *et al.*, “Thermal boundary layer limitations on the performance of micromachined microphonesa),” *The Journal of the Acoustical Society of America*, vol. 144, no. 5, p. 2838, Nov. 2018. DOI: 10.1121/1.5070155.

[13] S.-C. Lo *et al.*, *Development of a no-back-plate SOI MEMS condenser microphone; Development of a no-back-plate SOI MEMS condenser microphone*. 2015. DOI: 10.1109/TRANSDUCERS.2015.7181115.

[14] W. J. Mao, C. L. Cheng, S. C. Lo, Y. S. Chen, and W. Fang, “Design and implementation of a CMOS-MEMS microphone without the back-plate,” *TRANSDUCERS 2017 - 19th International Conference on Solid-State Sensors, Actuators and Microsystems*, pp. 1037–1040, Jul. 2017. DOI: 10.1109/TRANSDUCERS.2017.7994229.

[15] Z. Wang, Q. Zou, Q. Song, and J. Tao, “The era of silicon MEMS microphone and look beyond,” *2015 Transducers - 2015 18th International Conference on Solid-State Sensors, Actuators and Microsystems, TRANSDUCERS 2015*, pp. 375–378, Aug. 2015. DOI: 10.1109/TRANSDUCERS.2015.7180939.

[16] B. H. Kim and H. S. Lee, “Acoustical-thermal noise in a capacitive MEMS microphone,” *IEEE Sensors Journal*, vol. 15, no. 12, pp. 6853–6860, Dec. 2015. DOI: 10.1109/JSEN.2015.2464372.

[17] L. Sant *et al.*, “A 130dB SPL 72dB SNR MEMS Microphone Using a Sealed-Dual Membrane Transducer and a Power-Scaling Read-Out ASIC,” *IEEE Sensors Journal*, vol. 22, no. 8, pp. 7825–7833, Apr. 2022. DOI: 10.1109/JSEN.2022.3154446.

[18] N. Bilaniuk, “Optical microphone transduction techniques,” *Applied Acoustics*, vol. 50, no. 1, pp. 35–63, Jan. 1997. DOI: 10.1016/S0003-682X(96)00034-5.

[19] N. A. Hall *et al.*, “Micromachined microphones with diffraction-based optical displacement detection,” *The Journal of the Acoustical Society of America*, vol. 118, no. 5, pp. 3000–3009, Nov. 2005. DOI: 10.1121/1.2062429.

[20] M. L. Kuntzman, C. T. Garcia, A. G. Onaran, B. Avenson, K. D. Kirk, and N. A. Hall, “Performance and modeling of a fully packaged micromachined optical microphone,” *Journal of Microelectromechanical Systems*, vol. 20, no. 4, pp. 828–833, Aug. 2011. DOI: 10.1109/JMEMS.2011.2148164.

[21] Infineon Technologies, *MEMS microphones for consumer*, 2022. [Online]. Available: https://www.infineon.com/cms/en/product/sensor/mems-microphones/mems-microphones-for-consumer/?gclid=Cj0KCQiA7bucBhCeARIsAIOwr-_O-I-xLa5dZrcjFXTvuyNYKx0eUNjUJbfpCJMRELE7cPKSisXxeqMaAvfVEALw_wcB&gclsrc=aw.ds#!products.

[22] D. Kim and N. A. Hall, “Towards a sub 15-dBA optical micromachined microphone,” *The Journal of the Acoustical Society of America*, vol. 135, no. 5, p. 2664, May 2014. DOI: 10.1121/1.4871181.

[23] Apple Inc., *Method of detecting sound using a micro-electro-mechanical system optical microphone*, 2017.

[24] Apple Inc., *Open top back plate optical microphone*, 2017.

[25] C. Zhou, S. V. Letcher, and A. Shukla, “Fiber-optic microphone based on a combination of Fabry-Perot interferometry and intensity modulation,” *Citation: The Journal of the Acoustical Society of America*, vol. 98, p. 1042, 1995. DOI: 10.1121/1.413669.

[26] X. Lu, Y. Wu, Y. Gong, and Y. Rao, “A miniature fiber-optic microphone based on an annular corrugated MEMS diaphragm,” *Journal of Lightwave Technology*, vol. 36, no. 22, pp. 5224–5229, Nov. 2018. DOI: 10.1109/JLT.2018.2868964.

[27] B. Liu *et al.*, “An Optical Fiber Fabry-Perot Microphone Based on Corrugated Silver Diaphragm,” *IEEE Transactions on Instrumentation and Measurement*, vol. 67, no. 8, pp. 1994–2000, Aug. 2018. DOI: 10.1109/TIM.2018.2809840.

[28] W. J. Westerveld and P. H. Urbach, *Silicon Photonics - Electromagnetic Theory*. Bristol, UK: IOP Publishing, 2017.

[29] B. Jalali and S. Fathpour, *Silicon photonics*, 2006. DOI: 10.1109/JLT.2006.885782.

[30] V. Rochus *et al.*, “Design of a MZI Micro-Opto-Mechanical Pressure Sensor for a SiN photonics platform,” *2016 17th International Conference on Thermal, Mechanical and Multi-Physics Simulation and Experiments in Microelectronics and Microsystems, EuroSimE 2016*, Apr. 2016. DOI: 10.1109/EUROSIME.2016.7463357.

[31] B. Troia *et al.*, “Coupled multiphysics circuital modelling of micro-opto-mechanical pressure sensor systems,” *https://doi-org.tudelft.idm.oclc.org/10.1117/12.2290361*, vol. 10545, pp. 297–306, Feb. 2018. DOI: 10.1117/12.2290361. [Online]. Available: https://www-spiedigitallibrary-org.tudelft.idm.oclc.org/conference-proceedings-of-spie/10545/1054518/Coupled-multiphysics-circuital-modelling-of-micro-opto-mechanical-pressure-sensor/10.1117/12.2290361.fullhttps://www-spiedigitallibrary-org.tudelft.idm.oclc.org/conference-proceedings-of-spie/10545/1054518/Coupled-multiphysics-circuital-modelling-of-micro-opto-mechanical-pressure-sensor/10.1117/12.2290361.short.

[32] H. Gao *et al.*, “Simulation and characterization of a high-sensitive micro-opto-mechanical Microphone,” *2018 19th International Conference on Thermal, Mechanical and Multi-Physics Simulation and Experiments in Microelectronics and Microsystems, EuroSimE 2018*, pp. 1–4, May 2018. DOI: 10.1109/EUROSIME.2018.8369932.

[33] W. J. Westerveld *et al.*, “Micro-Opto-Mechanical Pressure, Sound, and Ultrasound Sensors in Silicon-Nitride Photonic Technology,” Tech. Rep., 2019. [Online]. Available: www.pix4life.eu.

[34] D. Yuan, Y. Dong, Y. Liu, and T. Li, “Mach-Zehnder Interferometer Biochemical Sensor Based on Silicon-on-Insulator Rib Waveguide with Large Cross Section,” *Sensors 2015, Vol. 15, Pages 21500-21517*, vol. 15, no. 9, pp. 21 500–21 517, Aug. 2015. DOI: 10.3390/S150921500.

[35] P. K. Pattnaik, B. Vijayaaditya, T. Srinivas, and A. Selvarajan, “Optical MEMS pressure sensor using ring resonator on a circular diaphragm,” *Proceedings - 2005 International Conference on MEMS, NANO and Smart Systems, ICMENS 2005*, pp. 277–280, 2005. DOI: 10.1109/ICMENS.2005.94.

[36] S. M. Leinders *et al.*, “A sensitive optical micro-machined ultrasound sensor (OMUS) based on a silicon photonic ring resonator on an acoustical membrane,” *Scientific Reports*, vol. 5, Sep. 2015. DOI: 10.1038/srep14328.

[37] W. J. Westerveld *et al.*, “Supplementary Information (SI) for: Sensitive, small, broadband and scalable optomechanical ultrasound sensor in silicon photonics,” *Nature Photonics*, vol. 15, no. 5, pp. 341–345, May 2021. DOI: 10.1038/s41566-021-00776-0.

[38] R. L. St Pierre and D. J. Maguire, “The Impact of A-weighting Sound Pressure Level Measurements during the Evaluation of Noise Exposure,” 2004.

[39] Y. Nemirovsky and O. Bochobza-Degani, “A methodology and model for the pull-in parameters of electrostatic actuators,” *Journal of Microelectromechanical Systems*, vol. 10, no. 4, pp. 601–615, Dec. 2001. DOI: 10.1109/84.967384.

[40] H. C. Nathanson, W. E. Newell, R. A. Wickstrom, and J. R. Davis, “The Resonant Gate Transistor,” *IEEE Transactions on Electron Devices*, vol. ED-14, no. 3, pp. 117–133, 1967. DOI: 10.1109/T-ED.1967.15912.

[41] W. Kühnel and G. Hess, “A silicon condenser microphone with structured back plate and silicon nitride membrane,” *Sensors and Actuators: A. Physical*, vol. 30, no. 3, pp. 251–258, 1992. DOI: 10.1016/0924-4247(92)80128-P.

[42] P. R. Scheeper *et al.*, “A silicon condenser microphone with a silicon nitride diaphragm and backplate,” *Journal of Micromechanics and Microengineering*, vol. 2, pp. 187–189, 1992.

[43] V. Naderyan, R. Raspet, and C. Hickey, “Thermo-viscous acoustic modeling of perforated micro-electro-mechanical systems (MEMS),” *The Journal of the Acoustical Society of America*, vol. 148, no. 4, p. 2376, Oct. 2020. DOI: 10.1121/10.0002357. [Online]. Available: https://asa.scitation.org/doi/abs/10.1121/10.0002357.

[44] P. Scheeper, W. Olthuis, and P. Bergveld, “The Design, Fabrication, and Testing of Corrugated Silicon Nitride Diaphragms,” *Journal of Microelectromechanical Systems*, vol. 3, no. 1, pp. 36–42, 1994. DOI: 10.1109/84.285722.

[45] M. Ying, Q. Zou, and S. Yi, “Finite-element analysis of silicon condenser microphones with corrugated diaphragms,” Tech. Rep., 1998, pp. 163–173.

[46] M. Füldner, A. Dehé, and R. Lerch, “Analytical analysis and finite element simulation of advanced membranes for silicon microphones,” *IEEE Sensors Journal*, vol. 5, no. 5, pp. 857–862, Oct. 2005. DOI: 10.1109/JSEN.2004.841449.

[47] J. Bernstein, “Micromachined condenser hydrophone,” *Technical Digest- IEEE Solid-State Sensor and Actuator Workshop*, pp. 161–165, 1992. DOI: 10.1109/SOLSEN.1992.228301.

[48] P. R. Scheeper, W. Olthuis, and P. Bergveld, “Improvement of the performance of microphones with a silicon nitride diaphragm and backplate,” *Sensors and Actuators A: Physical*, vol. 40, no. 3, pp. 179–186, Mar. 1994. DOI: 10.1016/0924-4247(94)87003-9.

[49] H. A. Tilmans, “Equivalent circuit representation of electromechanical transducers: I. Lumped-parameter systems,” *Journal of Micromechanics and Microengineering*, vol. 6, no. 1, p. 157, Mar. 1996. DOI: 10.1088/0960-1317/6/1/036.

[50] H. A. C. Tilmans *et al.*, “Equivalent circuit representation of electromechanical transducers: II. Distributed-parameter systems,” *Journal of Micromechanics and Microengineering*, vol. 7, no. 4, p. 285, Dec. 1997. DOI: 10.1088/0960-1317/7/4/005.

[51] H. Gharaei and J. Koohsorkhi, “Design and characterization of high sensitive MEMS capacitive microphone with fungous coupled diaphragm structure,” *Microsystem Technologies*, vol. 22, no. 2, pp. 401–411, Feb. 2016. DOI: 10.1007/S00542-014-2406-2/FIGURES/17.

[52] S. P. Mao *et al.*, “Modal analysis based equivalent circuit model and its verification for a single cMUT cell,” *Journal of Micromechanics and Microengineering*, vol. 27, no. 3, Jan. 2017. DOI: 10.1088/1361-6439/aa53ce.

[53] L. E. Kinsler, A. R. Frey, A. B. Coppens, and J. V. Sanders, *Fundamentals of Acoustics*, Fourth Edition. John Wiley & Sons, Inc., 1950, pp. 184–188.

[54] D. Blackstock, *Fundamentals of Physical Acoustics*. John Wiley & Sons, Inc., 2000.

[55] L. Beranek, *Acoustics*. American Institute of Physics: New York, 1954.

[56] B. E. Anderson, “Understanding radiation impedance through animations,” *Citation: Proc. Mtgs. Acoust*, vol. 33, p. 25 003, 2018. DOI: 10.1121/2.0001259. [Online]. Available: https://doi.org/10.1121/2.0001259.

[57] M. Jensen, *Theory of Thermoviscous Acoustics: Thermal and Viscous Losses*, Feb. 2014. [Online]. Available: https://www.comsol.com/blogs/theory-of-thermoviscous-acoustics-thermal-and-viscous-losses/.

[58] J. Wolfe, *Open vs Closed pipes (Flutes vs Clarinets)*, 2023. [Online]. Available: http://www.phys.unsw.edu.au/jw/flutes.v.clarinets.html.

[59] J. Woodhouse, *4.2.1 The Helmholtz resonator – Euphonics*, 2023. [Online]. Available: https://euphonics.org/4-2-1-the-helmholtz-resonator/.

[60] C. Loudon and K. Mcculloh, “Application of the Hagen—Poiseuille Equation to Fluid Feeding through Short Tubes,” *Annals of the Entomological Society of America*, vol. 92, no. 1, pp. 153–158, Jan. 1999. DOI: 10.1093/AESA/92.1.153. [Online]. Available: https://dx-doi-org.tudelft.idm.oclc.org/10.1093/aesa/92.1.153.

[61] H. B. Callen, T. A. Eusda, and Morgan, “Irreversibility and Generalized Noise*,” *Randal Morgan Laboratory of Physics, University of Pennsylvania*, vol. 83, no. 1, 1951.

[62] T. B. Gabrielson, “Mechanical-Thermal Noise in Micromachined Acoustic and Vibration Sensors,” *IEEE Transactions on Electron Devices*, vol. 40, no. 5, pp. 903–909, 1993. DOI: 10.1109/16.210197.

[63] S. S. Rao, *Vibration of Continuous Systems*. 2007.

[64] M. Bao and H. Yang, “Squeeze film air damping in MEMS,” *Sensors and Actuators A: Physical*, vol. 136, no. 1, pp. 3–27, May 2007. DOI: 10.1016/J.SNA.2007.01.008.

[65] V. Naderyan, R. Raspet, and C. Hickey, “Analytical, computational, and experimental study of thermoviscous acoustic damping in perforated micro-electro-mechanical systems with flexible diaphragm,” *The Journal of the Acoustical Society of America*, vol. 150, no. 4, p. 2749, Oct. 2021. DOI: 10.1121/10.0006378. [Online]. Available: https://asa.scitation.org/doi/abs/10.1121/10.0006378.

[66] P. Li, Y. Fang, and F. Xu, “Analytical modeling of squeeze-film damping for perforated circular microplates,” *Journal of Sound and Vibration*, vol. 333, no. 9, pp. 2688–2700, Apr. 2014. DOI: 10.1016/J.JSV.2013.12.028.

[67] M. P. Desmulliez and G. Hantos, “Investigation into low frequency response of acoustic MEMS for determination of failure modes Citation for published version: Hantos, G & Desmulliez, MPY 2021, ’Investigation into low frequency response of acoustic MEMS for determination of failure modes’,” *IEEE Transactions on Semiconductor Manufacturing*, vol. PP, 2021. DOI: 10.1109/TSM.2021.3065553.

[68] M. S. Elbaz *et al.*, “Assessment of viscous energy loss and the association with three□dimensional vortex ring formation in left ventricular inflow: In vivo evaluation using four□dimensional flow MRI,” *Magnetic Resonance in Medicine*, vol. 77, no. 2, p. 794, Feb. 2017. DOI: 10.1002/MRM.26129. [Online]. Available: /pmc/articles/PMC5297883//pmc/articles/PMC5297883/?report=abstracthttps://www.ncbi.nlm.nih.gov/pmc/articles/PMC5297883/.

[69] S. C. Thompson and J. L. LoPresti, “Thermal boundary layer effects on the acoustical impedance of enclosures and consequences for acoustical sensing devicesa),” *The Journal of the Acoustical Society of America*, vol. 123, no. 3, p. 1364, Mar. 2008. DOI: 10.1121/1.2832314. [Online]. Available: https://asa.scitation.org/doi/abs/10.1121/1.2832314.

[70] F. B. Daniels, “Acoustical Impedance of Enclosures,” *Citation: The Journal of the Acoustical Society of America*, vol. 19, p. 569, 1947. DOI: 10.1121/1.1916522. [Online]. Available: https://doi.org/10.1121/1.1916522.

[71] Wikipedia, *Total internal reflection*, 2022. [Online]. Available: https://en.wikipedia.org/wiki/Total_internal_reflection.

[72] A. Yariv, “Universal relations for coupling of optical power between microresonators and dielectric waveguides,” *Electronics Letters*, vol. 36, no. 4, pp. 321–322, Feb. 2000. DOI: 10.1049/el:20000340.

[73] universitywafer.com, *Silicon-on-Insulator Substrates*, 2023. [Online]. Available: https://www.universitywafer.com/silicon-on-insulator-soi.html.

[74] CORNERSTONE, “Design guidelines for CORNERSTONE MPW #28,” Tech. Rep., 2022. [Online]. Available: www.cornerstone.sotonfab.co.uk/terms-and-conditions.

[75] M. N. Polyanskiy, *https://refractiveindex.info/*, 2023. [Online]. Available: https://refractiveindex.info/.

[76] X. Wang, W. Shi, H. Yun, S. Grist, N. A. F. Jaeger, and L. Chrostowski, “Narrow-band waveguide Bragg gratings on SOI wafers with CMOS-compatible fabrication process,” *Optics Express*, vol. 20, no. 14, p. 15 547, Jul. 2012. DOI: 10.1364/OE.20.015547. [Online]. Available: https://www.researchgate.net/publication/228443621_Narrow-band_waveguide_Bragg_gratings_on_SOI_wafers_with_CMOS-compatible_fabrication_process.

[77] IEC, *IEC 61672-1:2013 Electroacoustics - Sound level meters - Part 1: Specifications*. IEC, 2013.

[78] A. W. Leissa, *Vibration of plates*. 1969, pp. 1–10.

[79] M. Bîrsan, D. Pietras, and T. Sadowski, “Determination of effective stiffness properties of multilayered composite beams,” *Continuum Mechanics and Thermodynamics*, vol. 33, no. 4, pp. 1781–1803, Jul. 2021. DOI: 10.1007/S00161-021-01006-2/FIGURES/16. [Online]. Available: https://link-springer-com.tudelft.idm.oclc.org/article/10.1007/s00161-021-01006-2.

[80] K. K. Williams, “Understanding buckling phenomena in multilayered membranes,” Tech. Rep., 2018.

[81] M. Siškins *et al.*, “SUPPLEMENTARY INFORMATION: Nanomechanical probing and strain tuning of the Curie temperature in suspended Cr 2 Ge 2 Te 6-based heterostructures,” 2021.

[82] W. J. Westerveld *et al.*, “Characterization of Integrated Optical Strain Sensors Based on Silicon Waveguides,” *IEEE Journal of Selected Topics in Quantum Electronics*, vol. 20, no. 4, Jul. 2014. DOI: 10.1109/JSTQE.2013.2289992.

[83] M. Hammer, *Mode solver for 2-D multilayer waveguides, variational effective index approximation*, 2023. [Online]. Available: https://www.computational-photonics.eu/eims.html.

[84] Koheron, *1550 nm low-noise DFB laser*, 2023. [Online]. Available: https://www.koheron.com/photonics/ld100-laser.

[85] Koheron, *Low noise photodetector*, 2023. [Online]. Available: https://www.koheron.com/photonics/pd100-photodetection.

[86] V. Mackowiak, J. Peupelmann, Y. Ma, and A. Gorges, “NEP-Noise Equivalent Power,”

[87] R. P. Mann *et al.*, “Wet Etching,” *Encyclopedia of Nanotechnology*, pp. 2829–2830, 2012. DOI: 10.1007/978-90-481-9751-4{_}431. [Online]. Available: https://link.springer.com/referenceworkentry/10.1007/978-90-481-9751-4_431.

[88] A. Dendane, *Transfer Function in the Frequency Domain*, 2023. [Online]. Available: http://www.mathforengineers.com/transfer-functions/transfer-function-in-the-frequency-domain.html.

[89] P. G. Steeneken, R. J. Dolleman, D. Davidovikj, F. Alijani, and H. S. J. Van der Zant, “Dynamics of 2D material membranes,” 2021. DOI: 10.1088/2053-1583/ac152c.

[90] S Timoshenko, *Theory of plates and shells*, 2nd edition. McGraw-Hill Book Company, 1959.

[91] I. O. Wygant, M. Kupnik, and B. T. Khuri-Yakub, “Analytically calculating membrane displacement and the equivalent circuit model of a circular CMUT cell,” *Proceedings - IEEE Ultrasonics Symposium*, pp. 2111–2114, 2008. DOI: 10.1109/ULTSYM.2008.0522.

A

Transfer functions acoustic thermal noise

The transfer function is used to find the voltage over the capacitor that represents the diaphragm stiffness. A simple example of a transfer function with an input voltage and a desired output voltage is shown in Figure A.1, where Z_1 and Z_2 are complex impedances. The transfer function can be found with Kirchoff's and Ohm's law. Kirchhoff's voltage law states that the sum of voltages around any closed loop in a circuit is equal to zero. Kirchhoff's current law states that the sum of currents entering a node (or junction) in a circuit is equal to the sum of currents leaving that node, considering current as a conserved quantity. Ohm's Law for the voltage across a resistor states that the voltage across a resistor is equal to the current flowing through it multiplied by the resistance of the resistor [88]. Applying these for the simple circuit results in the transfer function of:

$$H(j\omega) = \frac{V_{out}}{V_{in}} = \frac{Z_2}{Z_1 + Z_2} \tag{A.1}$$

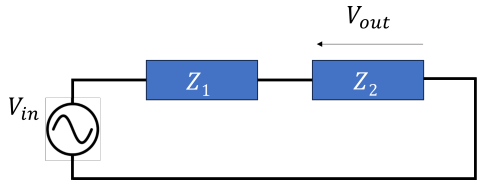

Figure A.1: Example of input and output voltage simplified for two impedances.

To derive a more complex transfer function, the complex impedances of both capacitors and inductors should be known:

$$Z_C = \frac{1}{j\omega C} \tag{A.2}$$

$$Z_L = j\omega L \tag{A.3}$$

Now, all information is available to derive the transfer functions of more complex systems. The next sections will derive the transfer functions of the circuits discussed in subsection 4.2.4, using Ohm's and Kirchoff's law as stated above.

A.1. Front Volume

The first circuit for which the transfer function is derived is the circuit used to calculate the acoustic noise corresponding to the front volume of the microphone. The indications of the in- and output voltages, representing pressures, are shown in Figure A.2. Also, the currents, representing volume flow, are indicated with $I, I_1 and I_2$. The four following equations are derived from Kirchoff's and Ohm's law, used to come to the transfer function:

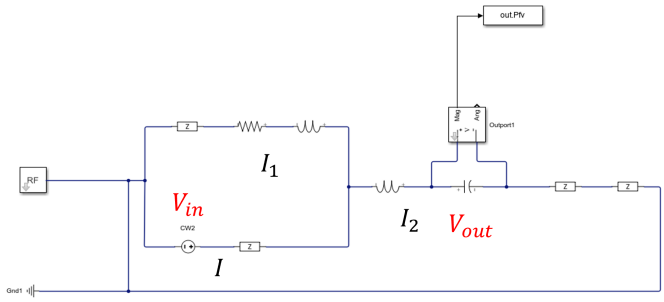

Figure A.2: Circuit of the noise due to the front volume impedance.

$$I = I_1 + I_2 \tag{A.4}$$
$$I_1(Z_{mp} + R_p + Z_{radport}) = I_2(Z_{md} + Z_d + Z_{damp} + Z_{rad}) \tag{A.5}$$
$$V_{out} = Z_c I_2 \tag{A.6}$$
$$V_{in} = I Z_{fv} + I_1(Z_{mp} + R_p + Z_{radport}) \tag{A.7}$$

Now the transfer function is found as:

$$H_{FV}(j\omega) = \frac{V_{out}}{V_{in}} = \frac{Z_{cd}}{Z_{fv} + (Z_{fv} + Z_{mp} + R_p + Z_{radport}) \cdot \frac{Z_{md}+Z_{cd}+Z_{damp}+Z_{rad}}{Z_{mp}+R_p+Z_{radport}}} \tag{A.8}$$

A.2. Port

The definitions of the voltages and currents used to derive the port transfer function, together with the electronic circuit itself, are shown in Figure A.3. For the port radiation and resistance, the transfer function is derived from the following four equations:

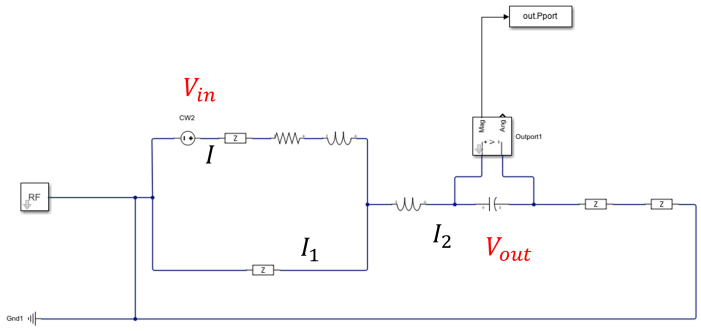

Figure A.3: Circuit of the noise due to port impedance.

$$I = I_1 + I_2 \tag{A.9}$$
$$I_1 Z_{fv} = I_2(Z_c + Z_{md} + Z_{damp} + Z_{rad}) \tag{A.10}$$
$$V_{out} = I_2 Z_c \tag{A.11}$$
$$V_{in} = I(Z_{radport} + R_p + Z_{mp}) + I_1 Z_{fv} \tag{A.12}$$

This results in the following transfer function for the port:

$$H_{port}(j\omega) = \frac{V_{out}}{V_{in}} = \frac{Z_{cd}}{\left(\frac{Z_{cd}+Z_{md}+Z_{damp}+Z_{rad}}{Z_{fv}} \cdot (Z_{radport} + R_p + Z_{mp} + Z_{fv}) + Z_{rad_{port}} + R_p + Z_{mp}\right)} \tag{A.13}$$

A.3. Backside radiation impedance

The definitions of the voltages and currents used to derive the backside transfer function, together with the electronic circuit itself, are shown in Figure A.4. For the backside radiation, the transfer function is derived from the following four equations:

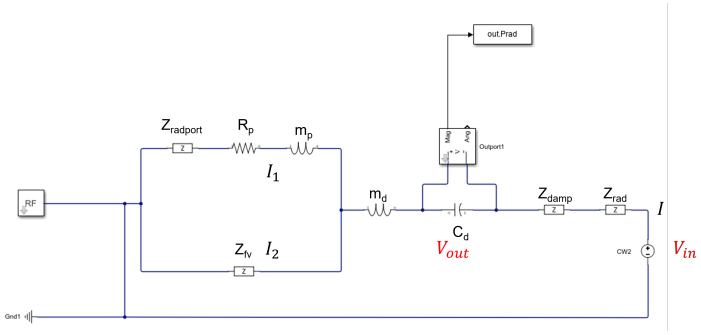

Figure A.4: Circuit of the noise due to backside radiation impedance.

$$I = I_1 + I_2 \tag{A.14}$$

This results in the following transfer function for the backside radiation:

$$H_{rad}(j\omega) = \frac{V_{out}}{V_{in}} = \frac{Z_{cd} + Z_{cd} \cdot \frac{Z_{radport}+R_p+Z_{mp}}{Z_{fv}}}{Z_{rad_{port}} + R_p + Z_{mp} + Z_{rad} + Z_{cd} + Z_{md} + Z_{damp} + \frac{(Z_{rad}+Z_{cd}+Z_{md}+Z_{damp})\cdot(Z_{rad_{port}}+R_p+Z_{mp})}{Z_{fv}}} \tag{A.15}$$

A.4. Signal itself

The signal itself can also be computed with a transfer function of the circuit, where the input voltage is placed in front of the parallel junction of the front volume and the port. The transfer function is then identical to the transfer function derived in the previous section, such that the response to a signal of 1 pascal at 1 kHz can be found with $V_{out} = H_{rad}(j\omega) \cdot V_{sig}$, where V_{sig} represents the pressure of the input signal.

B
Mass-spring-damper systems

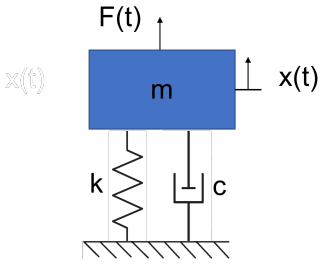

Figure B.1: Schematic overview of a mass-spring-damper system

The basics of modelling vibration of a circular diaphragm start with understanding the principle of a mass-spring-damper system, also referred to as a damped harmonic oscillator (see Figure B.1). These are well-known systems and I used [63] to derive the formulas. The equation of motion is often written in two forms:

$$F(t) = m\ddot{x}(t) + c\dot{x}(t) + kx(t) \tag{B.1a}$$

$$\frac{F(t)}{m} = \ddot{x}(t) + 2\zeta\omega_0\dot{x}(t) + \omega_0^2 x(t) \tag{B.1b}$$

where $\omega_0 = \sqrt{k/m}$ is the undamped angular resonance frequency and $\zeta = \frac{C}{2\sqrt{mk}}$ the damping ratio, which relates to the Q factor defined by $Q = \frac{1}{2\zeta}$. When the damping is proportional to the velocity, it is referred to as viscous damping. For the underdamped situation ($\zeta < 1$), the natural frequency shifts with $\omega_d = \omega_0\sqrt{1-\zeta^2}$. For the damped case, the amplification at the resonance frequency disappears. When there is no external force $F(t) = 0$ (damped free vibration), the general solution is equal to:

$$x(t) = e^{-\zeta\omega_0 t}\left(x_0 \cos(\omega_d t) + \frac{\dot{x}_0 + \zeta\omega_0 x_0}{\omega_d}\sin(\omega_d t)\right) \tag{B.2}$$

with x_0 and $\dot{x}_0$ denote the initial position and velocity respectively. When the system is driven with a harmonic force in complex form $\boldsymbol{F} = F_0 e^{j\omega t}$:

$$m\ddot{x}(t) + c\dot{x}(t) + kx(t) = F_0 e^{j\omega t}, \tag{B.3}$$

the solution can be written as:

$$x(t) = \frac{F_0}{k}|H(j\omega)|e^{j(\omega t - \phi)}, \tag{B.4}$$

where

$$H(j\omega) \equiv \frac{1}{(\frac{j\omega}{\omega_0})^2 + 2\zeta\frac{j\omega}{\omega 0} + 1} \tag{B.5}$$

is the complex frequency response of the system and $\phi = \tan^{-1}(\frac{c\omega}{k - m\omega^2})$ indicates the phase angle. The frequency response of a damped mass-spring-damper system is shown in Figure B.2 for different values of ζ.

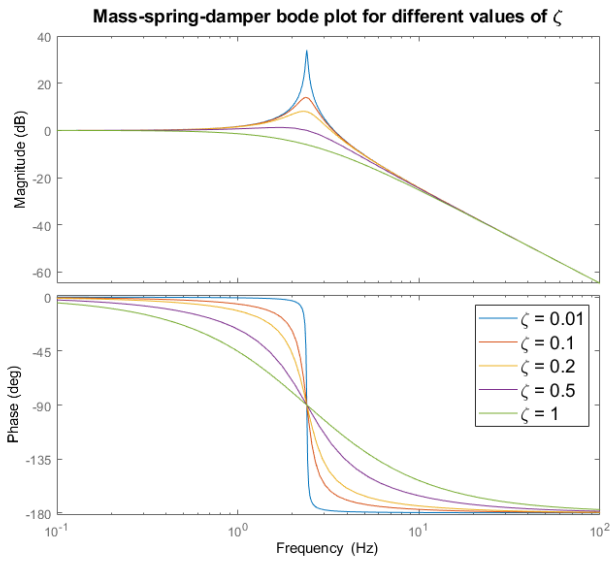

Figure B.2: Bode diagram of mass-spring-damper system for different values of ζ

The displacement of the mass is given by the absolute value of $|x(t)|$ and the phase between force and displacement is given by the complex argument $\angle x(t)$. When the driving harmonic force has no complex part $F(t) = F_0 \cos(\omega t)$, the solution is simplified to:

$$x(t) = \frac{F_0}{\sqrt{(k - m\omega^2)^2 + c^2\omega^2}} \cos(\omega t - \phi) \tag{B.6}$$

More complex systems such as a circular clamped plate can be reduced to a single mass-spring-damper system with an effective mass and stiffness, such that these equations can be applied.

C

Derivation of clamped circular plate

The well-established solution for vibration in plates is given by Leissa [78]. The dynamic equation for plates without damping and no external force in polar coordinates is:

$$D\nabla_r^4 w(r,\theta,t) + \rho h \frac{\partial^2 w(r,\theta,t)}{\partial t^2} = 0, \tag{C.1}$$

with $\nabla_r^2 = \frac{\partial^2}{\partial r^2} + \frac{1}{r}\frac{\partial}{r} + \frac{1}{r^2}\frac{\partial^2}{\partial \theta^2}$ the Laplacian operator, $w(r,\theta,t)$ the out of plane displacement, ρ the mass density, h the plate thickness, and D the bending rigidity defined by Equation C.4.

where E is the Young's modulus of the material, v the Poisson's ratio. This equation only holds for homogeneous isotropic plates. When the origin of a polar coordinate system coincides with the centre of a solid circular plate, the general solution is:

$$W(r,\theta) = \sum_{n=0}^{\infty} [A_n J_n(kr) + C_n I_n(kr)] \cos(n\theta) + \sum_{n=1}^{\infty} [A_n^* J_n(kr) + C_n^* I_n(kr)] \sin(n\theta), \tag{C.2}$$

with J_n the Bessel function and I_n the modified Bessel function of the order n. The coefficients A_n and C_n determine the mode shape and are found through the boundary conditions. The parameter k is used for convenience and defined by:

$$k^2 = \omega\sqrt{\frac{\rho h}{D}} \tag{C.3}$$

with D the bending rigidity defined as:

$$D = \frac{Eh^3}{12(1-v^2)} \tag{C.4}$$

When boundary conditions are symmetric with respect to one or more diameters of the circle, the terms involving $\sin(n\theta)$ are not needed. For a clamped edge, the boundary conditions at the edge $r = a$ are:

$$W(a) = 0 \tag{C.5a}$$

$$\frac{\partial W(a)}{\partial r} = 0 \tag{C.5b}$$

If Equation C.5a is applied to Equation C.2, we see the relation

$$\frac{A_n}{C_n} = \frac{A_n^*}{C_n^*} = -\frac{I_n(\lambda_{ns})}{J_n(\lambda_{ns})} \tag{C.6}$$

where $\lambda_{ns} = ka$ defines the roots of the mode shapes. Now the second boundary condition (C.5b) results in the frequency equation [89]:

$$I_n(\lambda_{ns})J_{n-1}(\lambda_{ns}) - J_n(\lambda_{ns})I_{n-1}(\lambda_{ns}) = 0 \tag{C.7}$$

For each value of $n = 0, 1, 2...$, λ_{ns} has $s = 1, 2, 3...$ solutions so that all the roots with corresponding eigenmodes are defined as λ_{ns}. The resonance frequency that belongs to the vibration mode is found with:

$$\omega_{ns} = \left(\frac{\lambda_{ns}}{a}\right)^2 \sqrt{\frac{D}{\rho h}} \tag{C.8}$$

The first values of λ_{ns} are tabulated in Table C.1 (from ref. [78]). Now the general solution for the eigenmodes becomes:

λ_{ns}			
s	n = 0	n = 1	n =2
1	**3.196**	4.611	5.906
2	6.306	7.799	9.197
3	9.439	10.958	12.402

Table C.1: Values of λ_{ns} that belong to circular clamped plate

$$W_{ns}^{(1)}(r,\theta) = \left[J_n(\lambda_{ns}\frac{r}{a})I_n(\lambda_{ns}) - J_n(\lambda_{ns})I_n(\lambda_{ns}\frac{r}{a})\right]\cos(n\theta) \tag{C.9a}$$

$$W_{ns}^{(2)}(r,\theta) = \left[J_n(\lambda_{ns}\frac{r}{a})I_n(\lambda_{ns}) - J_n(\lambda_{ns})I_n(\lambda_{ns}\frac{r}{a})\right]\sin(n\theta) \tag{C.9b}$$

When the plate is excited by uniform pressure below the resonance frequency, only the first mode shape is considered as the dominant contribution to the transverse displacement of the diaphragm. So for $n = 0$, terms with $\sin(n\theta)$ are zero and if we normalize the mode shape to the deflection of the centre we find the normalized mode shape of the first resonance with $\lambda_{01} = 3.196$:

$$\frac{W_{01}(r)}{W_{01}(0)} = \frac{J_0(\lambda_{01}\frac{r}{a})I_0(\lambda_{01}) - J_0(\lambda_{01})I_0(\lambda_{01}\frac{r}{a})}{I_0(\lambda_{01}) - J_0(\lambda_{01})} \tag{C.10}$$

For simplicity $W_{01}(0)$ will be expressed as w_0. The eigenfrequency corresponding to the first mode can be found with:

$$\omega_{01} = \left(\frac{\lambda_{01}}{a}\right)^2 \sqrt{\frac{D}{\rho h}} \tag{C.11}$$

Now it is possible to compare the static and dynamic mode shapes of a clamped circular plate. It is somewhat difficult to find the central deflection w_0 so just to compare the shape these have been set equal. The result is shown in Figure C.1a, and a 3D surface plot of the dynamic shape is shown in Figure C.1b.

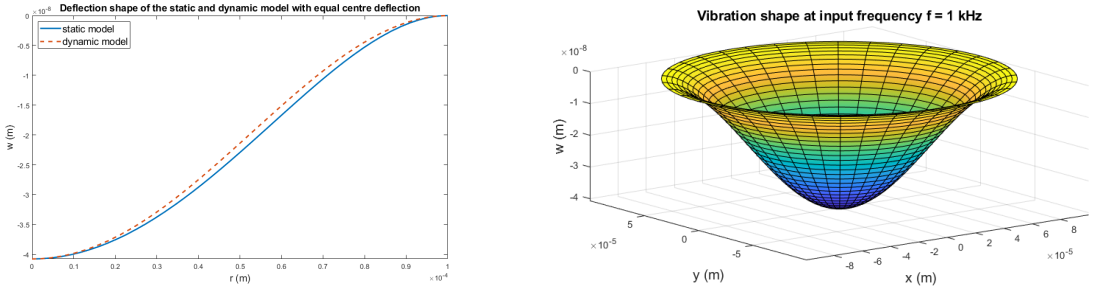

(a) **(b)**

Figure C.1: a) Deflection shape of dynamic and static model. **b)** 3D surface plot of the mode shape described by Equation C.10

D

From clamped circular plate to mass-spring-damper

The circular clamped plate is modelled as a single mass-spring-damper system (see Appendix B), referred to as lumped element representation. This is done in Ref. [9] for a capacitive microphone diaphragm as well; see Figure D.1. The displacement of the lumped element $x(t)$ corresponds to the displacement of the centre of the diaphragm w_0. To solve the equation of motion, the lumped mass is calculated such that the kinetic energy of the clamped circular plate and single mass are equal:

$$m_{eff} = \frac{2\pi\rho t}{y_c^2} \int_0^a y^2(r) r \, dr \tag{D.1}$$

with $y_c = y(0)$ the central deflection. To calculate the effective mass, it is sufficient to take the deflection shape that originates from a static pressure load on a circular clamped plate, such that $y(r)$ is given as [90]:

$$y(r) = \frac{p}{64D}(a^2 - r^2)^2 \tag{D.2}$$

with D the bending rigidity defined in Equation C.4. If the effective mass is now written in terms of a single coefficient:

$$m_{eff} = \alpha m = \alpha \rho h \pi a^2 \tag{D.3}$$

and Equation D.2 is substituted in Equation D.1, for a circular clamped plate the coefficient is equal to $\alpha = 0.2$.

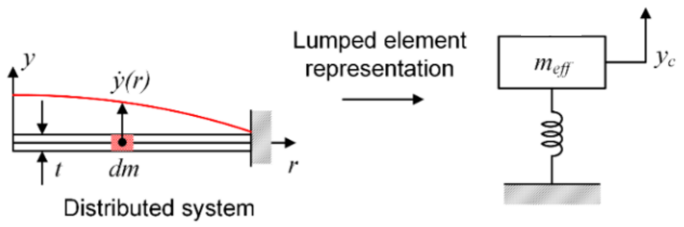

Figure D.1: Lumped element representation of a clamped plate, from Ref. [9]

.

With the effective mass and the resonance frequency in a vacuum given by Equation 5.2, the stiffness is:

$$k = \omega_{01}^2 m_{eff} \tag{D.4}$$

The mechanical impedance is given by Equation D.5:

$$\boldsymbol{Z}_{mv} = R_m + j(\omega m - \frac{1}{\omega} k) \tag{D.5}$$

The mechanical resistance is given by the damping coefficient ζ as:

$$R_m = 2\omega_{01} m_{eff} \zeta \tag{D.6}$$

Acoustically, the vibration of the plate can be modelled as a circular piston with a single mass and uniform velocity by means of an effective area, see Figure D.2:

$$A_{eff} = \beta A = \beta \pi a^2 = \frac{2\pi}{y_c} \int_0^a y(r) r dr \tag{D.7}$$

where $y(r)$ is calculated with Equation D.2. Solving for β results in $\beta = 1/3$ [91].

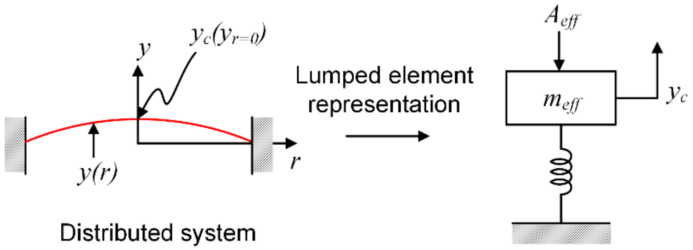

Figure D.2: Lumped element representation to add effective area, from Ref. [9].

The effective area can be used to model the force on the lumped element as $F = pA_{eff}$, so now Equation 2.24 becomes:

$$U_{m_{eff}} = \frac{pA_{eff}}{\boldsymbol{Z}_{mv} + \boldsymbol{Z}_{mr}} \tag{D.8}$$

Note that the impedances are calculated by substituting $m = m_{eff}$ in Equation 2.23 and the effective area A_{eff} in Equation 5.9. Finally, from the velocity it is possible to find the displacement of the centre w_0 due to the pressure p:

$$w_0 = \left| \frac{U_{m_{eff}}}{j\omega} \right| = \left| \frac{pA_{eff}}{j\omega(\boldsymbol{Z}_{mv} + \boldsymbol{Z}_{mr})} \right| \tag{D.9}$$

This formula can be used in combination with Equation 5.1 to find the total deflection of the vibrating clamped plate in air. In Figure D.3 the effect of the radiation impedance on the frequency response is shown by removing the radiation impedance $\boldsymbol{Z}_{mr}$ for vacuum in Equation D.9. In the next section, the effect of deflection on the photonic sensor is explained, such that a sensitivity function can be derived.

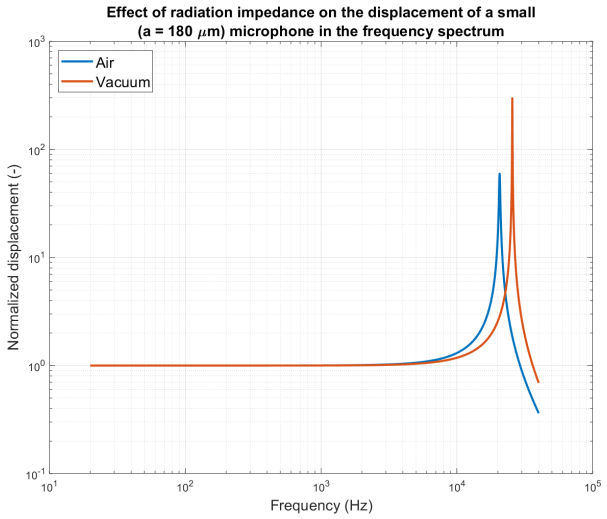

Figure D.3: Frequency response of a diaphragm with resonance frequency between 20-30 kHz for vacuum and baffled piston in air.

E

Optimum design results for all different design options

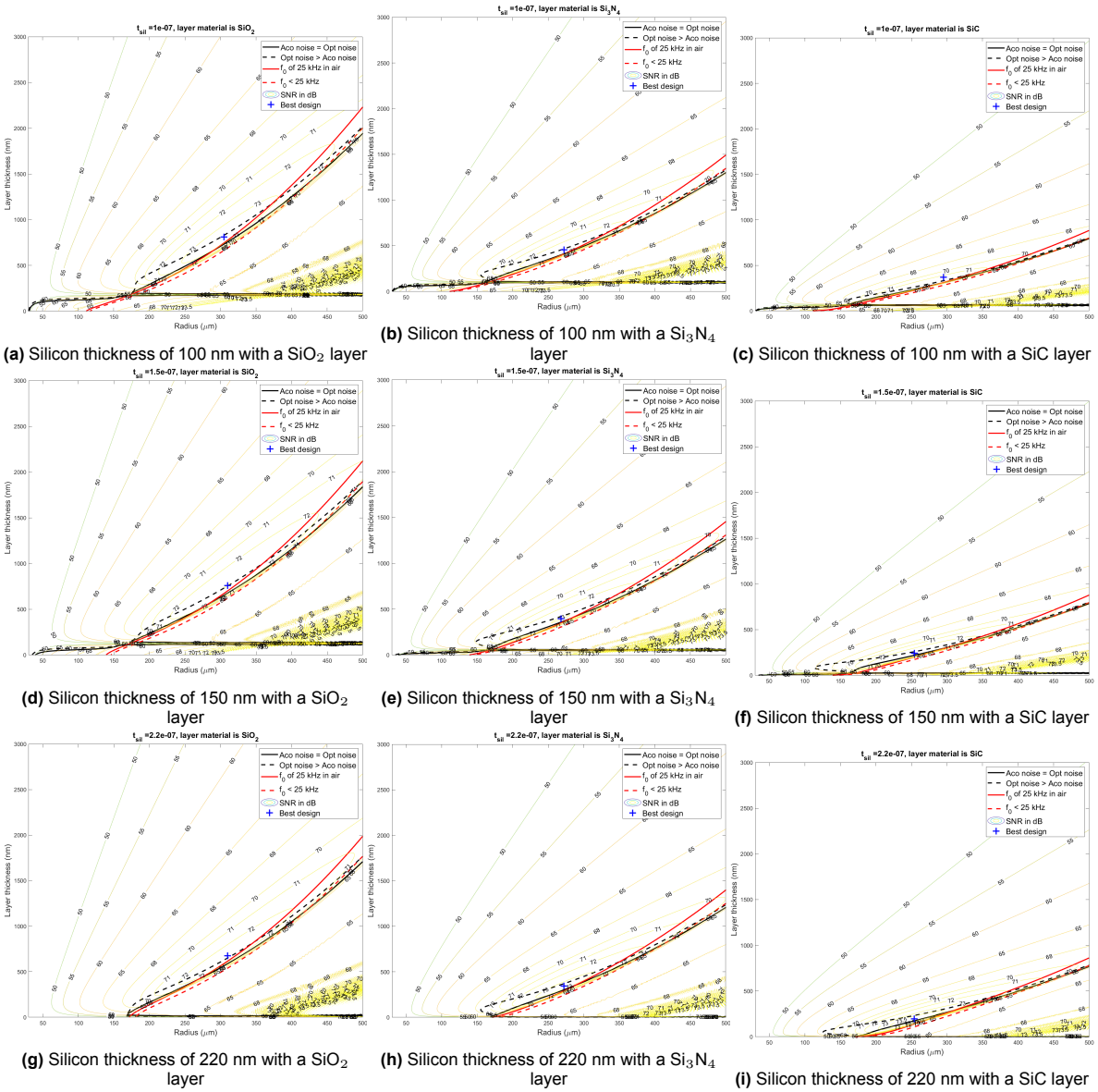

(a) Silicon thickness of 100 nm with a SiO_2 layer

(b) Silicon thickness of 100 nm with a Si_3N_4 layer

(c) Silicon thickness of 100 nm with a SiC layer

(d) Silicon thickness of 150 nm with a SiO_2 layer

(e) Silicon thickness of 150 nm with a Si_3N_4 layer

(f) Silicon thickness of 150 nm with a SiC layer

(g) Silicon thickness of 220 nm with a SiO_2 layer

(h) Silicon thickness of 220 nm with a Si_3N_4 layer

(i) Silicon thickness of 220 nm with a SiC layer

Figure E.1: Effect of radius and layer thickness on the SNR (dB) with an indication of the resonance frequency at 25 kHz and an indication where the optical noise is equal to the acoustic noise